Master's Thesis

Application of IGZO Semiconductors for UV photo detection

Author:
Maurice Schamber

Examiner:
Prof. Dr. Tilman Pfau
Co-Examiner:
Prof. Dr. Norbert Frühauf
Supervisor:
Yannick Schellander

University of Stuttgart
5th Institute of Physics
June 7, 2023

Erklärung über die Eigenständigkeit der Masterarbeit

Hiermit versichere ich, Maurice Schamber, dass die vorliegende Arbeit mit dem Titel **Application of IGZO Semiconductors for UV photo detection** nach Paragraph §24.7 der Prüfungsordnung 2015 für den Master of Science bearbeitet wurde. Dies beinhaltet

- dass die Arbeit bzw. bei einer Gruppenarbeit die entsprechend gekennzeichneten Anteil der Arbeit selbständig verfasst hat,
- dass keine anderen als die angegebenen Quellen benutzt und alle wörtlich oder sinngemäß aus anderen Werken übernommenen Aussagen als solche gekennzeichnet ist,
- dass die eingereichte Arbeit weder vollständig noch in wesentlichen Teilen Gegenstand eines anderen Prüfungsverfahrens gewesen ist,
- dass das elektronische Exemplar mit den anderen Exemplaren übereinstimmt.

Ort, Datum

Maurice Schamber

Contents

1 Zusammenfassung

In dieser Arbeit wurde die Herstellung und Charakterisierung von Fotosensoren auf Basis von Indium-Gallium-Zink-Oxid (IGZO) mittels Dünnschichttechnologie untersucht. IGZO ist ein vielversprechendes Material für die Detektion von UV-Licht aufgrund seiner großen Bandlücke von über 3 eV [1]. Das Forschungsinteresse liegt auf möglichen Anwendungen in Bereichen wie Displaytechnologie, Sensoren und neuromorphen Systemen [2].

Zunächst wurden verschiedene Sensor-Designs hergestellt und getestet. Dabei stellte sich heraus, dass der erzeugte Fotostrom von der aktiven Fläche des Sensors und der Geometrie abhängt. Es wurde festgestellt, dass mit Sensoren mit Gold-Elektroden auch für kleinere Dimensionen im Bereich von $10 - 100\,\mu$m Breite des aktiven Sensorbereichs nahezu identische Ergebnisse lieferten wie größere Breiten. Entscheidend für diese Schlussfolgerung war das Verhältnis zwischen dem Strom bei Bestrahlung und dem Dunkelstrom, welches einen Unterschied von mindestens einer Größenordnung aufwies. Die U/I-Kennlinie der Sensoren zeigte überwiegend ohmsches Verhalten, obwohl an der Metall-Halbleiter-Kontaktstelle ein Schottky-Kontakt erwartet wurde. Des Weiteren wurde festgestellt, dass die Reaktionszeit von der Dicke der IGZO-Schicht abhängt. Die besten Werte, die sich im Bereich von Millisekunden für Anstiegs- und Abfallzeit bewegten, wurden mit einer Schichtdicke von 120 nm erreicht.

Es wurde auch untersucht, ob die Variation der aktiven Schicht Einfluss auf die Eigenschaften hat. Dazu wurde eine Seite der Gold-Elektrode durch Indiumzinnoxid (ITO) oder Aluminium ersetzt. Allerdings führte dies zu keiner Verbesserung der Reaktionszeit. Es wurde auch ein vertikales Diodendesign getestet, bei dem entweder zwei Gold-Elektroden oder eine Variation mit ITO im Herstellungsprozess verwendet wurden. Hierbei waren die Reaktionszeiten signifikant schlechter, sodass dieser Ansatz keine Verbesserung brachte. Dennoch kann dieser Typ von Sensor in anderen Anwendungen als Stromquelle genutzt werden, da er ein konstantes Plateau des Fotostroms in der U/I-Kennlinie aufweist.

Als bestes Ergebnis wurde eine Photodiode mit einer aktiven Sensorfläche von $10\,\mu$m x $100\,\mu$m und zwei Gold-Elektroden identifiziert. Die Reaktionszeiten lagen im niedrigen Millisekundenbereich, sowohl für UV-Licht bei 385 nm als auch bei 226 nm. Responsivities von bis zu 2000 A/W bei 226 nm Licht wurden erreicht, was deutlich besser ist als in anderen vergleichbaren Studien. Die Responsivity hängt dabei von der angelegten Diodenspannung, der Lichtleistung des UV-Lichts und der Temperatur ab. Hohe Diodenspannungen von 20 V, geringere Lichtleistungen von einigen Mikrowatt und Raumtemperatur erzielten die besten Werte. Das Noise-equivalent-Power (NEP) ist signifikant besser als bei herkömmlichen Silizium-basierten Avalanche-Photodioden und erreichte einen Wert von bis zu $0.26\,\mathrm{nW}/\sqrt{\mathrm{Hz}}$ für 385 nm Licht.

Die Sensoren wurden anschließend im TraceGas-Sensor Experiment getestet, bei dem Stickstoffmonoxid durch eine Glaszelle strömt und mit Hilfe von Lasern in Rydbergzustände angeregt werden kann. Das Fluoreszenzlicht von einer Anregung bei 226 nm konnte mithilfe dieser Sensoren detektiert werden, wobei die gemessenen Breiten in etwa der theoretischen Doppler-Verbreiterung entsprachen. Darüber hinaus konnte gezeigt werden, wie sich die Strahlungseigenschaften eines Dipols mit einer Änderung der Polarisation verhielt. Als letzten Schritt in dieser Arbeit wurden die Sensoren in einem 8x8-Sensorarray hergestellt, mit dem alle Sensoren räumlich ausgelesen werden konnten. Es wurden vergleichbare Ergebnisse bezüglich der Strahlprofilcharakteristiken zu einer kommerziellen Photodiode erzielt.

Zusammenfassend konzentrierte sich diese Arbeit auf die Herstellung und Charakterisierung von IGZO-Fotosensoren für die UV-Lichterkennung. Es wurden verschiedene Designansätze untersucht, Leistungsparameter bewertet und gezeigt, dass Sensorarrays erfolgreich in räumlichen Messungen integriert werden können. Die Ergebnisse unterstreichen das vielversprechende Potenzial von IGZO-Fotosensoren für verschiedene Anwendungen und deren verbesserte Leistung im Vergleich zu herkömmlichen Silizium-basierten Avalanche-Photodioden [3].

2 Introduction

In this work, photosensors for ultraviolet light based on indium-gallium-zinc-oxide (IGZO) are investigated. Arranging sensors in arrays then allows first spatially resolved measurements.
IGZO is a relatively new material in research with promising application areas in display technology, sensing devices and neuromorphic systems [2]. It is particularly interesting because the band gap of IGZO is about 3-4 eV [1] and thus transparent in the visible range, but can be used for detection in the UV range. In contrast to conventional silicon based avalanche photodiodes [3] one hopes for better detection properties.

For this purpose, IGZO photosensors based on thin-film technology are designed, manufactured and characterized. These will be realized as passive matrix sensor arrays on glas substrates, which can then be easily integrated into vapor cells. The measurement setup of the utilized project can be used for the detection of nitric oxide gas, which uses gas flow cells for the nitric oxide. The aim is to produce efficient photosensors in the UV range, which, when integrated into the project's measurement set-up, should allow simple spatial readout of the sensors.

This thesis first discusses theoretical basics (chapter **Theoretical Background**) on two-level-systems and nitric oxide, which are relevant for later measurements. The production process of thin-film technology and general concepts of semiconductor-metal contact are briefly touched upon. The most important properties of the IGZO material are also discussed. This is followed by the structure of such a photodiode, the readout electronics and the software used in the chapter **Methods**. The experimental results are then discussed in the **Results** chapter. First, different design approaches are tested and then a selected photodiode is more closely examined in terms of response time, responsivity, signal-to-noise ratio and noise-equivalent power. In addition, fluorescence measurements on a nitrogen monoxide gas are performed and evaluated. Finally, a sensor array will be investigated to perform spatial measurements.

Information

Parts of this work have already been published in the paper **Ultraviolet photodetectors and readout based on a-IGZO semiconductor technology** [4].

3 Theoretical Background

3.1 Two-Level-System

In this work, concepts such as absorption and fluorescence of light in molecules are measured and discussed. The following section deals with some important basics.

3.1.1 Absorption profile

Absorption and emission of light in an atom or molecule can be often described approximately by a two-level system. In this simple description the influence of effects such as perturbation of nearby states are neglected [5]. In this thesis “frequency” resembles to the actual “angular frequency” for shortening reasons.
If light at frequency $\omega_\mathrm{L} = 2\pi f_\mathrm{L}$ drives a transition between $|1\rangle$ & $|2\rangle$ it can exite electrons from state $|1\rangle$ into a higher state $|2\rangle$. In a simple description the required incoming light frequency ω_L has to be equal to the resonance frequency ω_0 of the transition. The difference between resonance frequency and light frequency is called detuning $\Delta = \omega_\mathrm{L} - \omega_0$. Figure 1 shows a simple sketch of a two-level system.

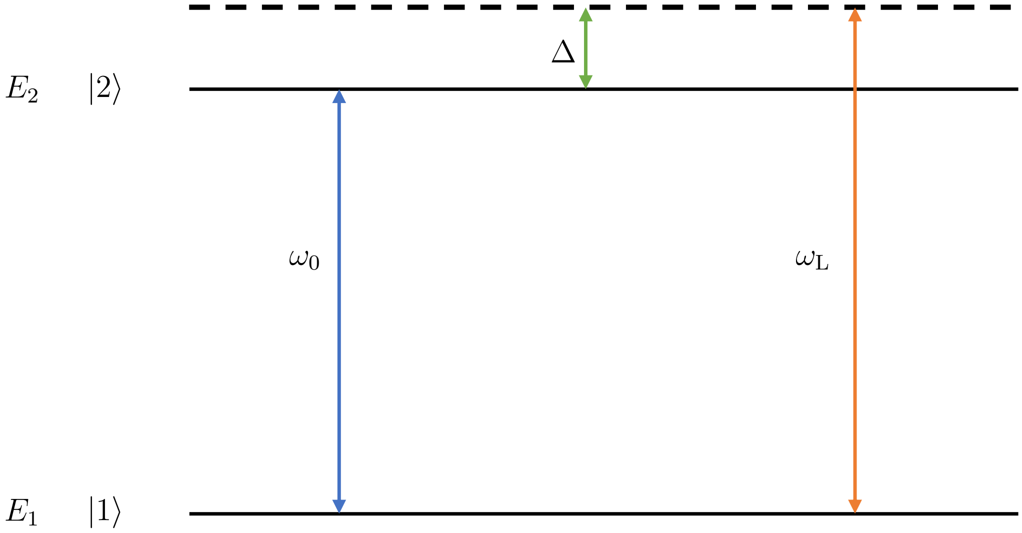

Figure 1: Sketch of a two-level system. Ground state $|1\rangle$ can be exited into $|2\rangle$ if the light beam ω_L is equal to the resonance frequency ω_0 .

Since in most systems a light beam passes through a medium with volume V filled with atoms/molecules which cause absorption, one has to look at the change of intensity I over the propagation distance. The reduction of intensity is given by the following differential equation

$$\frac{\mathrm{d}I}{\mathrm{d}L} = -\alpha(\omega)I \tag{3.1}$$

with $\alpha(\omega)$ being the frequency dependent absorption coefficient. $\mathrm{d}L$ resembles the infinitessimal change of propagation distance ΔL. Figure 2 drafts this approach. When integrating the differential equation, one obtains

$$I(\omega, L) = I(\omega, 0)e^{-\alpha(\omega)L}. \tag{3.2}$$

This formula is called *Beer's Law* and is only valid for neglecting stimulated emission corresponding to a much higher ground state population in comparison to the excited state.

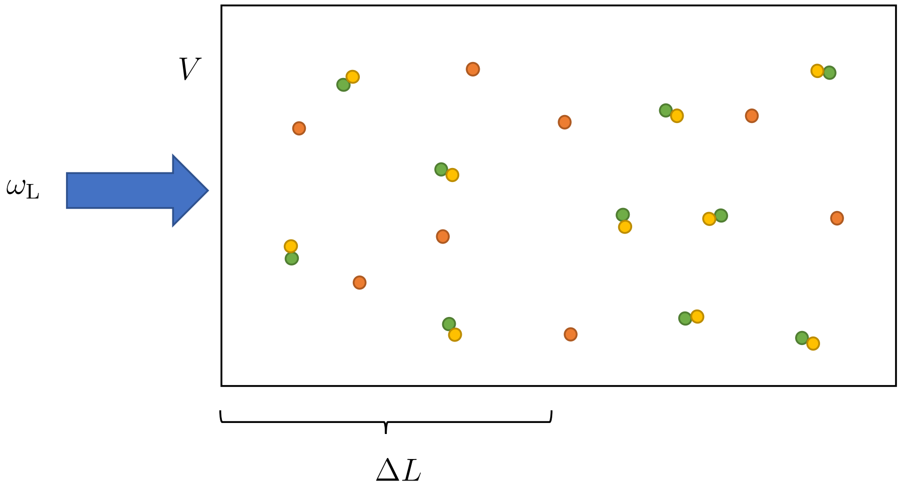

Figure 2: Light at frequency ω_L passes a volume V of length L filled with particles.

Describing absorption processes in atoms and molecules can be done by different approaches. The following concept is based on a semi-classical approach by treating the light field classical, starting with the time dependent Schrödinger equation [5]

$$i\hbar\frac{\partial\Psi}{\partial t} = H\Psi \tag{3.3}$$

with H being the Hamiltonian and Ψ being the wavefunction of the system. In this simple treatment the Hamiltonian $H = H_0 + H_\mathrm{int}$ consists of H_0 describing the molecular structure and H_int the interaction with the light field. A wavefunction $\Psi(\boldsymbol{r},t)$ can always be expressed as

$$\Psi(\boldsymbol{r},t) = c_1 \left|1\right\rangle e^{-iE_1t/\hbar} + c_2 \left|2\right\rangle e^{-iE_2t/\hbar} \tag{3.4}$$

because $|1\rangle$ and $|2\rangle$ are eigenstates in an unperturbed system H_0 and $c_{1,2}$ normalization constants. The electric field as $\boldsymbol{E} = \boldsymbol{E}_0\cos(\omega t)$ leads to a Hamiltonian $H_\mathrm{int} = e\boldsymbol{r}\boldsymbol{E_0}\cos(\omega t)$ describing the energy of an electric dipole. Using Equation 3.4 as ansatz for solving the Schrödinger equation leads to two coupled differential equations

$$i\dot{c_1} = \Omega\cos(\omega t)e^{-i\omega_0 t}c_2 \tag{3.5}$$

$$i\dot{c_2} = \Omega^*\cos(\omega t)e^{i\omega_0 t}c_1 \tag{3.6}$$

with Ω the Rabi frequency

$$\Omega = \frac{\left\langle 1\right| e\boldsymbol{r}\boldsymbol{E}_0 \left|2\right\rangle}{\hbar}. \tag{3.7}$$

To solve the coupled differential equations for the coefficients $c_{1,2}(t)$, one has to apply further approximations.

Rotating wave approximation Under the assumption that in the lower state $c_1(0) = 1$ and $c_2(0) = 0$ applying the first order approximation leads to [5]

$$c_1(t) = 1 \tag{3.8}$$

$$c_2(t) = \frac{\Omega^*}{2}\left\{\frac{1-e^{i(\omega_0+\omega)t}}{\omega_0+\omega} + \frac{1-e^{i(\omega_0-\omega)t}}{\omega_0-\omega}\right\}. \tag{3.9}$$

Close to the resonance, the limits $|\omega_0 - \omega| \ll \omega_0$ and $\omega_0 + \omega \approx 2\omega_0$ yield the probability coefficient for the upper state $|2\rangle$,

$$|c_2(t)|^2 = \left|\Omega \frac{\sin[(\omega_0-\omega)t/2]}{\omega_0-\omega}\right|^2. \tag{3.10}$$

Figure 3 shows the probability for $t = 2$ and $\Omega = 1$. As expected the maximum is at the resonance frequency and minima at $\pm 2n\pi/t$ for $n \in \mathbb{N}$.

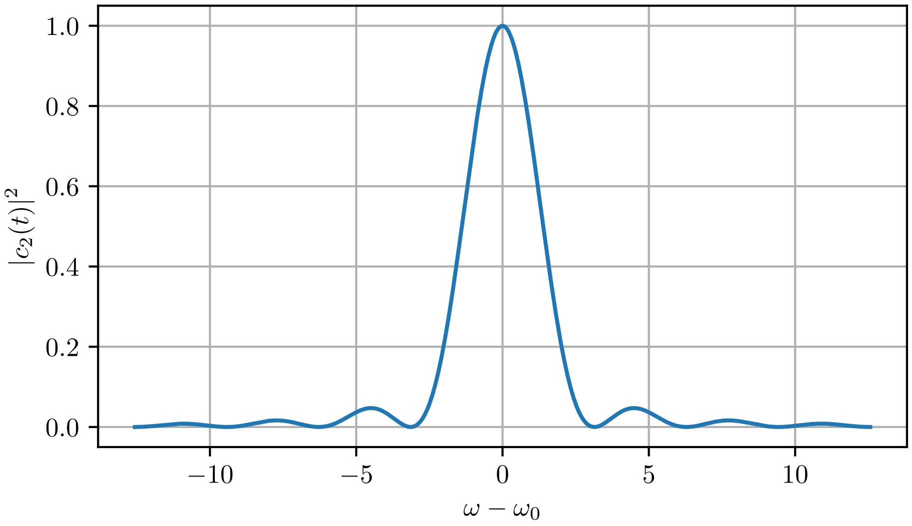

Figure 3: Probability coefficient $|c_2(t)|^2$ for the upper state $|2\rangle$ with $t = 2$ and $\Omega = 1$ plotted against the detuning $\omega - \omega_0$.

The general case for any incoming light frequency leads to the following probability coefficient [5]

$$|c_2(t)|^2 = \frac{\Omega^2}{W^2}\sin^2\left(\frac{Wt}{2}\right), \tag{3.11}$$

with $W^2 = \Omega^2 + (\omega - \omega_0)^2$. Plotting the time dependency (Figure 4) for the case of resonance $\omega = \omega_0$ and $W = \Omega$ shows an oscillation $\sim \sin^2(\Omega t)$ where the population oscillates between the two levels with the Rabi frequency Ω.

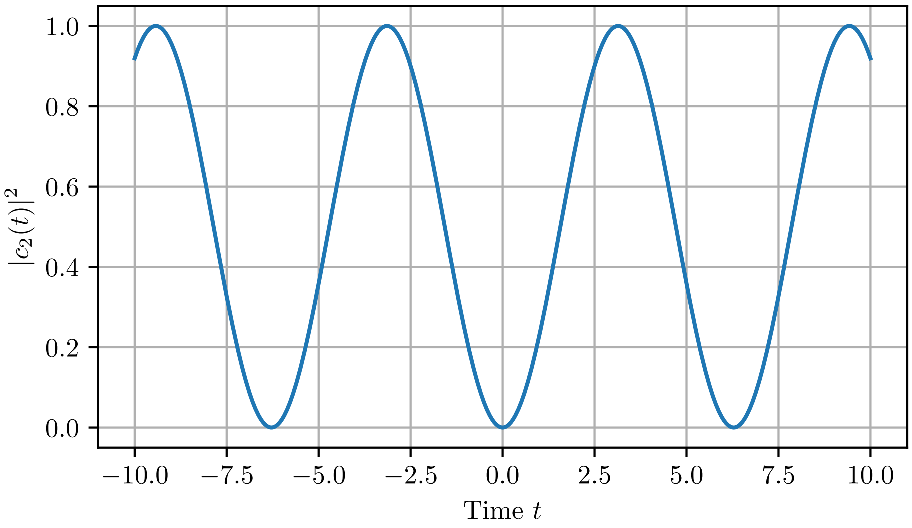

Figure 4: Probability coefficient $|c_2(t)|^2$ for the upper state $|2\rangle$ with $\Omega = 1$ and $\omega = \omega_0$ plotted against the time.

Sending a pulse with duration $\Omega t = \pi$ transfers the complete population into the excited state. This special pulse is called π-pulse. After $\Omega t = 2\pi$ it radiates back in the inital state.

One common way describing two-level systems are density matricies. For this system there are easily obtained from the outer product of $|\Psi\rangle$ and $\langle\Psi|$

$$|\Psi\rangle\langle\Psi| = \begin{pmatrix} c_1 \\ c_2 \end{pmatrix} \begin{pmatrix} c_1^* & c_2^* \end{pmatrix} = \begin{pmatrix} |c_1|^2 & c_1 c_2^* \\ c_2 c_1^* & |c_2|^2 \end{pmatrix} = \begin{pmatrix} \rho_{11} & \rho_{12} \\ \rho_{21} & \rho_{22} \end{pmatrix}, \tag{3.12}$$

where the diagonal elements ρ_{11}, ρ_{22} are the populations and the offdiagonal elements coherences. Introducing new variables

$$\tilde{c}_1 = c_1 e^{-i\delta t/2} \tag{3.13}$$

$$\tilde{c}_2 = c_2 e^{i\delta t/2} \tag{3.14}$$

with $\delta = \omega - \omega_0$ and splitting real and imaginary part yields

$$u = \tilde{\rho}_{12} + \tilde{\rho}_{21} \tag{3.15}$$

$$v = -i(\tilde{\rho}_{12} - \tilde{\rho}_{21}). \tag{3.16}$$

After some calculation (can be seen in [5]) the following set of equation arises

$$\dot{u} = \delta v \tag{3.17}$$

$$\dot{v} = -\delta u + \Omega w \tag{3.18}$$

$$\dot{w} = -\Omega v \tag{3.19}$$

where $w = \rho_{11} - \rho_{22}$. These equations are known as Bloch equations [5]. On a Bloch sphere (Figure 5) the Bloch vector

$$\boldsymbol{R} = u\hat{\boldsymbol{e}}_1 + v\hat{\boldsymbol{e}}_2 + w\hat{\boldsymbol{e}}_3 \tag{3.20}$$

represents the current state of the atom/molecule. Because $|\boldsymbol{R}|^2$ remains constant, the Bloch vector only reaches points on the surface.

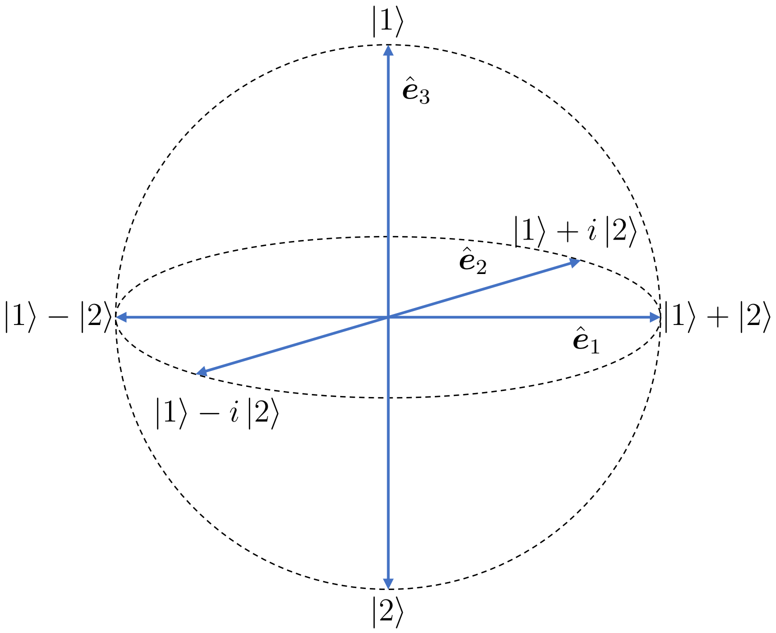

Figure 5: Bloch sphere representing all states which can be reached in a two-level system.

When introducing spontaneous decay, one has to expand the Bloch equations by a damping factor Γ

$$\dot{u} = \delta v - \frac{\Gamma}{2} u \tag{3.21}$$

$$\dot{v} = -\delta u + \Omega w - \frac{\Gamma}{2} v \tag{3.22}$$

$$\dot{w} = -\Omega v - \Gamma(w-1) \tag{3.23}$$

They behave the same as the first introduced Bloch equation for timescales much shorter than damping or relaxation times in the system.

Resonance fluorescence For a steady state solution in the excited state the population settles to [6]

$$\rho_{22}(t \to \infty) = \frac{(\Omega/2\pi\Gamma)^2}{1 + 4(\Delta/\Gamma)^2 + 2(\Omega/2\pi\Gamma)^2}. \tag{3.24}$$

Subsequently the total photon scattering rate by integrating over all directions and frequencies is given by

$$\Gamma\rho_{11}(t \to \infty) = R_{\text{scatter}} = \left(\frac{\Gamma}{2}\right) \frac{(I/I_{\text{sat}})}{1 + 4(\Delta/\Gamma)^2 + (I/I_{\text{sat}})} \tag{3.25}$$

where $I_{\text{sat}} = c\epsilon_0\Gamma^2\hbar^2/(4|e\boldsymbol{r}|^2)$ is defined as the value where the on-resonance scattering cross section σ drops to $1/2$. The scattering cross section σ is proportional to $R_{\text{scatter}}(\Delta = 0)/I$ and given by

$$\sigma = \frac{\sigma_0}{1 + 4(\Delta/\Gamma)^2 + (I/I_{\text{sat}})} \tag{3.26}$$

where the on-resonance cross section is $\sigma_0 = \hbar\omega\Gamma/(2I_{\text{sat}})$.

3.1.2 Broadening mechanisms

In reallife experiments many factors come into play which influence the absorption line width. Pressure and power lead to inhomogenious Lorentzian broadening, whereas Doppler and transit-time result in homogenious Gaussian broadening. In the following section these types of broadening effects are briefly explained [5, 7].

Doppler broadening Moving particles show Doppler broadening. In the laboratory frame the frequency ω' can be expressed as

$$\omega' = \omega - kv \tag{3.27}$$

where ω is the frequency of the moving particle system, v the velocity and k the wave vector $k = \omega/c$. This is shown in Figure 6.

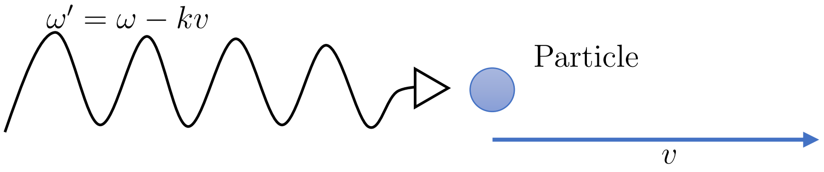

Figure 6: Doppler effect of a moving particle with velocity v. Absorption in the laboratory frame is only possible for $kv = \omega_\text{L} - \omega_0$.

For absorbing photons the following has to be fullfilled

$$kv = \omega_\text{L} - \omega_0 = \Delta. \tag{3.28}$$

Assuming a Maxwell-Boltzmann-Distribution of moving particles the Doppler broading $\Delta\omega_{\text{Doppler}}$ then is given by [5]

$$\Delta\omega_{\text{Doppler}} = \frac{\omega_0}{c}\sqrt{\frac{8\ln(2)k_\text{B}T}{m}} \tag{3.29}$$

with k_B the Boltzmann constant, T the temperature and m the mass of the particle. The standard deviation σ of a Gaussian Maxwell-Boltzmann distribution is given by the relation

$$\Delta\omega_{\text{Doppler}} = \frac{\sqrt{2\ln(2)}\sigma}{\pi}. \tag{3.30}$$

Transit-time broadening While particles fly through a laser beam with diameter d, they can interact for a transit time $t = d/\overline{v}$ (shown in Figure 7). The free mean velocity $\overline{v}$ in an ideal gas is given by [7]

$$\overline{v} = \sqrt{\frac{8k_\mathrm{B}T}{m\pi}}. \tag{3.31}$$

This time can also be longer than the lifetime of a state τ. Then the frequency-shift $\Delta\omega_\mathrm{Transit}$ occurs due to the passed transit-time for a Gaussian-shaped laser beam

$$\Delta\omega_\mathrm{Transit} = \frac{4\overline{v}}{2\pi d}\sqrt{2\ln(2)}. \tag{3.32}$$

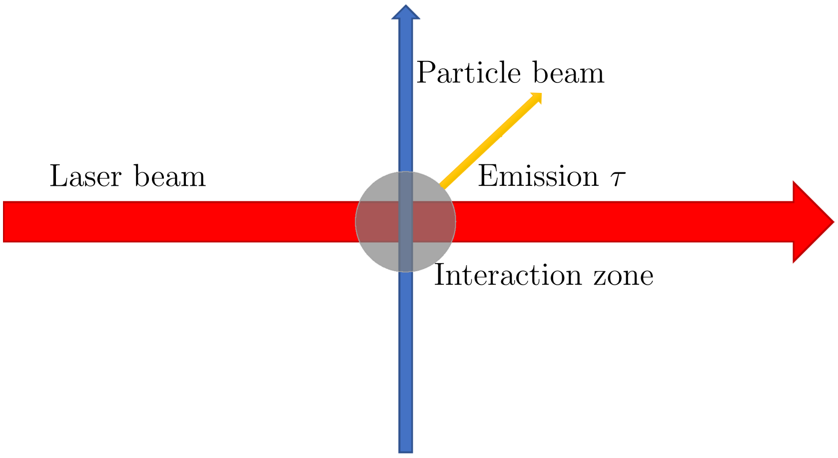

Figure 7: Particles excited by the laser beam perpendicular can interact as long as they travel through the beam. Transit-time broadening occurs if emission happens for lifetimes τ shorter than the transit time.

Pressure broadening Moving particles at velocity $\overline{v}$ can collide with each other reducing the lifetime of excited states. This leads to a broadened line width $\Delta\omega_\mathrm{Pressure}$ [7]

$$\Delta\omega_\mathrm{Pressure} = \frac{n\sigma\sqrt{2\overline{v}^2}}{2\pi}, \tag{3.33}$$

where n is the particle density, σ the cross section of two classical particles $\sigma = \pi(r_1+r_2)^2$ with $r_{1,2}$ the radii of particle 1/2 and the already known free mean velocity $\overline{v}$.

Power broadening Absorption at resonance can become saturated. If the densitiy is further increased, the absorption close to the resonance is reduced whereas the absorption within line width remain unchanged. This then broadens the overall line width $\Delta\omega_\mathrm{Power}$ by the [5]

$$\Delta\omega_\mathrm{Power} = \frac{\Gamma}{2\pi}\sqrt{1+\frac{I}{I_\mathrm{sat}}}, \tag{3.34}$$

where Γ is the inverse life-time introduced in the Bloch-equations, I the applied intensity and I_{sat} the saturation intensity which can be qualified by

$$I_{\text{sat}} = \frac{\pi}{3}\frac{\Gamma hc}{\lambda^3} \tag{3.35}$$

with c the speed of light and λ the wavelength.

3.2 Nitric oxide

Before treating the actual nitric oxide molecule, a short introduction into the diatomic structure theory should be made. The following explanation is based on [8, 9].

The total energy of a molecule is composed of three partial energies: electron energy, vibrational energy and rotational energy. Whereas for atoms the known quantum numbers n (principal quantum number), l (angular momentum quantum number), m_l (magnetic quantum number) and m_s (spin quantum number) can be used, l may be no longer a good quantum number (depending on the state's respective Hund's case [9]) in molecules due to the broken symmetry caused by the change in the Coulomb field. New parameters are introduced in molecular physics to describe this which are shown in the following list:

- J: total angular momentum
- Λ: orbital angular momentum
- N: rotational quantum number
- S: overall spin
- Σ: total electronic spin
- $\Omega = |\Lambda + \Sigma|$: total electronic angular momentum

According to these new definitions, molecular states are written as

$$\mathfrak{S}\ {}^{2S+1}\Lambda^{\pm}_{\Omega,(g/u)} \tag{3.36}$$

where $\mathfrak{S}$ labels configuration. X is the ground state, followed by A, B, C, ... corresponding to the first, second, third, ... excited state. For the ground state and the excited state not having the same multiplicity $2S+1$ lower case letters are used. Because historically some intermediate states were discovered later, an apostrophe is added for these states. The orbital angular momentum Λ which ranges from 0, 1, 2, 3, ... gets assigend greek letters $\Sigma, \Pi, \Delta, \Phi$, ... instead of numbers. The subscript g/u indicates parity with respect to inversion. ± shows if the state has a reflection symmetry along a plane containing the internuclear axis.

Not all electronic state transitions are allowed. By treating the electric dipole transitions in first-order perturbation theory, following selection rules arise with associated labeling

$$\Delta J = +1 \qquad R \text{ branch} \tag{3.37}$$

$$\Delta J = 0 \qquad Q \text{ branch} \tag{3.38}$$

$$\Delta J = -1 \qquad P \text{ branch} \tag{3.39}$$

whereby $\Delta J = 0$ is not allowed for the case that both states are in $\Lambda = 0$.

Nitric oxide Nitric oxide (NO) is a paramagnetic radical [10]. It has a mass of $m = 30\,\mathrm{u}$ and occurs most frequently as isotope $^{14}\mathrm{N}^{16}\mathrm{O}$. The heavly toxic and colorless gas reacts to NO_2 if exposed to air [11]. Since it has on unpaired electron in the anti-bonding orbital, the total spin is $S = 1/2$. The orbital occupation of NO in one of the two ground states (here X $^2\Pi_{1/2}$) is shown in Figure 8.

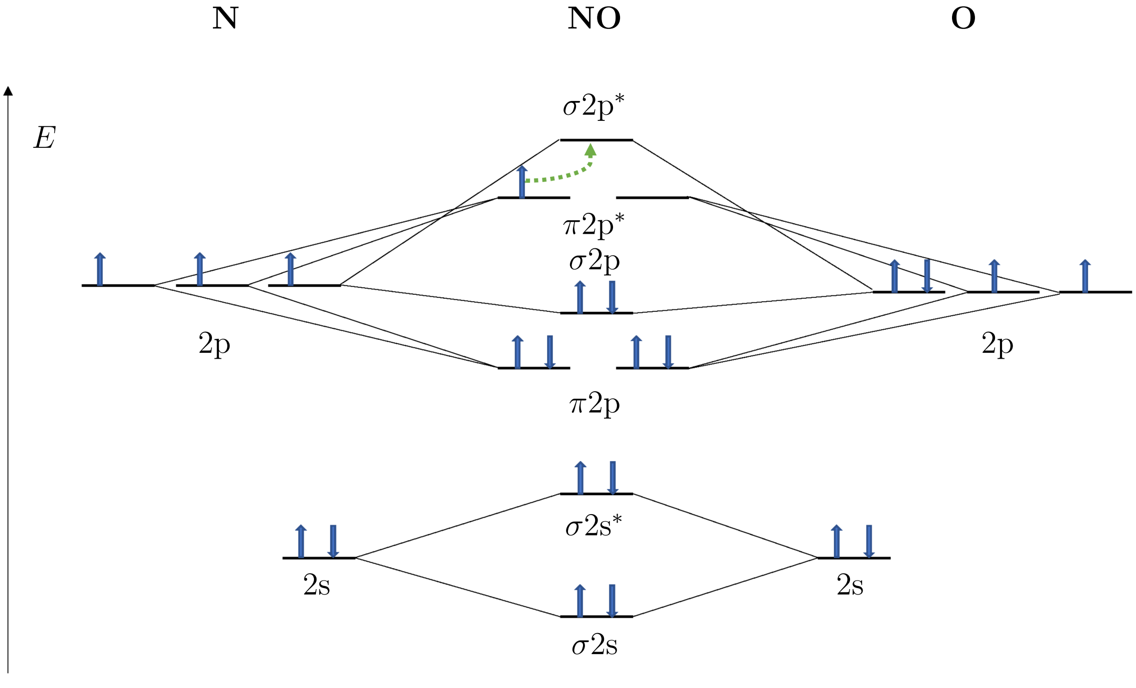

Figure 8: Orbital occupation of NO in the ground state X $^2\Pi_{1/2}$. The 1s occupation is not shown. The dotted arrow indicates the transition of the electron to the first exited state A $^2\Sigma^+$.

The project on which this thesis is based on uses three lasers to excite NO molecules from the ground state X $^2\Pi_{3/2}$ into a Rydberg state $^2\Sigma$ [12, 13]. The experimental setup will be further explained in chapter **Methods**. The ground state $^2\Pi$ has an orbital angular momentum of $\Lambda = 1$ and therefore two different total electrical angular momenta $\Omega = 1/2, 3/2$ which leads to the two ground states X $^2\Pi_{1/2}$ and X $^2\Pi_{3/2}$. The 3/2 state lies slightly above the 1/2 by 0.015 eV [13]. Because of thermal excitation in the regime $\sim 0.076\,\mathrm{eV}$ most of the 3/2 states are occupied [13, 12]. Figure 9 shows the excitation scheme for the used experimental setup, (a) and (b) show the substructure for the UV transitions. The transition wavelenght from the ground state X $^2\Pi_{3/2}$ into the first excited state A $^2\Sigma^+$ is at around 227 nm. Figure 10 illustrates simulated transition intensities in the range of the measured excitation. The $P(J' = 11/2)$ transition refers to a wavelength of 226.97 nm. As one could see, there is an additional peak just next to the desired transition which correspond to the $P(J' = 32/2)$ branch. For this simulation, a temperature of $T = 300$ K is assumed which leads to a Doppler broadening of 3 GHz was calculated (see in chapter **Results**).

In this work, the UV light detection was accomplished by gathering fluorescence light. Figure 11 shows the excitation and relaxation process producing the fluorescence light. The emitted light only originate from spontaneous emission, because the light from stimulated one goes in the direction of the laser beam [14] (see later in experimental setup). Since the transition a $^4\Pi \rightarrow$ X $^2\Pi$ is dipole forbidden and not observed [15, 16] and the transition a $^4\Pi \leftarrow$ A $^2\Pi^+$ is located in the IR, one likely occuring transition lies in the desired UV range. In the experiment, only excitations with $\nu = 0$ are possible, since the next higher vibration states are energetically too far away.

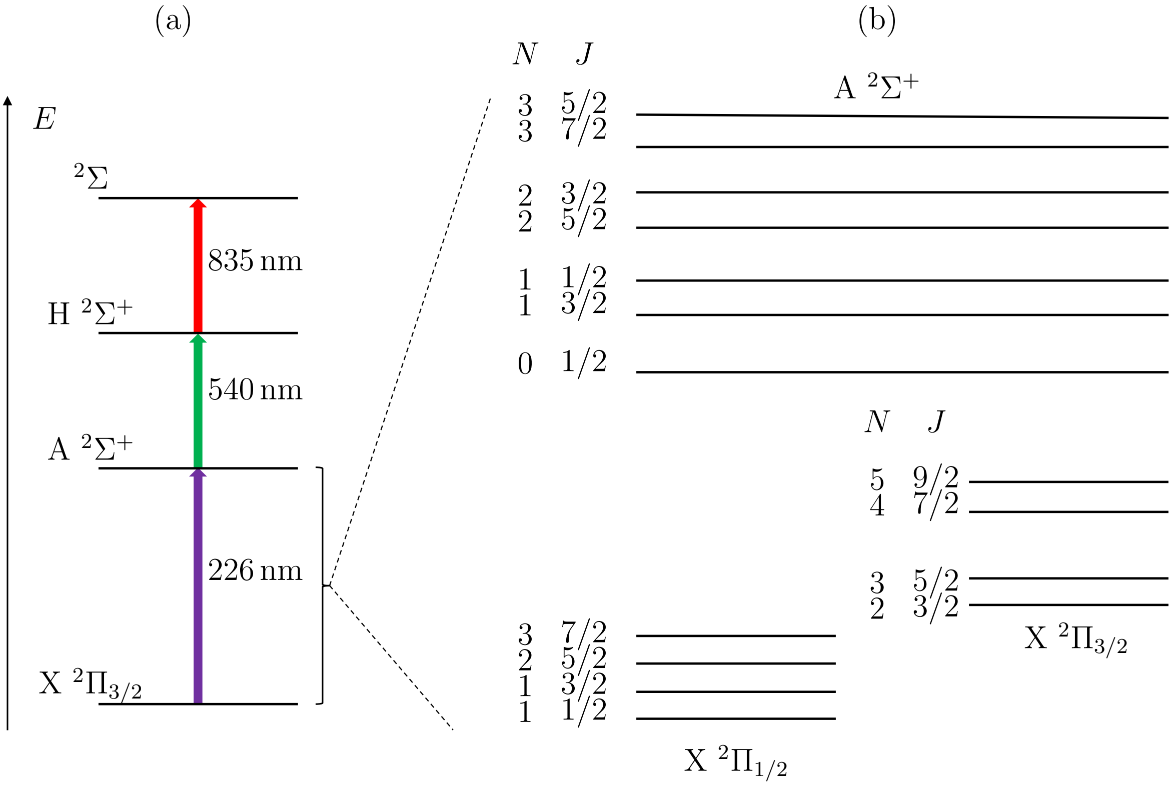

Figure 9: (a) Three photon excitation scheme for the experimental setup.(b) Energy levels for the NO transition from the ground state into the first excitated state. The shown states correspond to a vibrational quantum number of $\nu = 0$. Adapted from [13]

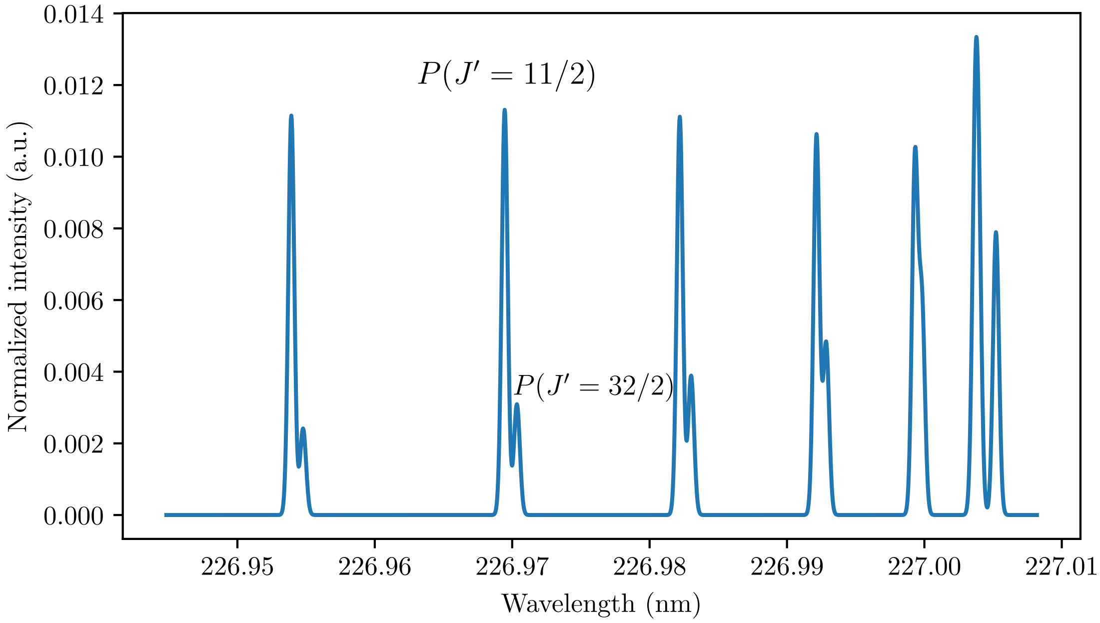

Figure 10: Simulated transition intensities for wavelengths $\sim 227\,\text{nm}$. The $P(J' = 11/2)$ is the used excitation. Simulation was done with *pGopher* [17] and parameters $T = 300\,\text{K}$ and a Gaussian broadening of $3\,\text{GHz}$.

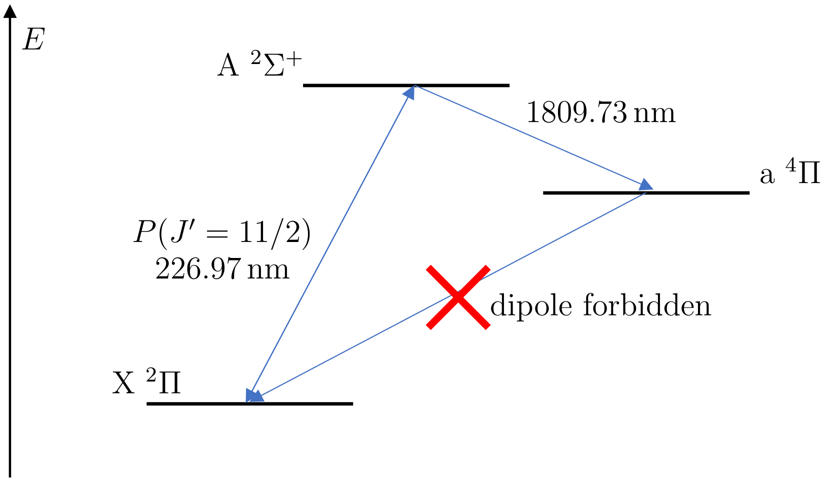

Figure 11: UV absorption and emsission through fluorescence. The excitation from the ground state X $^2\Pi$ into the first excited state A $^2\Sigma^+$ can decay directly back into the ground state or by IR emission into an a $^4\Pi$ state. Decays into other vibrational levels are also possible.

3.3 Thin film technology

This thesis presents semiconductor devices that were manufactured at the Institute for Large Area Microelectronics (IGM) located at the University of Stuttgart. The devices were created by utilizing thin film materials and using a range of manufacturing techniques. This chapter provides a brief summary of the production methods used to fabricate photodiodes. Sketch 12 shows an overview of the sequence of production steps. For more details about the individual steps, see [18, 19, 20].

Sputtering Sputtering is a common technique used for depositing thin film materials onto a substrate. Sputtering involves creating a plasma that moves ions towards a material target. The high-energy ions hit the target and release material, forming a new layer on the substrate. Two types of plasma, DC and RF, can be used to create ions, but a DC plasma needs a conductive target while an RF plasma can work with non-conductive materials. This study used both DC- and RF-sputtering to deposit metal and semiconductor.

Plasma-enhanced chemical vapor deposition Plasma-enhanced chemical vapor deposition (PECVD) is a technique commonly used to deposit dielectrics or amorphous semiconductors. This method involves heating a substrate and bringing precursor elements in a gas state to its surface. The desired molecule is deposited onto the substrate after the individual precursor elements have reacted in the plasma to form the intended molecule. The heat provides energy for a reaction between the precursors, but creating a plasma of the gas-phase elements reduces the temperature required for the reaction. This is the primary advantage of PECVD over regular chemical vapor deposition because it reduces the thermal enviroment of the process. The reaction rate depends on the temperature and precursor concentration in the chamber.

Lithography In semiconductor fabrication, a glas substrate in our case, the deposited layers are structured by optical lithography, which involves three or four basic steps. Firstly, the photoresist is deposited on the glas surface and evenly spread using a spin coating. Then, the wafer is exposed to UV radiation and aligned to the mask to create a desired pattern. For each layer another mask is needed. The exposed areas are removed using a developer solution, leaving the desired pattern on the surface. A hard bake may be applied to increase the photoresist's resilience against etching. Finally, the wafer is ready for the structuring of the desired layer.

Etching To remove the structures prepared with lithography, the material must be etched. Various approaches can be utilized for this purpose.

Wet Chemical Etching:
To remove materials from a wafer, a corrosive liquid is used in a process called wet etching. It can be adjusted to selectively etch specific materials and works quickly. Usually, this is isotropic etching, which can lead to under-etching of the structures. However, if the liquid is used along with other materials, it may pollute the substrate

with remaining nanoparticles from these processes.

Plasma Etching (reactive ion etching):
Plasma etching uses a reactive plasma to remove material from the surface of a wafer. There, the reaction gases corrode the exposed surface layer, inducing material to be removed in the process. Since plasma etching is machine controlled, anisotropic etching processes can also be performed, which can prevent under-etching of the structures.

In the last step, the remaining photoresist get removed by placing the substrate in an ultrasonic bath filled with different solvents.

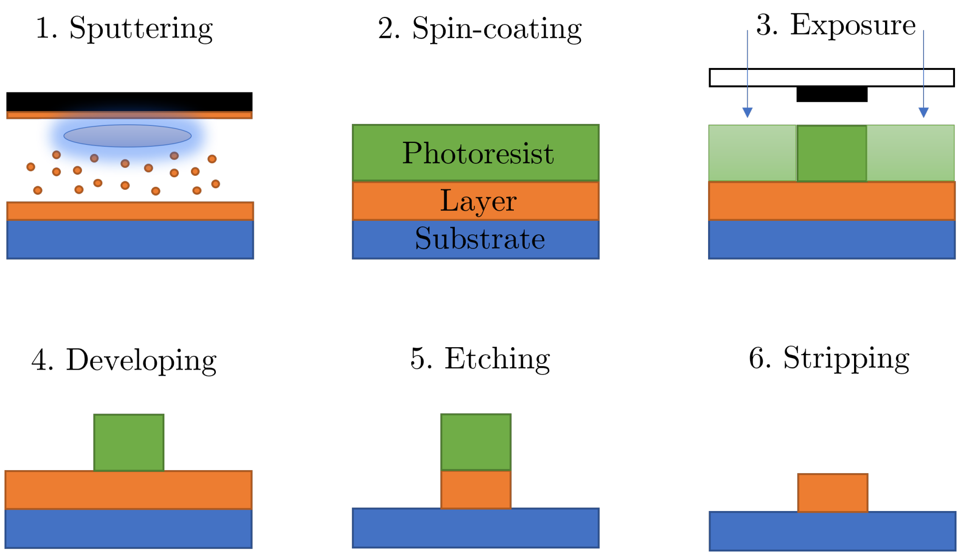

Figure 12: Typical structuring steps of thin films. Adapted from [19].

3.4 Semiconductor

Semiconductors are materials that show intermediate electrical conductivity between conductors and insulators. They are essential components in modern electronic devices, including transistors, diodes, and integrated circuits. The unique electrical properties of semiconductors, such as their ability to switch between conducting and non-conducting states when applying an external electric field, make them useful for controlling the electrical current in electronic devices. This chapter will introduce the highly used p-n junction and Schottky contact which will be used as base for the in this thesis underlying IGZO diodes. Further details about the topics can be found in [21, 22].

3.4.1 p-n junction

Doped semiconductors are classified into two types: n-type and p-type. The classification is based on the location of a new arising energy level lying between the valence and conduction band. Because of the excess of electrons in n-type semiconductors, a donator-niveau forms nearby the conduction band whereas for p-type the lack of electrons result in an acceptor niveau near the valence band. If one brings n- and p-type semiconductors together spatially, they form a p-n junction. Figure 13 shows both semiconductor types before contact (top) and after contact (bottom). E_L indicates the conductor band niveau, E_V the valence band. The Fermi energy E_F lies slightly above the acceptor niveau E_A for p-type and slightly below the donator niveau E_D for n-type semiconductors. If both types are brought together, the Fermi energy aligns to one constant level and a potential $-eV_\mathrm{D}$ arises which is characterized by the diffusion voltage V_D. This quantity is given by [21]

$$eV_\mathrm{D} = E_\mathrm{g} - k_\mathrm{B}T \ln\left(\frac{N_\mathrm{eff}^\mathrm{L} N_\mathrm{eff}^\mathrm{V}}{N_\mathrm{D} N_\mathrm{A}}\right) \tag{3.40}$$

with E_g being the band gap, $N_\mathrm{D/A}$ being the charge carrier concentrations and N_eff being the effective overall particle densitiy $N_\mathrm{eff} = 2\left(\frac{2\pi m^* k_\mathrm{B}T}{h^2}\right)^{3/2}$. Here m^* is the effective mass for electrons/holes. The reason for the emerging of V_D is charge compensation. Charges diffuse from areas of higher concentration such with lower ones. Electrons flow from the n- to the p-side and the other way around to recombinate. The absence of the charge carriers can not be compensated locally which build up a space charge balancing the diffusion charge. This then remains the system in an equilibrium state.

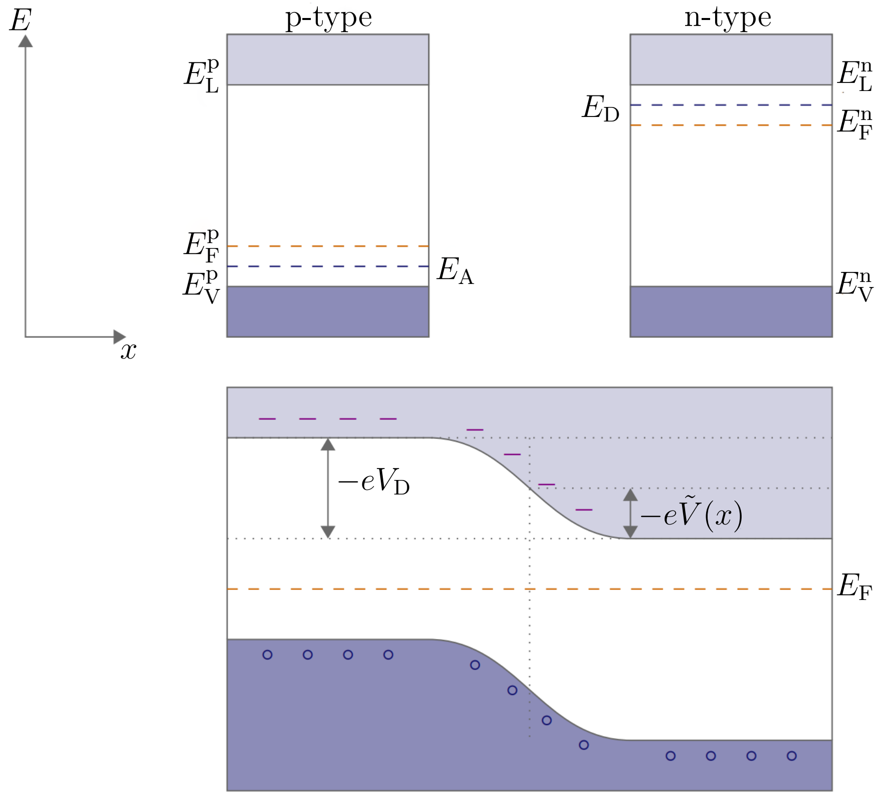

Figure 13: p-n junction sketch before contact (top) and after (bottom). Additionaly the impurity levels $E_\mathrm{A/D}$, the band levels $E_\mathrm{V/L}$ and the Fermi level E_F are marked. Since the charges are not in equilibrium anymore by appling a potential $\tilde{V}(x)$, there is no common Fermi level. Taken and modified from [22].

Of great interest is the impact of an external voltage U. If the junction is switched in forward direction (positive pole on p side and negative pole on n side) the potential which arises from the diffusion voltage will decrease, contrary to this in blocking direction where the overall potential will increase. The external voltage drops almost entirely in the space charge area therefore the remaining region in nearly zero field. This behaviour can be seen in Figure 14. Since both holes and electrons contribute to the total current density $j(U)$, this results in

$$j(U) = j_{\mathrm{S}}(e^{eU/k_{\mathrm{B}}T} - 1), \tag{3.41}$$

where j_{S} is the condensed current density. This can be calculated via

$$j_{\mathrm{S}} = \left(\frac{eD_{\mathrm{p}}}{\sqrt{D_{\mathrm{p}}\tau_{\mathrm{p}}}} p_{\mathrm{n}} + \frac{eD_{\mathrm{n}}}{\sqrt{D_{\mathrm{n}}\tau_{\mathrm{n}}}} n_{\mathrm{p}} \right) \tag{3.42}$$

where τ is the lifetime of electrons/holes, p_{n} is the electron density in the p-area, and n_{p} the hole density in the n-area. The diffusion coefficient D is linked to the mobility μ of electrons and holes $D_{\mathrm{p,n}} = k_{\mathrm{B}}T\mu_{\mathrm{p,n}}/e$. Graph 3.41 shows the typical current behaviour of equation 3.41 for p-n diodes. The leakage current for the wiring in blocking direction j_{S} remains constant in an idealised case. In reality a breakthrough occurs at a certain voltage.

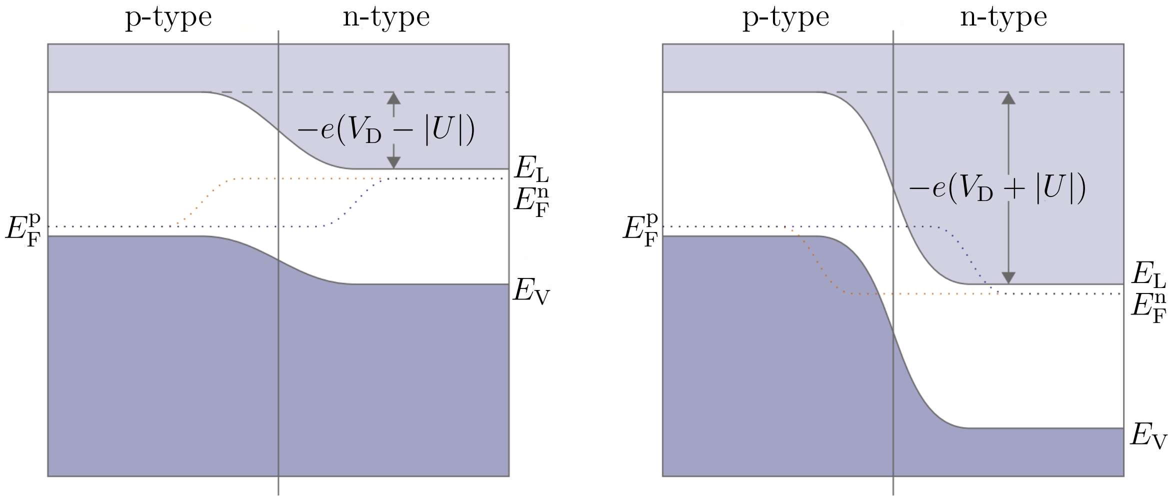

Figure 14: p-n junction being subject to an external voltage U. The left side shows a voltage in forward direction, leading to an overall smaller potential, the right side shows the opposite wiring in blocking direction. Additionaly the impurity levels $E_{\mathrm{A/D}}$, the band levels $E_{\mathrm{V/L}}$ and the Fermi level E_{F} are marked. Taken and modified from [22].

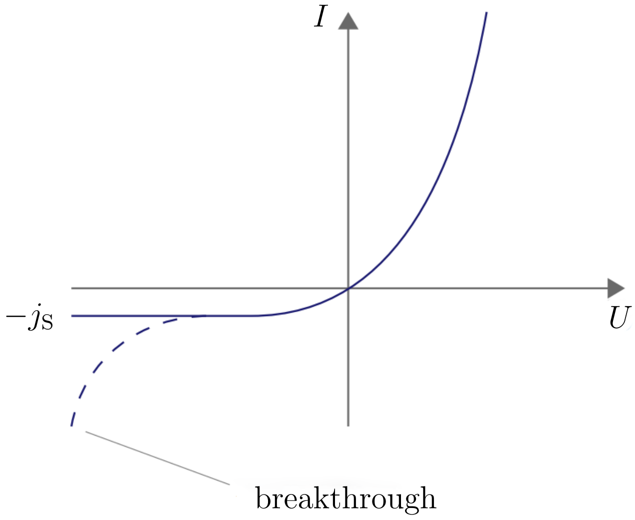

Figure 15: U/I characteristic for a p-n diode. The dotted line shows the real case for a breakthrough after a certain voltage whereas the blue line assumes an ideal scenario. Taken and modified from [22].

3.4.2 Schottky contact

In contrast to a pure p-n junction, one side of a metal-semiconductor interface is a metal, the other one a semiconductor. In this case, an n-doped semiconductor is assumed. The work required to push an electron out of a metal/semiconductor into a vacuum is called the work function and is defined as $\phi = E_\mathrm{vak} - E_\mathrm{F}$ furthermore the electron affinity $\chi = E_\mathrm{vak} - E_\mathrm{L}$ is the distance from the lower conduction band edge to the vacuum level. Figure 16 shows the case $\phi_\mathrm{ME} < \phi_\mathrm{SE}$ on top and below the case $\phi_\mathrm{ME} > \phi_\mathrm{SE}$. The respective left side shows the case before contact, the right side depicts the case after contact.

For $\phi_\mathrm{ME} < \phi_\mathrm{SE}$ electrons flow from the metal to the semiconductor. Due to the negative space charge in the semiconductor, the conduction band edges of the semiconductor are curved downwards. As a result, the Fermi level lies in the conduction band of the n-semiconductor and a strong concentration of electrons occurs in the semiconductor. If an external voltage is applied, the electrons can flow across the interface without interferences. Therefore this type of contact is called *Ohmic contact* with its characteristic linear behaviour ($I = U/R$) no matter in which direction the voltage is applied.
For $\phi_\mathrm{ME} > \phi_\mathrm{SE}$ the formation of the space charge zone can be understood by the fact that a part of the electrons existing in the n-semiconductor diffuses into the metal. In the boundary layer of the n-semiconductor, a positive space charge zone is then formed. However, due to the high charge carrier density in the metal, the spatial expansion in the metal is small compared to a p-n junction. For a positive voltage (forward direction), the potential on the side of the metal is raised. For a negative

voltage (reverse direction), it is exactly the opposite. In the forward direction, the potential barrier which the electrons in the conduction band of the n-semiconductor have to overcome in order to enter the metal is lowered, so that the current increases exponentially with the voltage like in a p-n junction (Equation 3.41). In the reverse direction, the potential barrier is increased so that the current reaches a saturation value with increasing negative voltage, because the electrons can no longer overcome the potential. This form of contact is then called *Schottky contact*.

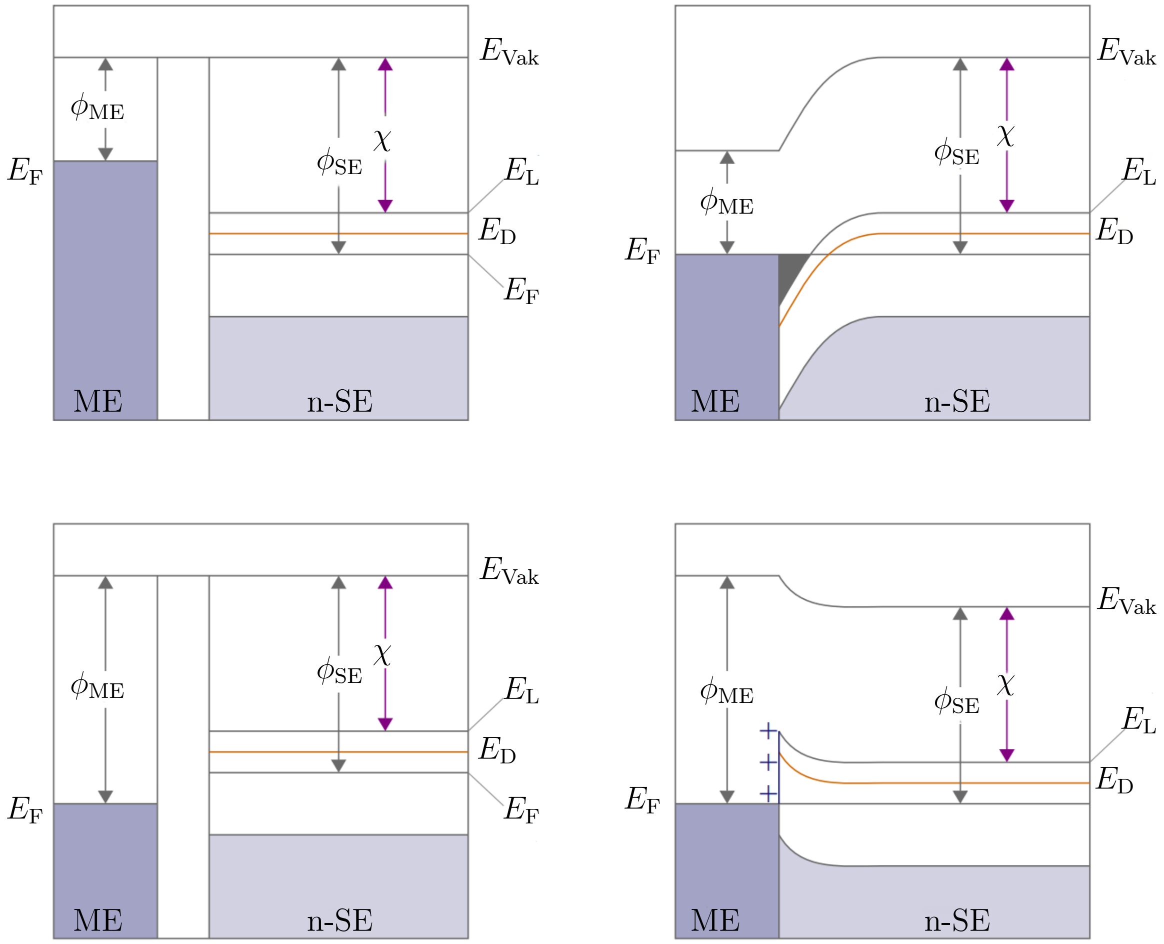

Figure 16: Metal-n-type-semiconductor before contact (left side) and after contact (right side). The upper row shows the case $\phi_{\mathrm{ME}} < \phi_{\mathrm{SE}}$, whereas the lower one $\phi_{\mathrm{ME}} > \phi_{\mathrm{SE}}$ where ϕ_{ME} is the work function for the metal and ϕ_{SE} the semiconductor. χ is the electron affinity. Taken and modified from [22].

3.4.3 Indium-gallium-zinc-oxide (IGZO)

Indium-gallium-zinc-oxide is a relativly new metal oxide semiconductor which shows promising results in display technology, sensing devices and neuromorphic systems [2]. Amorphous IGZO is particularly interesting, as it can be sputtered evenly over large areas and is deposited at relatively low process temperatures for modest costs. A schematic sketch of the structure of a-IGZO can be seen in Figure 17. With a bandgap located between $3 - 4\,\mathrm{eV}$ [23, 24, 1, 25] it's transparent to visible light and therefore can be used as an UV sensor not being affected by visible background light.

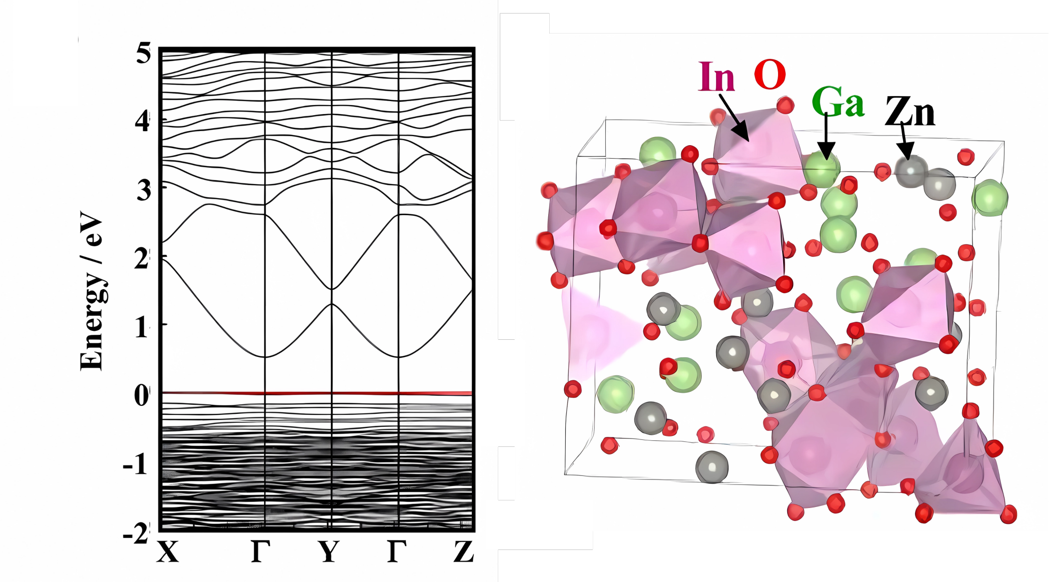

Figure 17: Left: Pseudo bandstructure of amorphous IGZO. The zero level is measured from E_{G}. Right: Polyhedral notion of amorphous IGZO. Taken from [26].

Figure 18 shows an absorption measurement of a-IGZO on a quartz glass substrate. It cleary shows significantly increasing absorption below 400 nm. On the left in Figure 17 the bandstructure indicate noticeable absorption increase for excitations above 3 eV because of the high conduction band concentration.

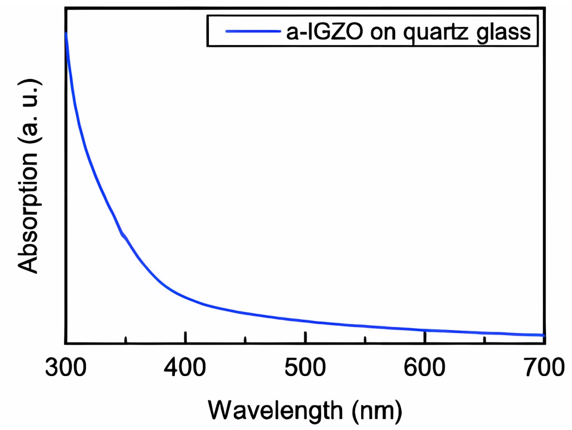

Figure 18: Absorption of a-IGZO on a quartz glas substrate. Taken from [27].

The conductivity arises primarily from the electrons, because the mobility of the holes is negligible and makes no contribution to the charge flow [28, 26]. This can be explained by the fact that in the IGZO the conduction band is formed by s-orbitals of the metal, whereas the valence band is formed by the oxygen 2p orbitals (illustrated in Figure 19). The spatial overlap of s-orbitals in contrast to p-orbitals is significantly larger [29].

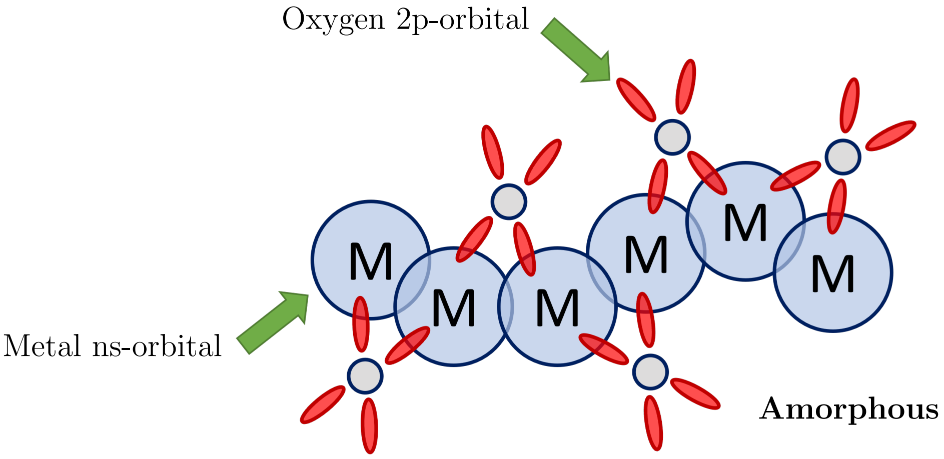

Figure 19: Schematic drawing of oxide semiconductor orbitals for crystaline and amorphous structures. Adapted from [30].

3.4.4 Photodiode characteristics

This section will briefly introduce some of the key characteristics of a photodiode [31].

Dark current (I_{dark}) The current that flows through the photodiode in the absence of light. In the ideal case this should be zero.

Photosensitive area This is the area of the photodiode that responds to light. The photocurrent results only from applying a voltage. Seperation of free electrons and holes takes place in the active region. Irradiated light then excites electrons from the valence to the conduction band which produces a current.

Rise and fall time (τ_{rise} & τ_{fall}) The time required for the photodiode to respond to changes in light intensity (rise) and return to its initial state (fall). In this thesis the time is determined as a the time distance bewteen 10% and 90% of the photo current signal.

Signal-to-noise ratio (SNR) A measure used in signal processing to describe the ratio of the signal power to the noise power present in a given signal. Usually its definded by the power, but can also be calculated from the arising photocurrents, as

$P = U \cdot I$ where the voltage is kept constant by the power source.

$$\mathrm{SNR} = \frac{P_\text{signal}}{P_\text{noise}} = \frac{I_\text{signal}}{I_\text{noise}}. \tag{3.43}$$

Photosensitivity (PS) Measure of the optical switching ratio between the photocurrent without the darkcurrent diveded by the darkcurrent itself

$$PS = \frac{I_\text{signal} - I_\text{dark}}{I_\text{dark}}. \tag{3.44}$$

Responsivity (R) The ratio of the generated photocurrent to the incident light power indicating how efficient the diode converts light into an electrical signal.

$$R = \frac{I_\text{signal} - I_\text{dark}}{P}. \tag{3.45}$$

It should be mentioned that the power P is referring to the power the photosensitive area receives.

External quantum efficiency (EQE) The ratio of the number of charge carriers generated by the photodiode to the number of incident photons, which indicates how efficiently the photodiode converts photons into charge carriers

$$EQE = \frac{(I_\text{signal} - I_\text{dark})/q}{P/E_\text{photon}} \tag{3.46}$$

where q is the involved charge and E_photon is the energy of one single photon.

Noise-equivalent power (NEP) The sensitivity of a photodiode is given by the noise-equivalent power value. It is defined as the signal power that provides a SNR of one at an output bandwidth of 1 Hz,

$$NEP = \frac{P}{SNR(1\,\mathrm{Hz})}. \tag{3.47}$$

4 Methods

4.1 Photodiodes

This work presents a photosensor designed in a metal-semiconductor-metal configuration for detecting light. To begin, a thin layer of $\sim 150\,\mathrm{nm}$ of SiOx is applied on a glas substrate via plasma-enhanced chemical vapor deposition. This layer should provide a defined starting layer for the subsequent layers.
Moving on, the electrodes are made of a metal of choice which can be deposited via DC-sputtering. In the last step, the semicondcuctor is applied on top of the electrodes by RF-sputtering. In Figure 20, on the left side a simple layer stack design of such a photoresistor sensor is shown. Due to the nature of metals, Schottky barriers are formed at the interfaces between the metal electrodes and the semiconductor material. When producing an array of photosensors, it cannot be avoided to introduce an additional layer. In Figure 20 on the right side a microscope image of an array of photosensors is shown. The crossing of the metal conduction tracks (gold and pink color) are seperated using a dielectric. This project focused on producing and testing 8x8 photosensor arrays. In order to find out which parameters have an influence on the sensor and can be fabricated best, the following parameters were varied and tested:

- Type of metal used as electrodes
- Design and dimension of the individual sensors
- Layer thickness of the semiconductor material

The design of the layers was done using the software *KLayout*. An evaluation of these variations is given in the next chapter **Results**.

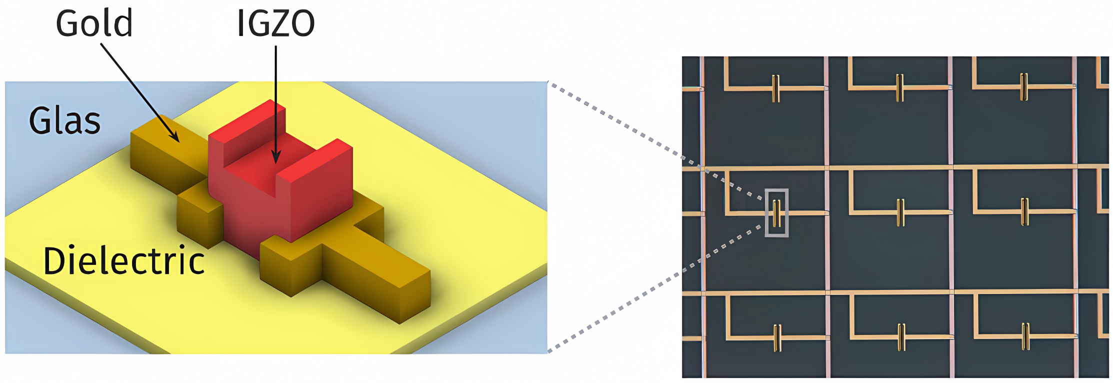

Figure 20: General layer structure of a Metal-Semiconductor-Metal photosensor using two gold electrodes and the corresponding use in an array of photosensors.

4.2 Readout

In order to be able to read out the photocurrent generated by the sensors and to be able to allocate it in the array, a circuit consisting of various components was developed. The general idea is based on multiplexing. This makes it possible to precisely control individual sensors. The structure and operation of the circuit is explained in this section. Figure 24 shows a schematic of the circuit.
When the sensors are illuminated with UV light, a photocurrent is generated due to the increased conductivity when a voltage is applied. Since small currents are generally more difficult to measure, it is beneficial to convert the current into a voltage. This can be realized by a transimpedance amplifier (TIA), schemed in Figure 21. Basically, this is an operational amplifier where the output node is fed back to the negative input node, which allows its gain to be adjusted by the feedback resistor. In Figure 24, this feedback resistor is R_1 which gives the gain factor. According to Ohm's law $I = U/R$ the current can be calculated by providing the measured voltage if an ideal operational amplifier is assumed.

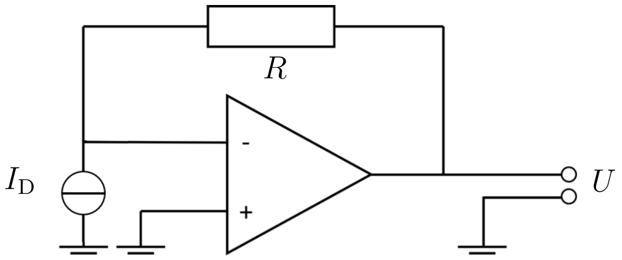

Figure 21: Schematic sketch of a transimpedance ampilifier. The input current I_D gets converted into a voltage U. The feedback resistor R controls the amplification factor.

Since the transimpedance amplifier outputs a negative voltage, it is useful to convert the signal into a positive voltage. The main reason is the Arduino can not deal with negative voltages at the analog input. This can be realized by an inverting amplifier (Figure 22). Basically, this is similar to the TIA, which has a second resistor as an additional component. The input voltage is applied to the negative input of the operational amplifier via resistor R_2 and part of the output voltage is fed back to the negative input of the operational amplifier via resistor R_3. The difference to the TIA is that here no current is converted into voltage but voltage into voltage. Since the inverting amplifier is only used to invert the voltage, the amplification ratio should be 1 according to $V = -R_3/R_2$ [32]. This can be easily achieved with two resistors of the same resistance.

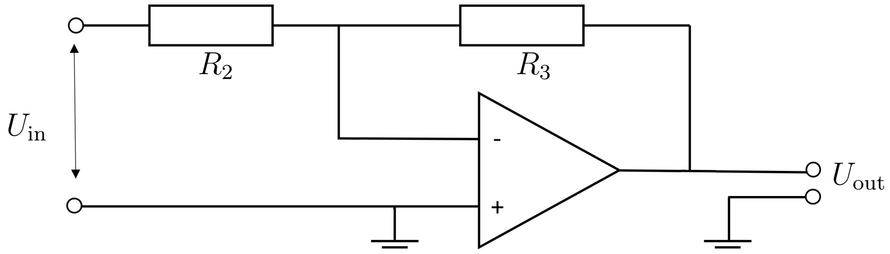

Figure 22: Schematic sketch of an inverting amplifier. The input voltage U_{in} gets converted into an amplified voltage U_{out} by a factor $V = -R_3/R_2$.

To make sure that no negative voltage is applied to the analog input of the Arduino, a diode is integrated into the circuit in forward direction. Since the analog input of the Arduino can read a maximum voltage of 5 V, it must be ensured that voltages below this value are present. Therefore a voltage divider is built from two resistors, R_4 and R_5. According to [33] the adjusted voltage is $U_{\text{adj}} = U \cdot R_4/R_5$.
To improve the measurement signal, a low-pass filter can be installed to reduce the 50 Hz noise which is picked up from the enviroment, as seen in Figure 23. This is installed between TIA and inverting amplifier, as one of the resistors (R_2) can be used to realize the low pass filter with a capacitance C. The cutoff frequency f_{g} can be calculated after [34] $f_{\text{g}} = (1/2\pi R_2 C)$.

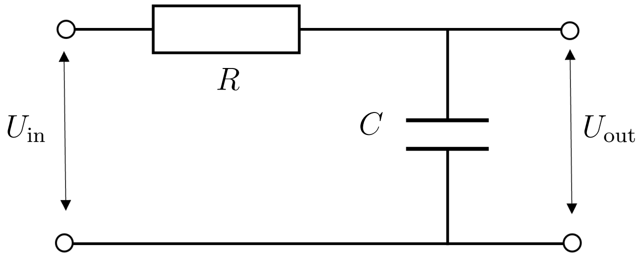

Figure 23: Schematic sketch of a lowpass filter.

With this simple circuit, a single sensor can be read by applying a voltage, e.g. $V_{\text{sensor}} = 5\,\text{V}$, to one side of the electrode and the negative input from the TIA to the other side. However, if an entire array is to be read and certain sensors in it are to be controlled, multiplexers are employed. Since in this project arrays of size 8x8 were produced, two multiplexers with 8 channels are also needed. The rows are connected to the outputs of one multiplexer and the columns to the outputs of the second multiplexer. By applying a voltage to the pins of the multiplexers, a dedicated channel can be opened. The applied sensor voltage V_{sensor} goes to the input of the first multiplexer, the output of the second to the TIA. Thus a special sensor can be addressed by correct switching. The switching is realized with the help of an Arduino and a script developed in C++ and Python within the scope of this project. More about this in section **Software**.

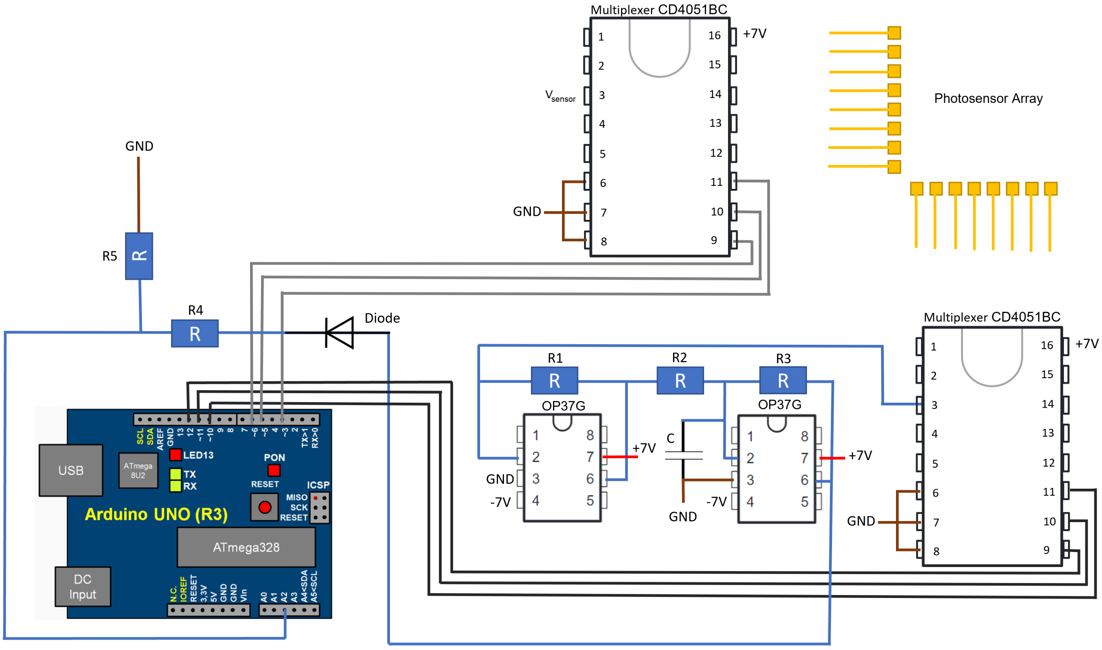

Figure 24: Schematic drawing of the utilized circuit. The multiplexers are used to select a specific sensor in the array. Two operational amplifiers first convert the diode current into a voltage (TIA) and then invert the output voltage. A low pass filter is used to reduce noise and a diode protects the Arduino from voltage spikes. The Sketch of the Arduino is taken from [35].

Since each row/column of the array would have to be pinned individually, an elegant solution is a flat ribbon cable. Figure 25 shows a schematic drawing of the photo array on the right, which is connected to a PCB (left side) using a flat ribbon cable.

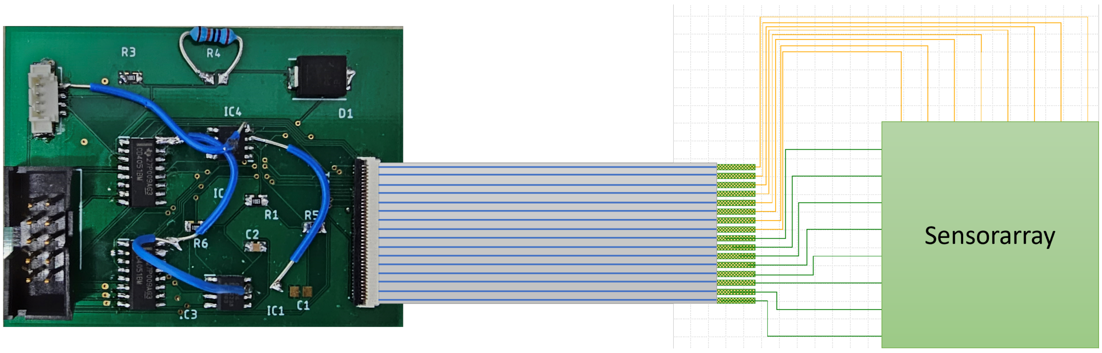

Figure 25: Sketch of the underlying connection between photosensor array and the circuit on a PCB.

Here is a list of the components used:

- Transimpedance amplifier: *OP37G*, feedback resistor R_1 variable
- Inverting amplifier: *OP37G*, $R_2 = R_3 = 100\,\mathrm{k\Omega}$
- Low-pass filter: $f_\mathrm{g} = 25\,\mathrm{Hz} \Rightarrow R_2 = 100\,\mathrm{k\Omega}, C \approx 60\,\mathrm{nF}$
- Voltage divider: $R_4 = 100\,\mathrm{k\Omega}, R_5 = 300\,\mathrm{k\Omega}$
- Multiplexer: *CD4051*
- Microcontroller: *Arduino Uno R3*

4.3 Software

In principle, it is possible to read out individual sensors if the multiplexers are manually switched to the correct channel. To automate the process and to be able to read out all photosensors quickly and efficiently, an Arduino Sketch loops through all channels of the multiplexer. This way all 64 sensors are read out in one run. The data is sent as a serial packet via the USB connection to a computer with a GUI (graphical user interface) written in Python. Using this GUI, various parameters can be adjusted and the measured values can be displayed directly.
Figure 26 shows the GUI during the measurement. All sensors are displayed in the correct arrangement and are highlighted by color coding of the measured voltage. The upper picture shows the case of displaying the measured raw data, the lower one a measurement after calibration. The color gradient is caused by a partial occlusion of the array.

Some of the core functions of the GUI are briefly explained below:

Dark current/ max value/ normal measurement In the normal measurement mode, the read voltage values are simply stored for a certain time for each sensor. To calibrate the sensors, the dark current measurement can be used to measure the voltage without illumination and subtract it from the raw data directly. This is easily done by $U_\mathrm{new} = U_\mathrm{raw} - U_\mathrm{dark}$. If a max value measurement is also made, a complete calibration is possible. The value is no longer displayed in volts, but as a percentage of the maximum measured value (see Figure 26 right). The value is calculated as follows: Percentage from maximum measured voltage value $= 100\% \cdot (U_\mathrm{raw} - U_\mathrm{dark})/(U_\mathrm{max} - U_\mathrm{dark})$.

Measure single/ all pixel The display can be switched between reading individual sensors (Measure single pixel) and all (Measure all pixel). Thus, a specific single sensor can be measured and also plotted time dependent via *Plot single pixel.*

Adjust delay The read out of the individual sensors depends on the delay of the loop in which the multiplexer channels are switched. This can be adjusted with the help of this function. The value always refers to a single sensor and must be multiplied by 64 when considering a full refresh on the display.

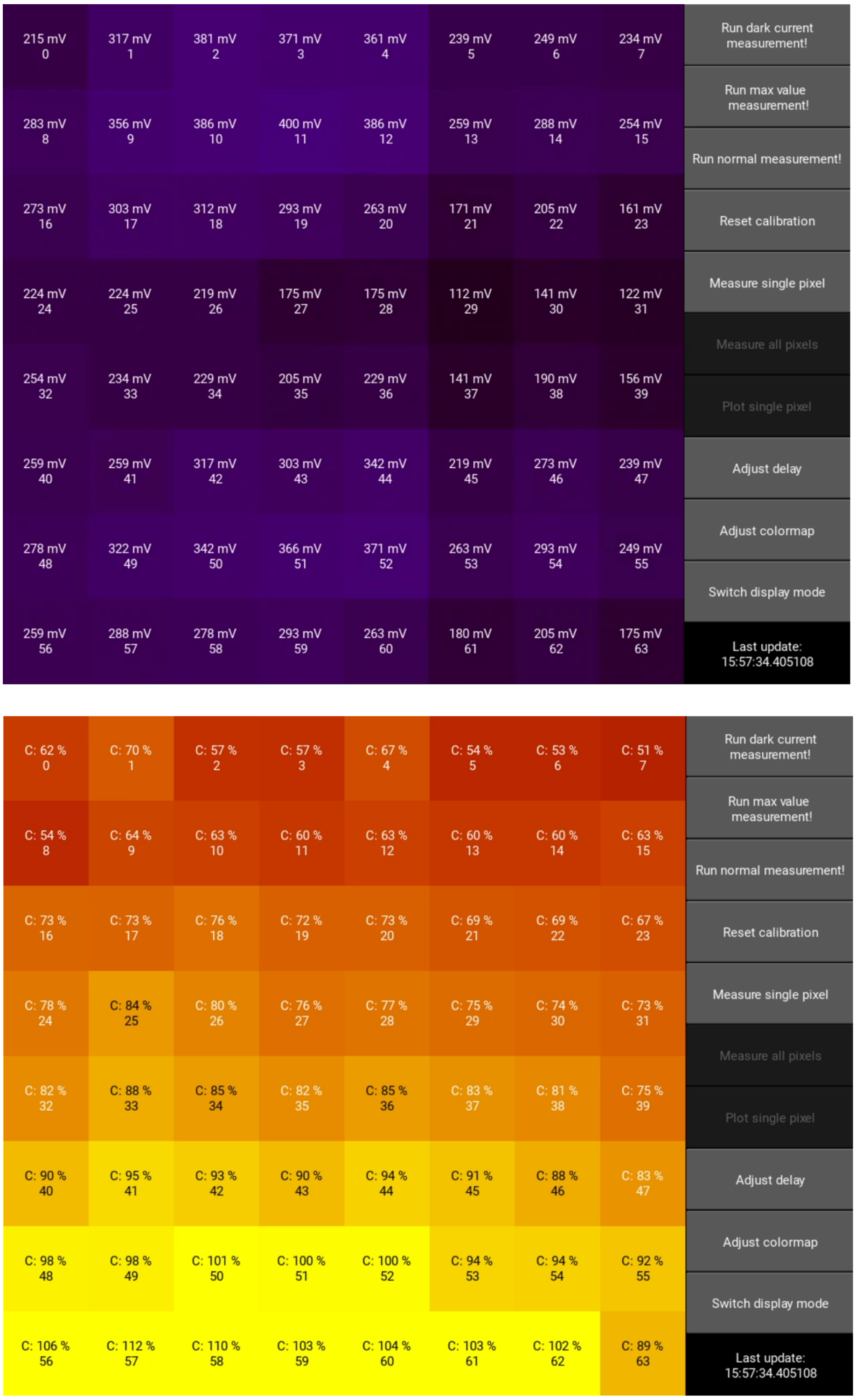

215 mV 0	317 mV 1	381 mV 2	371 mV 3	361 mV 4	239 mV 5	249 mV 6	234 mV 7
283 mV 8	356 mV 9	386 mV 10	400 mV 11	386 mV 12	259 mV 13	288 mV 14	254 mV 15
273 mV 16	303 mV 17	312 mV 18	293 mV 19	263 mV 20	171 mV 21	205 mV 22	161 mV 23
224 mV 24	224 mV 25	219 mV 26	175 mV 27	175 mV 28	112 mV 29	141 mV 30	122 mV 31
254 mV 32	234 mV 33	229 mV 34	205 mV 35	229 mV 36	141 mV 37	190 mV 38	156 mV 39
259 mV 40	259 mV 41	317 mV 42	303 mV 43	342 mV 44	219 mV 45	273 mV 46	239 mV 47
278 mV 48	322 mV 49	342 mV 50	366 mV 51	371 mV 52	263 mV 53	293 mV 54	249 mV 55
259 mV 56	288 mV 57	278 mV 58	293 mV 59	263 mV 60	180 mV 61	205 mV 62	175 mV 63

Last update:
15:57:34.405108

C: 62 % 0	C: 70 % 1	C: 57 % 2	C: 57 % 3	C: 67 % 4	C: 54 % 5	C: 53 % 6	C: 51 % 7
C: 54 % 8	C: 64 % 9	C: 63 % 10	C: 60 % 11	C: 63 % 12	C: 60 % 13	C: 60 % 14	C: 63 % 15
C: 73 % 16	C: 73 % 17	C: 76 % 18	C: 72 % 19	C: 73 % 20	C: 69 % 21	C: 69 % 22	C: 67 % 23
C: 78 % 24	C: 84 % 25	C: 80 % 26	C: 76 % 27	C: 77 % 28	C: 75 % 29	C: 74 % 30	C: 73 % 31
C: 82 % 32	C: 88 % 33	C: 85 % 34	C: 82 % 35	C: 85 % 36	C: 83 % 37	C: 81 % 38	C: 75 % 39
C: 90 % 40	C: 95 % 41	C: 93 % 42	C: 90 % 43	C: 94 % 44	C: 91 % 45	C: 88 % 46	C: 83 % 47
C: 98 % 48	C: 98 % 49	C: 101 % 50	C: 100 % 51	C: 100 % 52	C: 94 % 53	C: 94 % 54	C: 92 % 55
C: 106 % 56	C: 112 % 57	C: 110 % 58	C: 103 % 59	C: 104 % 60	C: 103 % 61	C: 102 % 62	C: 89 % 63

Last update:
15:57:34.405108

Figure 26: Screenshot of the GUI to read out the sensors. The upper case shows a measurement of the obtained raw voltage data, the lower side a calibrated measurement.

5 Results

In this section, the experimental results are shown, which include the optimization of the sensor structure, the characterization of a selected design and several applications cases.

5.1 Diode design approaches

First, this section presents the results obtained by varying the sensor structure. The electrode material, the thickness of the semiconductor layer, the dimensions of the sensor and the general design are altered. The diode current under variation of the applied voltage and also the response time under irradiation of UV light as well as without is shown and discussed.

5.1.1 Gold-Gold layer structure

The first design approach consists of two symmetrical gold electrodes connected by an overlying layer of IGZO. Throughout this work, the following nomenclature is used for the dimensions of a sensor:

Number of sensor sections | *Width of active sensor area* x *Height of active sensor area*
e.g. 1 | 100 μm x 10 μm

The picture below shows how the dimensions of a sensor are defined in case of the example of a sensor structure with dimensions 1 | 100 μm x 10 μm as also shown in full view in Figure 28 (b).

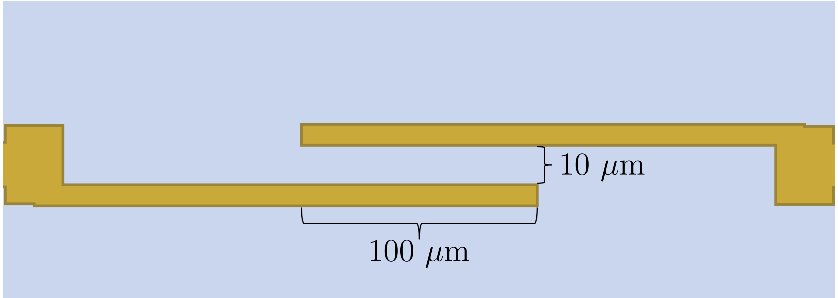

Figure 27: Sketch of 1 | 100 μm x 10 μm zoomed in the active sensor area scope.

The gold layer actually consists of a thin chromium adhesive layer, on which the gold is then deposited. The thickness ratio of chromium/gold is 20 nm/70 nm on every substrate. For the first design, a batch of eight substrates was prepared, two with 40 nm IGZO, four substrates with 70 nm IGZO and two substrates with 120 nm IGZO. Because the RF sputtering machine target does not spatially deposit the same all over, the thickness was measured, so the best position for further batches can be used. Table 1 shows the targeted thickness values and the measured values, which were averaged over four measurements. The thickness measurement was performed using a Dektak 1600 profilometer.

As the measurement results show, the measured values correspond to the expected ones, especially for the Cr/Au layer they are almost perfect. Since the 70 nm substrates were produced first and substrates three and four correspond best to the desired thickness, the others were spatially placed in the machine as they were.

Table 1: Measured layer thicknesses of the layers for the first batch consisting of 8 substrates.

Substrate	Measured Cr/Au thickness	Measured IGZO thickness
40 nm No. 1	90.3 nm	42.7 nm
40 nm No. 2	89.2 nm	37.0 nm
70 nm No. 1	86.9 nm	59.3 nm
70 nm No. 2	90.9 nm	61.6 nm
70 nm No. 3	89.4 nm	71.7 nm
70 nm No. 4	90.1 nm	72.8 nm
120 nm No. 1	85.8 nm	113.4 nm
120 nm No. 2	89.1 nm	114.7 nm

The first important parameter for classifying the characteristics of the manufactured diodes is the U/I characteristic. The electrodes are connected on both sides and a voltage U_{D} is applied. The measured current I_{D} is measured for variable voltages. The whole process is done with and without UV light. The Keithley system can perform this measurement fully automatic, quickly and precisely, so that several diodes of the same type can be measured. Since the UV diode is manually attached to the measurement set-up, the same distance to the diode is not always guaranteed resulting in a different UV power and therefore there may be minor deviations in the characteristics between them. However, the key factors are differences in production, as sputter thickness and etch rate can vary slightly. Figure 28 shows the diode design on the left side and the U/I curve for voltages $-20\,\mathrm{V}$ to $20\,\mathrm{V}$ on the right side for the substrate 7 or 8 corresponding to 120 nm of IGZO. Because of the measured linear behavior according to Ohm's law, the current flow also increases at higher voltages, the y-axis is shown logarithmically and additionally the absolute value is given. Actually, no linear ohmic contact is expected because of the Schottky contact, but it seems to be strongly pronounced with these diodes. The blue curve shows the curve when the UV diode is switched off, the orange curve when it is switched on. The diode has its peak in the wavelength at about 385 nm, which corresponds to 3.22 eV and should therefore already have enough energy for an excitation. This is confirmed by looking at the difference between the blue and orange curves. The irradiated UV light can transport electrons in the semiconductor from the valence to the conduction band and strongly increase the conductivity. The different sensor types are compared in Table 2. The value of the current at 10 V is always evaluated. The first three sensor types in the table refer to sensors with a single section. It can be seen that although the current with and without the active sensor width increases with increasing active sensor width, the ratio of both sizes does not improve. Similar behavior is also seen for diodes with ten individual sections. The ratio of the currents is always within one to two orders of magnitude difference. Figure 29 shows the values in the table again graphically. For both sensor types, an increase in the active sensor width leads only slowly, if at all, to an increase in the current; a significant increase in current only occurs at values greater than 100 μm width. However, since the current also increases without light incidence, the ratio of the currents does not improve. For this reason, it can be stated that smaller sensor dimensions also achieve equally good or better results and are better suited due to the possibility of fitting more sensors on a substrate because of the small size.

Table 2: Measured currents I_D with and without UV exposure and the corresponding ratio for different sensor types. All values are obtained by an applied voltage U_D of 10 V.

Sensortype	I_D without UV light	I_D with UV light	$I_{\mathrm{D(Light)}}/I_{\mathrm{D(no\ Light)}}$
1 | 10 μm x 10 μm	$6.6 \cdot 10^{-11}$ A	$1.3 \cdot 10^{-8}$ A	196.9
1 | 100 μm x 10 μm	$5.2 \cdot 10^{-10}$ A	$1.7 \cdot 10^{-8}$ A	32.7
1 | 500 μm x 10 μm	$2.0 \cdot 10^{-9}$ A	$5.9 \cdot 10^{-8}$ A	29.5
10 | 10 μm x 10 μm	$1.4 \cdot 10^{-8}$ A	$2.3 \cdot 10^{-7}$ A	16.4
10 | 20 μm x 10 μm	$4.8 \cdot 10^{-9}$ A	$1.0 \cdot 10^{-7}$ A	20.8
10 | 50 μm x 10 μm	$7.6 \cdot 10^{-9}$ A	$2.2 \cdot 10^{-7}$ A	28.9
10 | 100 μm x 10 μm	$6.1 \cdot 10^{-9}$ A	$2.1 \cdot 10^{-7}$ A	34.4
10 | 500 μm x 10 μm	$6.3 \cdot 10^{-8}$ A	$8.7 \cdot 10^{-7}$ A	138.1
10 | 1000 μm x 10 μm	$1.2 \cdot 10^{-7}$ A	$2.0 \cdot 10^{-6}$ A	16.6

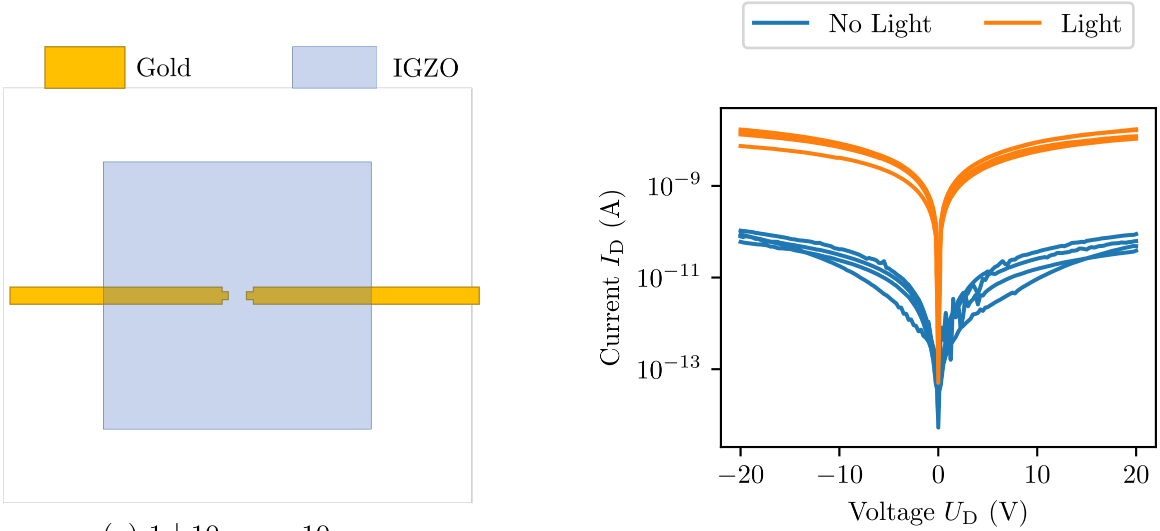

(a) 1 | 10 μm x 10 μm

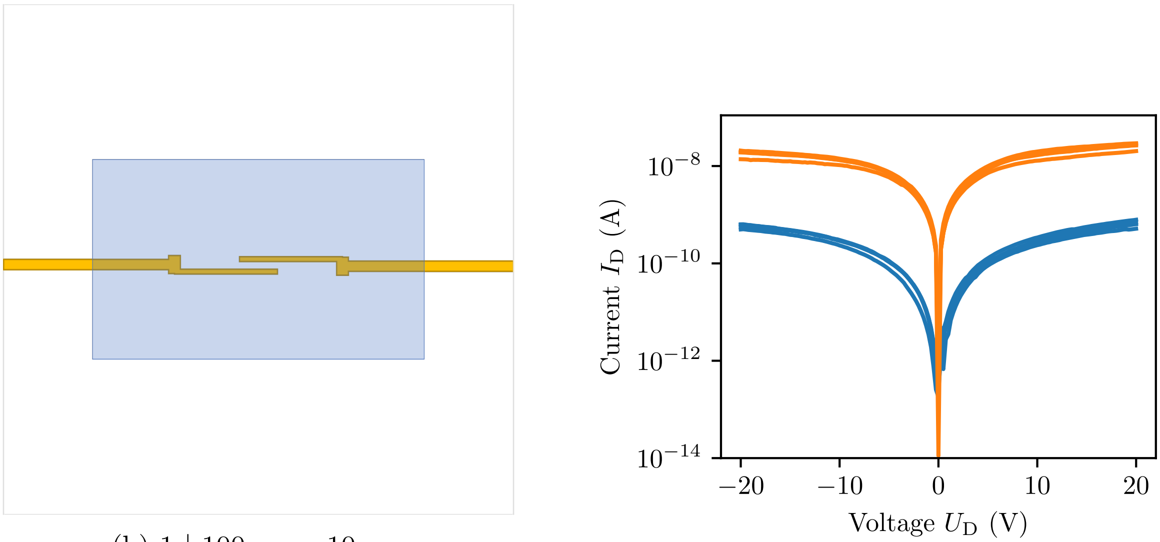

(b) 1 | 100 μm x 10 μm

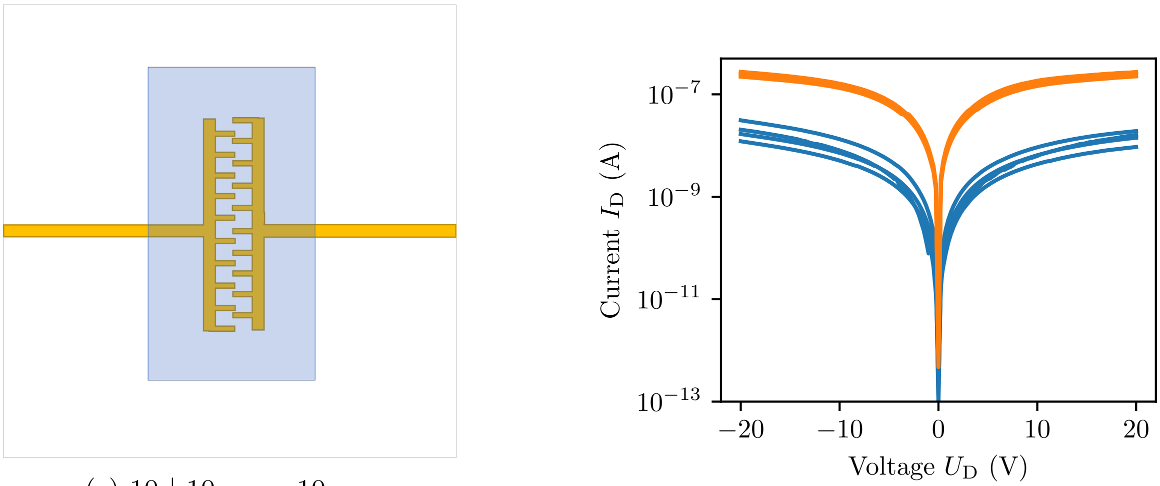

(c) 10 | 10 μm x 10 μm

Figure 28: Sketches of different diode structure designs with gold electrodes on both sides on the left and the associated U/I-curve with and without UV exposure in logarithmic mapping. Substrate 7 or 8 with 120 nm IGZO were used for this plot.

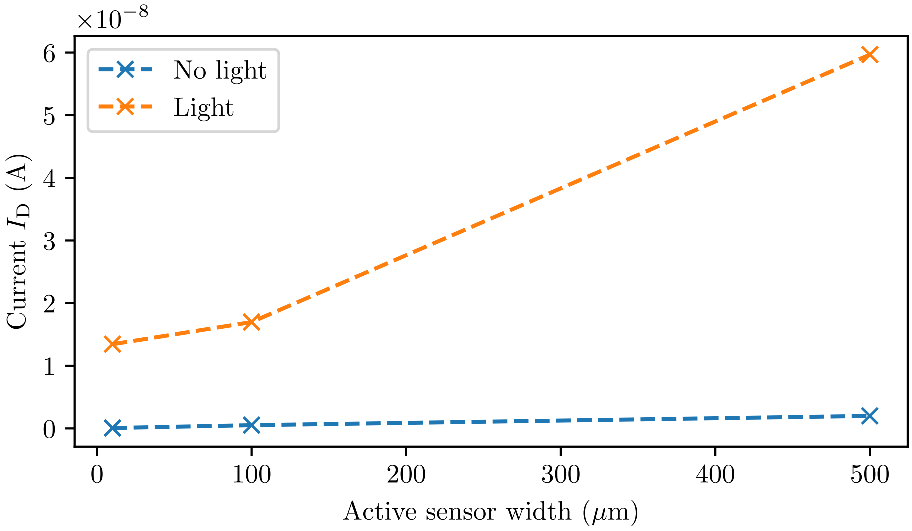

(a) Sensor type 1 | x µm x 10 µm

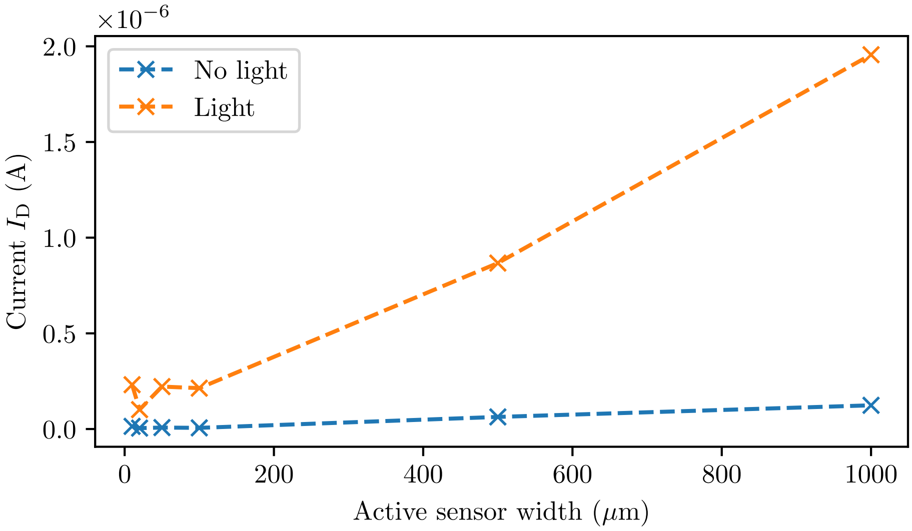

(b) Sensor type 10 | x µm x 10 µm

Figure 29: Dependence of the current I_D on the active sensor width for two different structures (a) & (b). The x denotes the variation in the active sensor width. The dashed lines are a guide for the eye.

Response time

One of the most important properties for photosensors is their response time. According to [31], oxygen vacancies affect the response time, so the thickness of the IGZO layer was varied to change the number of vacancies. Therefore, three different layer thicknesses were chosen, 40 nm, 70 nm and 120 nm. The 1 | 10 µm x 10 µm structure was chosen for the measurement, as these showed the most stable values in U/I measurements.
To measure the reponse time, the sensor was kept under a constant voltage, in this

case at 5 V. On an oscilloscope the measured voltage was recorded time resolved, which was done by connecting the circuit as explained in chapter **Methods**. The UV LED at 385 nm is blocked and released manually. The measurement curves for the different film thicknesses are shown in Figure 30. The measured voltage was converted back to a current using Ohm's law. $R = 1\,\mathrm{M\Omega}$ was used as the feedback resistor. In Figure 30, the areas where the rise time in green and the fall time in red, were evaluated are also drawn as dotted lines. For the layer thickness of 40 nm and 70 nm the rise time is evaluated from the measured maximum value, since a steady increase of the current was still recorded. Therefore, the rise times are greater than the evaluated ones. It can be clearly seen that with increasing IGZO layer thickness, both the rise and fall times are significantly reduced. The largest jump occurs from 70 nm to 120 nm layer thickness. Table 3 shows the values obtained. While the values for rise and fall time are still in the seconds range, as shown by workgroups in [28, 31], the times at 120 nm thickness are already in the millisecond range. The working group [1] was also able to achieve response times in the millisecond range. In a later section, even better times than shown here could be achieved. The slow increase and also decrease after the irradiation was switched off are striking. According to [31] one possible explanation is a change in the oxygen vacancies, which are ionized by the irradiated light and thus get an increased energy in the band scheme and move closer to the conduction band. This increases the conductivity because then both the electrons and the localized holes of the oxygen vacancies contribute to the conduction. Also peroxide ions O_2^{2-} can be created out of single oxide ions O^{2-}, offering even more conducation electrons, which states then relaxate back slowly [36]. The effect is also called persistent photo conductivity (PPC). The conductivity increases after a longer period of irradiation and continues to exist even after the UV light is switched off and only decreases slowly. Due to the increased amount of charge carriers in thicker layers, it can be assumed that the recombination of holes and electrons is more likely and therefore the fall time can be significantly improved. Unfortunately, it cannot be explained exactly why this also improves the preceding rise time considerably.

It can be stated that a higher IGZO layer thickness leads to considerable improvements in both the rise and fall time. Due to the long and also more expensive production of even thicker layers, this was not done in this work. However, it is not excluded that even better results can be achieved by doing so.

Table 3: Reponse time dependent on the IGZO layer thickness. The measured sensor was of the type 1 | 10 μm x 10 μm.

IGZO thickness	Rise time τ_{rise}	Fall time τ_{fall}
40 nm	> 2.914 s	> 3.755 s
70 nm	> 2.217 s	0.394 s
120 nm	0.082 s	0.088 s

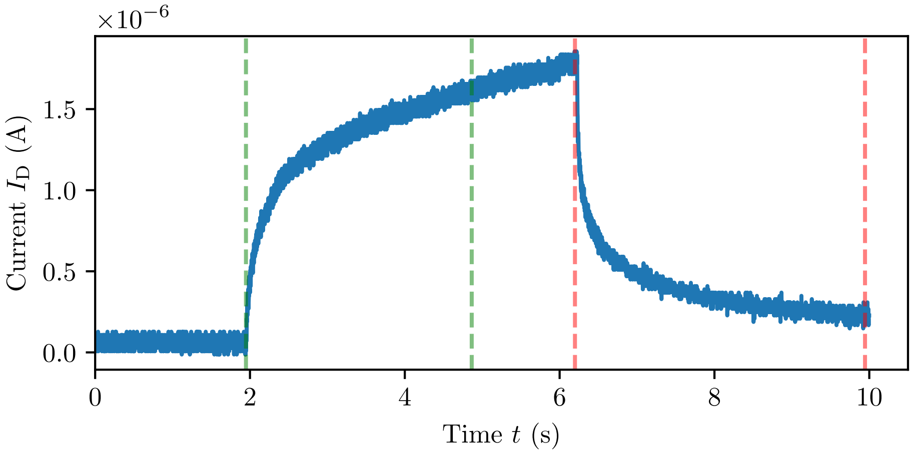

(a) Response time measurement of an 40 nm IGZO diode

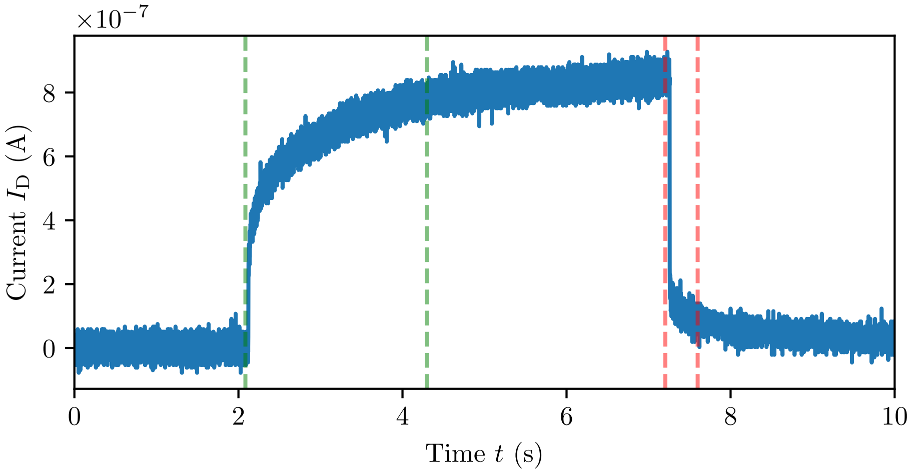

(b) Response time measurement of an 70 nm IGZO diode

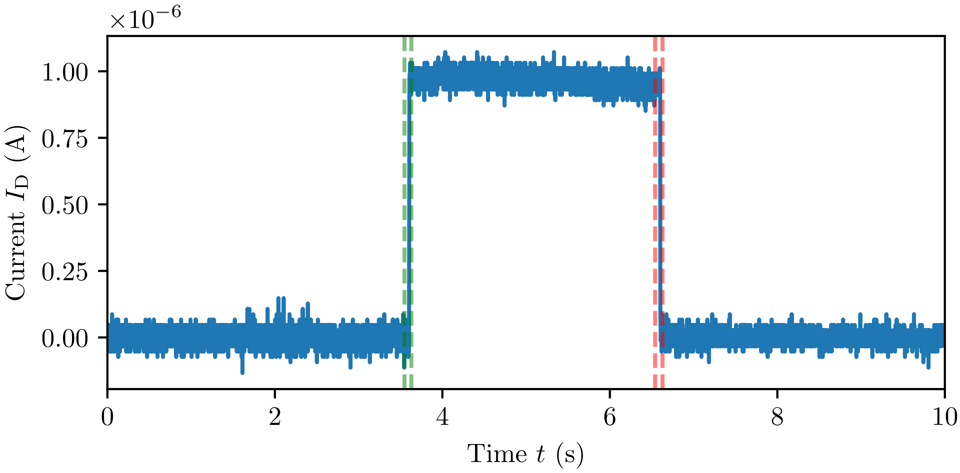

(c) Response time measurement of an 120 nm IGZO diode

Figure 30: Behavior of the current I_D under direct UV irradiation (385 nm). The green dotted lines indicates the domain of the 10%-90% increase, the red ones show the 90%-10% decrease.

5.1.2 Electrode material variation

This section deals with sensors in which one of the two electrodes is replaced by another conductive material instead of gold. Due to the easy handling and availability in the clean room, aluminum and ITO were used. ITO, indium tin oxide is a semiconductor, but it still has a high conductivity. For this series of measurements, the 10 | 10 μm x 10 μm structure was chosen because it was the most homogeneous during fabrication. The layer thickness for gold is again a mixture of Cr/Au as in the previous substrates, which is 90 nm in total, the aluminum has a thickness of 75 nm and the ITO 50 nm. Figure 31 shows the design layout and associated U/I characteristics. Since gold, aluminum and ITO (Au: $\sim 5.3\,\text{eV}$ [37], Al: $\sim 4.2\,\text{eV}$ [37], ITO: $\sim 4.6\,\text{eV}$ [38]) have different workings and therefore a different Schottky barrier, which changes the U/I behavior, this should be reflected in the U/I measurement. Looking at the Au-Al sensor, the characteristic looks symmetrical, whereas for the Au-ITO sensor a slight asymmetry is visible. However, since the work function for aluminum is lower than that of ITO, the effect should be more visible there. The more direct explanation lies in the different conductivity or resistivity. This is significantly lower for aluminum with $\rho \sim 10^{-6}\,\Omega\text{cm}$ [39] than for ITO with $\rho \sim 10^{-4}\,\Omega\text{cm}$ [40]. Looking at the ratio of the currents in Table 4, we get promising results especially for the Au-Al sensor, which are even higher than those for pure Au-Au sensors, but the crucial point, the response time, will be discussed in the next section.

Table 4: Measured currents I_D with and without UV exposure and the corresponding ratio for different sensor electrode materials. All values are obtained by an applied voltage U_D of 10 V and of the sensor type 10 | 10 μm x 10 μm.

Electrodes	I_D without UV light	I_D with UV light	$I_{\text{D(Light)}}/I_{\text{D(no Light)}}$
Au-Alu	$9.9 \cdot 10^{-11}\,\text{A}$	$1.2 \cdot 10^{-7}\,\text{A}$	1212.1
Au-ITO	$5.3 \cdot 10^{-10}\,\text{A}$	$4.5 \cdot 10^{-8}\,\text{A}$	84.9

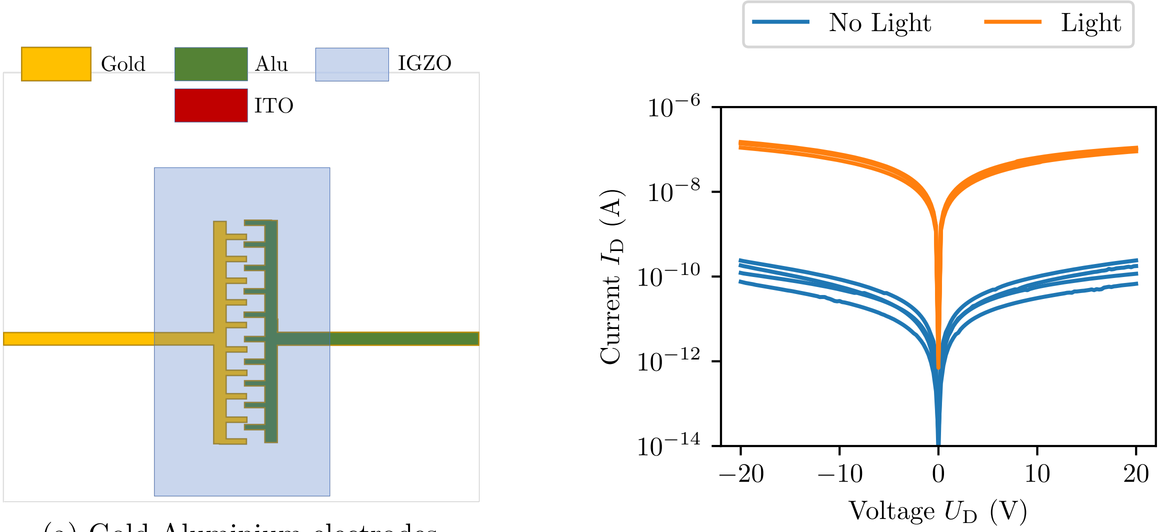

(a) Gold-Aluminium electrodes

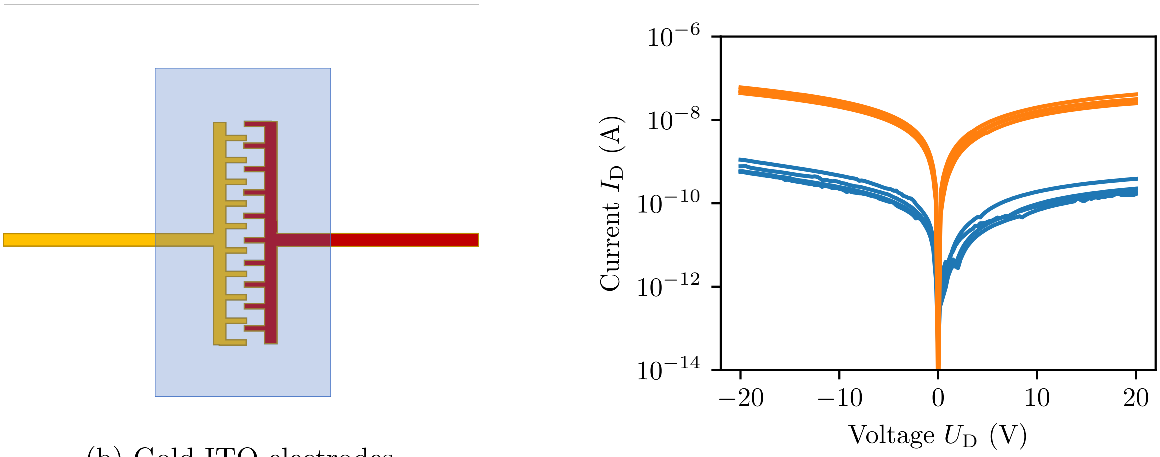

(b) Gold-ITO electrodes

Figure 31: Sketch of diodes with different electrode materials on the left side and the associated U/I-curve with and without UV exposure in logarithmic mapping. The substrates have an IGZO thickness of 120 nm.

Response time

Table 5: Response times for different electrode materials. The measured sensor was from the type 10 | 10 μm x 10 μm.

Electrode materials	Riset ime τ_{rise}	Fall time τ_{fall}
Au-Alu	0.088 s	0.104 s
Au-ITO	0.027 s	0.130 s

Since it was discussed in the previous section which film thickness provided the best results, these substrates are also coated with 120 nm IGZO. Figure 32 shows the response of the diodes for the different electrode combinations Au-Al in (a) and Au-ITO in (b). Both rise and fall times for both variants are low and in a similar range to the Au-Au variant, as can be seen in Table 5. The Au-ITO variant performs a little better, since the rise time is lower and a stable plateau is reached almost immediately after the rise. Nevertheless, especially in comparison to Au-Au sensors, no serious advantage or disadvantage can be seen and because of the additional process step due to the different material, it is not a useful alternative. For some unknown reason, the 50 Hz noise is very clearly visible in this measurement. Possibly the low pass filter was was not properly integrated into the circuit for this measurement.

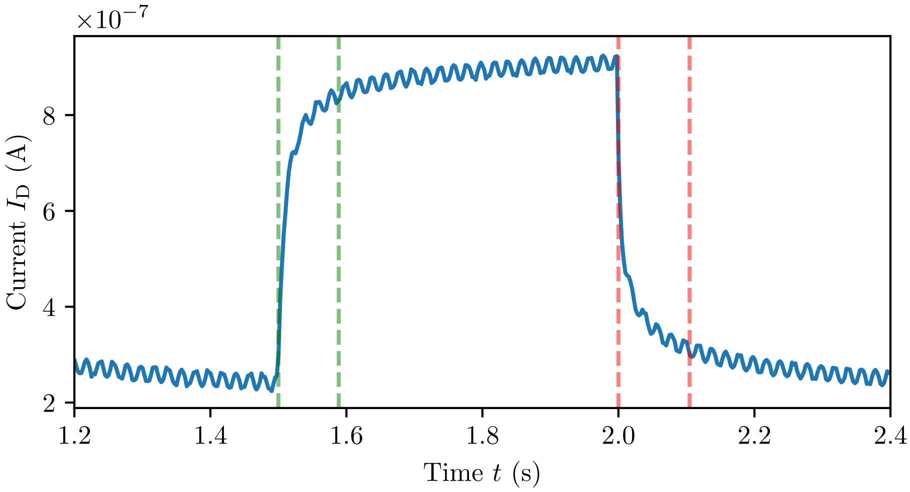

(a) Response time measurement for sensors with Gold-Aluminum electrodes

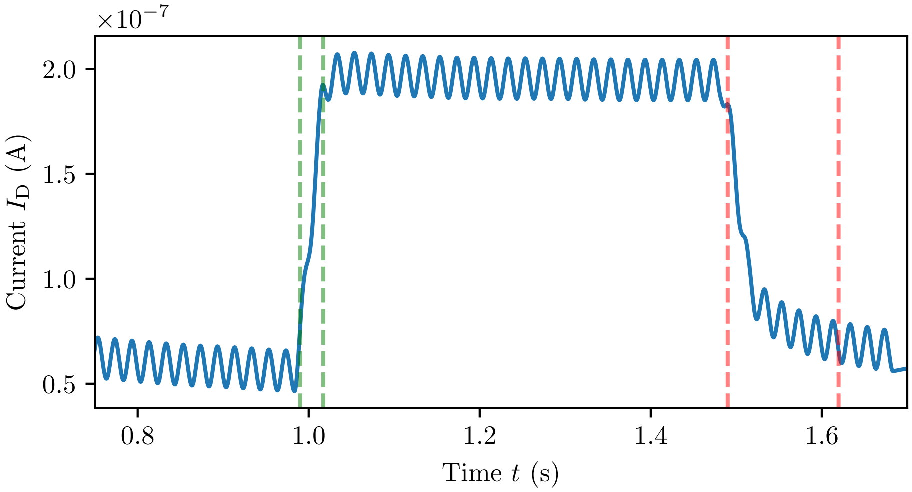

(b) Response time measurement for sensors with Gold-ITO electrodes

Figure 32: Behavior of the current I_D under direct UV irradiation (385 nm) for different electrode material combinations. The green dotted lines indicates the domain of the 10%-90% increase, the red ones shows the 90%-10% decrease.

5.1.3 Vertical structure approach

As a final design attempt, a vertical structure was tried instead of a flat horizontal one. Figure 33 shows the design layout. First, one of the two electrodes is structured. On top of this comes the IGZO layer, which connects the second layer above it to the second electrode via a dielectric with the help of a VIA mask. To prevent the entire surface of the upper layer from coming into contact with the IGZO, a second layer of dielectric between the IGZO and the upper layer creates a smaller connection channel to the electrode. The sensors measured here thus have an active sensor area of $15\,\mu$m x $20\,\mu$m, which is shown as the left green area in the diagram.The parameters for the thicknesses are kept unchanged. If one looks at the U/I graphs to the right, there is a strong difference to the previous structures. The range of negative voltage U_D is almost constant up to 0 V when irradiated with light and also without. This does not show a typical behavior according to Ohm's law, there seems to be an immediate saturation for negative voltages. In principle, this would not be a problem for detection, since as shown in Table 6 the ratios of the currents at $-10\,\mathrm{V}$ are very good. Furthermore, such structures can be used in this range as an almost perfect current source as a load in circuits. Here the current can be varied by material choice and dimension of the active area. The range for positive voltages, on the other hand, is not applicable, since they show little difference to each other when irradiated, as opposed to no UV light.

Table 6: Measured currents I_D with and without UV exposure and the corresponding ratio for different sensor electrode materials. All values are obtained by an applied voltage U_D of $-10\,\mathrm{V}$.

Electrodes	I_D without UV light	I_D with UV light	$I_{\mathrm{D(Light)}}/I_{\mathrm{D(no\ Light)}}$
Au-Au	$6.9 \cdot 10^{-9}\,\mathrm{A}$	$9.3 \cdot 10^{-7}\,\mathrm{A}$	134.8
Au-ITO	$5.1 \cdot 10^{-10}\,\mathrm{A}$	$7.2 \cdot 10^{-8}\,\mathrm{A}$	141.2

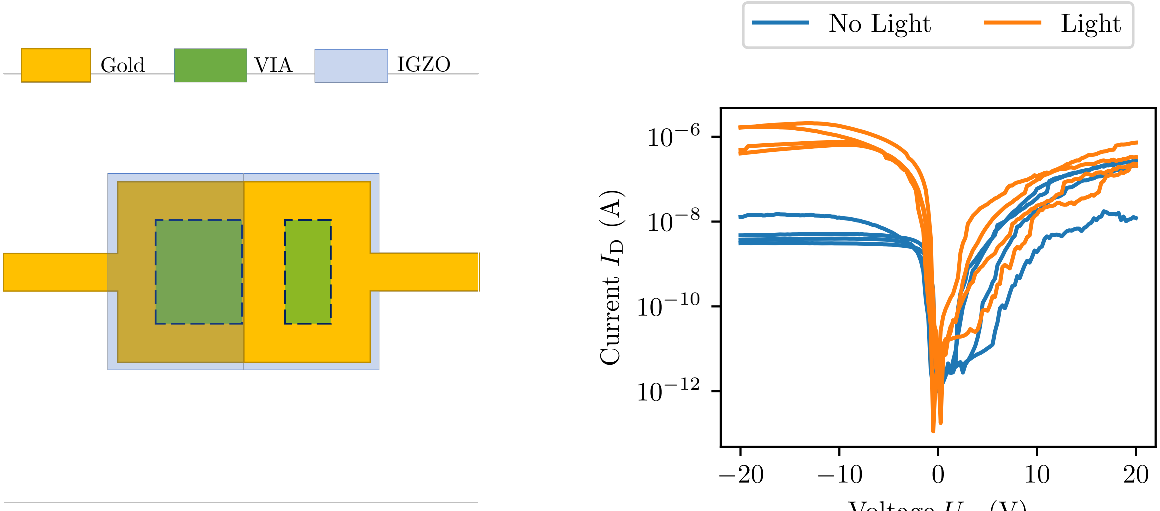

(a) Gold-Gold electrodes

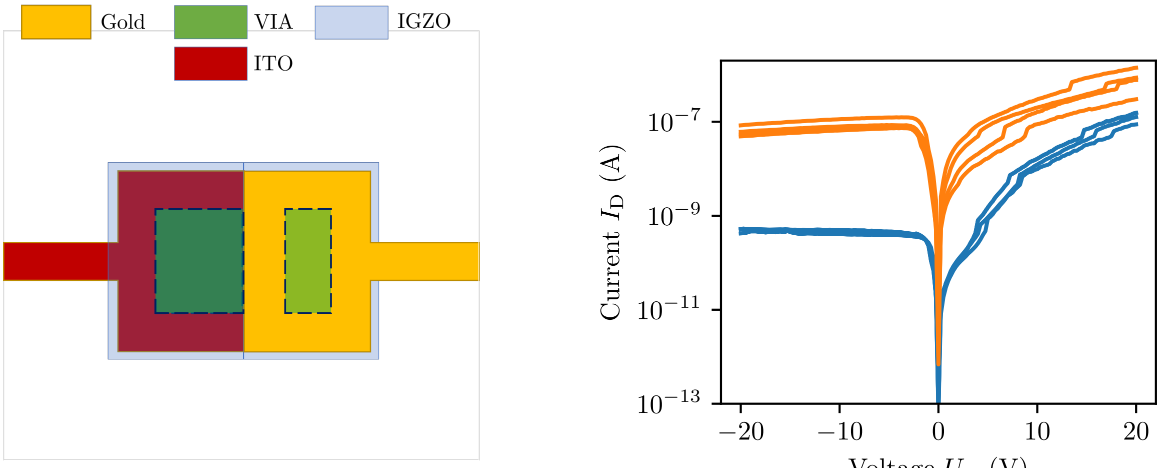

(b) Gold-ITO electrodes

Figure 33: Sketch of diodes with different electrode materials and vertical structure on the left site and the associated U/I-curve with and without UV exposure in logarithmic mapping. The substrates have an IGZO thickness of 120 nm.

Response time

Since it was possible to achieve good detection at least in the negative voltage range, it is anticipated that the response properties will also be improved. However, if we consider Figure 34, the graphs look similar to those of a layer thickness of 40 nm from the first design. Also, the rise and fall times shown in Table 7 are in the second range, making it useless as a sensor for fast detection. Unfortunately, the reason for such high times cannot be conclusively explained. One explanation is that during fabrication the dielectric is etched with the help of plasma and is also deposited in a plasma. Since the IGZO is not applied as the last layer, it is possible that the plasma has made irreparable changes in the IGZO structure.

Table 7: Response times for different electrode materials and vertical structure.

Electrode materials	Rise time τ_{rise}	Fall time τ_{fall}
Au-Au	1.645 s	4.377 s
Au-ITO	0.921 s	1.932 s

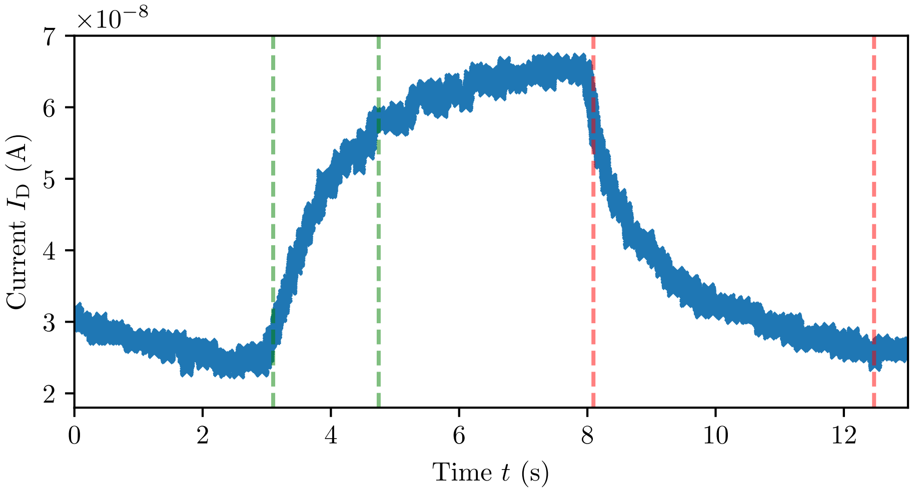

(a) Response time measurement for sensors with Gold-Gold electrodes

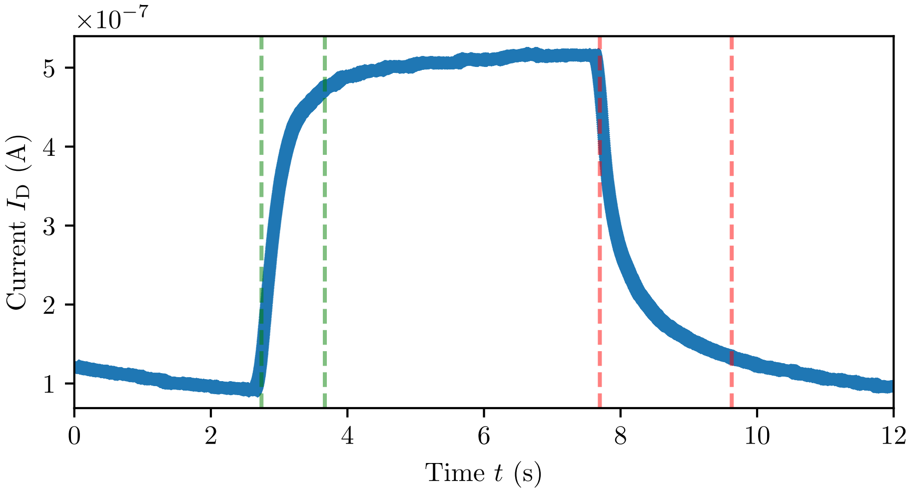

(b) Response time measurement for sensors with Gold-ITO electrodes

Figure 34: Behavior of the current I_D under direct UV irradiation (385 nm) for different electrode material combinations and vertical structure. The green dotted lines indicates the domain of the 10%-90% increase, the red ones show the 90%-10% decrease.

5.2 Characteristics of the diode of choice

After testing various parameters for optimizing in the previous sections, a final design was chosen for all following measurements. Figure 35 shows the final design, which is a diode with dimension 1 | 10 μm x 100 μm and dual gold electrodes consisting of 70 nm Cr/Au and 120 nm IGZO. Key factors in choosing this design were the dependence of the dimension of the active sensor area, which was established in the first section. The result is a good compromise between measured current and area at the present dimension, especially with regard to the application in the sensor array. In addition, this design was simple to manufacture and less error-prone in terms of mask alignment.

Figure 35 on the right shows the U/I curve, which appears to be largely symmetrical, small deviations can arise from inhomogeneities during deposition of the layers or etch inhomogeneities. The values at 10 V for the current without light $I_{\text{D(no Light)}} = 2.2 \cdot 10^{-10}$ A and $I_{\text{D(Light)}} = 4.7 \cdot 10^{-7}$ A give a ratio of 2134 which is the best result so far. The ratio depends on the light intensity, which will also be discussed in this chapter. However, since the same LED was operated with the same power, the results are comparable.

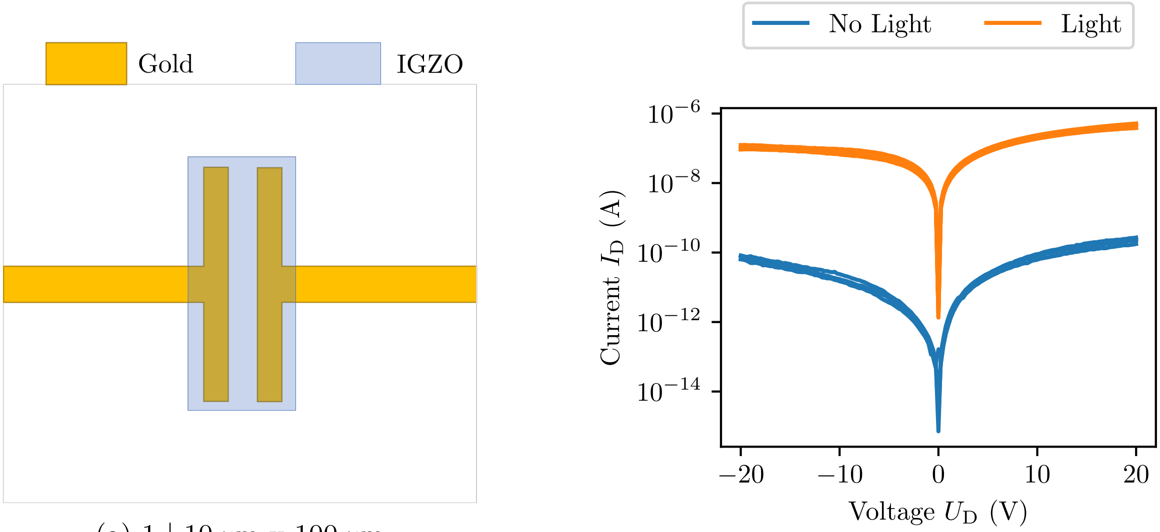

(a) 1 | 10 μm x 100 μm

Figure 35: Sketch of the final diode design on the left site and the associated U/I-curve with and without UV exposure (385 nm) in logarithmic mapping. The substrate have an IGZO thickness of 120 nm.

Response time

For the response time measurement, measurements were also made for the first time at a wavelength in the deeper UV. The 226 nm results from a frequency quadrupled titanium sapphire laser with a fundamental wavelength of 904 nm. Figure 36 shows for (a) the measurement with the 385 nm diode and (b) with the 226 nm laser light.

The obtained values for rise- and falltime are given in Table 8. Comparing the rise time at 385 nm with 226 nm, it improves by an order of magnitude from about 44 ms to 4 ms. Possibly the 226 nm laser light excites states higher up in the band gap, which have faster conduction, resulting in a faster response. In contrast to the improved risetime at lower wavelength, the falltime degrades. The reason for this can also only be guessed at and, according to [31], explained by the oxygen vacancies. At lower wavelengths, more ionized defects can be generated, which then contribute to the current conduction due to the energy increase near the conduction band and relax only slowly.

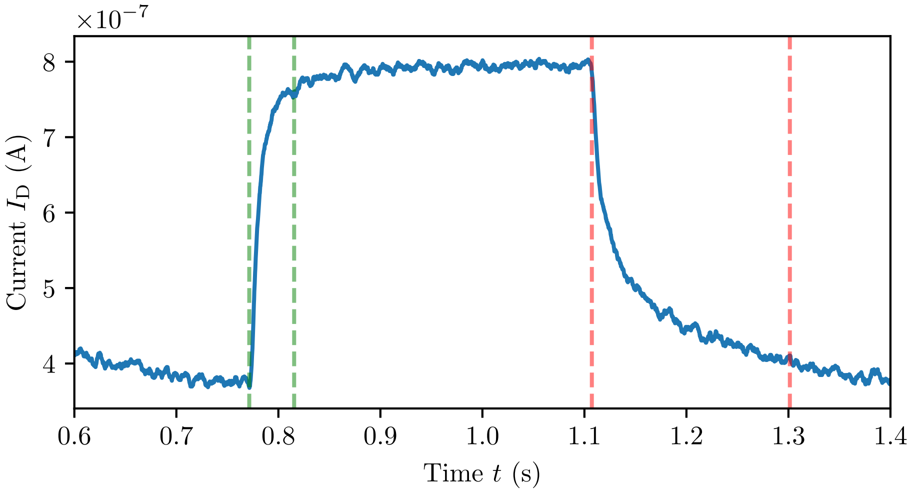

(a) Response time measurement for $\lambda_{\text{Light}} = 385\,\text{nm}$

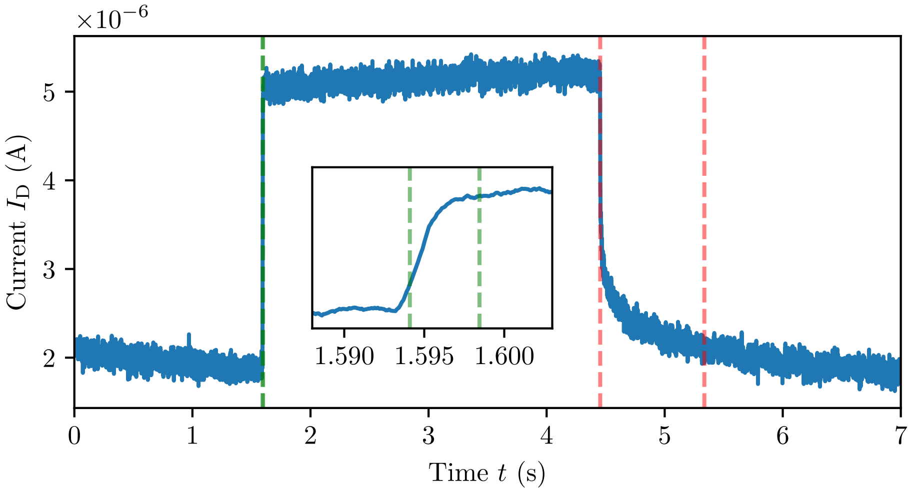

(b) Response time measurement for $\lambda_{\text{Light}} = 226\,\text{nm}$

Figure 36: Behavior of the current I_D under direct UV irradiation for different UV wavelenghts. The green dotted lines indicates the domain of the 10%-90% increase, the red ones shows the 90%-10% decrease.

Table 8: Response times for different light wavelenghts.

Wavelenght λ	Rise time τ_{rise}	Fall time τ_{fall}
385 nm	0.044 s	0.194 s
226 nm	0.0043 s	0.882 s

Since rise- and falltime are at least one order of magnitude apart and fast detection is desired, a compromise must be made to ensure sufficient differentiation of measured current without and with light. Therefore the 385 nm diode was connected to a frequency generator to send a constant frequency of light pulses. Figure 37 shows the maximum and minimum of the measured current at different pulse frequencies of the diode. Since the risetime is significantly lower than the falltime, the maximum current remains almost constant over a range of $0 - 500$ Hz pulse frequency, whereas the minimum current first increases steeply in the range $0 - 100$ Hz, but then also approaches a more or less constant value. For a useful measurement difference between the two current values, the threshold value is about 50 Hz, which corresponds to a period of 0.025 s. Thus, the current has not yet dropped to the value of 10% of the maximum value, but still a passable measurement difference is visible. This value is especially relevant with regard to the readout in the array later.

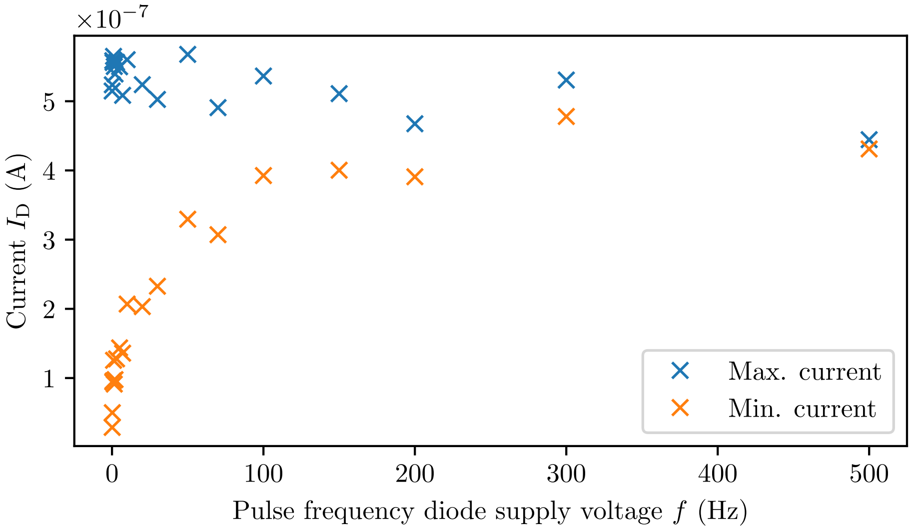

Figure 37: Measured maximum and minimum values of the current I_D at variable pulse frequency $f$of the 385 nm diode.

Responsivity

The responsivity is another characteristic quantity with which photodiodes can be compared with each other. It is defined by the conversion efficiency from optical input into electrical output. As in formula 3.45 the responsivity R is in this case:

$$R = \frac{I_{\text{D(light)}} - I_{\text{D(no Light)}}}{P} \tag{5.1}$$

Here, the measured power of the light source cannot simply be used, but only the power P that shines on the photosensitive area of the diode may be included. The beam with radius r is assumed to be Gaussian, which corresponds to a total power of the beam

$$P_0 = I_0 \underbrace{\frac{\pi r^2}{2}}_{A_{\text{gauss}}} . \tag{5.2}$$

To obtain the power for a single sensor irradiated with a gaussian beam, the total power of the beam must be factored with the ratio of the photo area A_{photo} and the area of the gaussian profile A_{gauss} . The photosensitive area A_{photo} is assumed here to be the rectangular IGZO area with dimensions 110 μm x 40 μm. This results in the following for the responsivity

$$R = \frac{I_{\text{D(light)}} - I_{\text{D(no Light)}}}{P_0 \cdot \frac{A_{\text{photo}}}{A_{\text{gauss}}}}. \tag{5.3}$$

The beam radius was measured using a photodiode and a program that fits a Gaussian profile to the beam profile. The beam of the LED diode could be focused to a beam with radius $r = 2\,\text{mm}$ with the help of two lenses and the UV laser beam to $r = 0.9\,\text{mm}$. Figure 38 (a) shows the responsivity as a function of the applied diode voltage U_{D} for different powers of the 385 nm UV diode, (b) shows the responsivity for measurements with the 226 nm UV laser.

Looking at the graph, the responsivity grows with increased diode voltage, which makes perfect sense according to the Formula 5.3, as with increased diode voltage the current grows as well. The curve is linear for all tested powers in the range of $0 - 14\,\text{V}$, then slopes down slightly and is linear again with a slightly lower gradient. The measurement points for a power of 5 μW show that the produced IGZO photodiodes are especially effective for even lower powers. Responsivities of more than 120 A/W can be achieved at diode voltages of approx. $< 25\,\text{V}$. Table 9 shows a comparison of different works on IGZO photosensors and their achieved responsivities. None of the works shown can achieve responsivities in the wavelength range of approx. 385 nm, which are shown in this work.

Looking in Figure 38 at the responsivity of measurements of the diode at 226 nm, values of up to ~ 2000 A/W are achieved at 20 V applied voltage. In this case, the response seems to be linear throughout. Since the power of the laser is reduced by waveplates and only a value of minimum 15 μW was achieved, it can be assumed that even higher values of the responsivity can be achieved for lower powers. Since only one work with measurements in the deep UV range could be found, there is little comparative material. That work achieved a value of ~ 0.1 A/W [1], which in this work is five orders of magnitude larger.

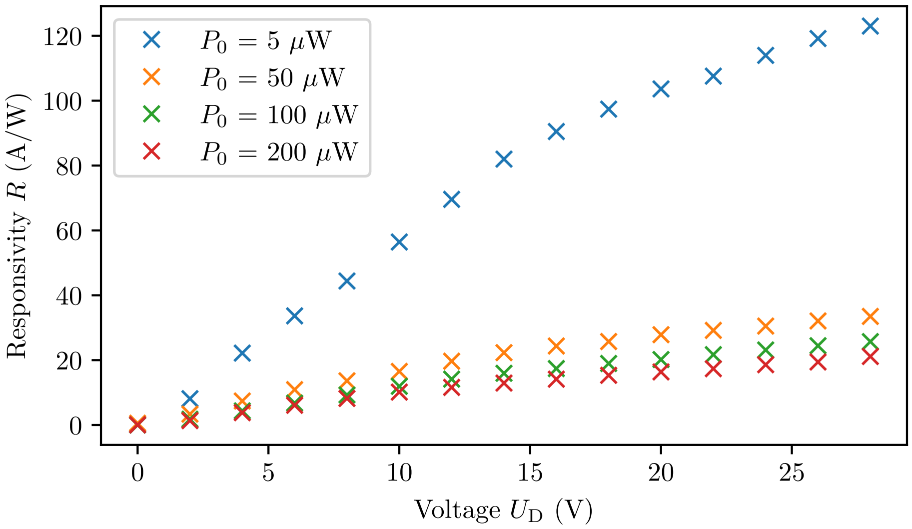

(a) Responsivity measured at four different UV LED powers P_0 at $\lambda = 385\,\text{nm}$ with a beam radius of $r = 2\,\text{mm}$

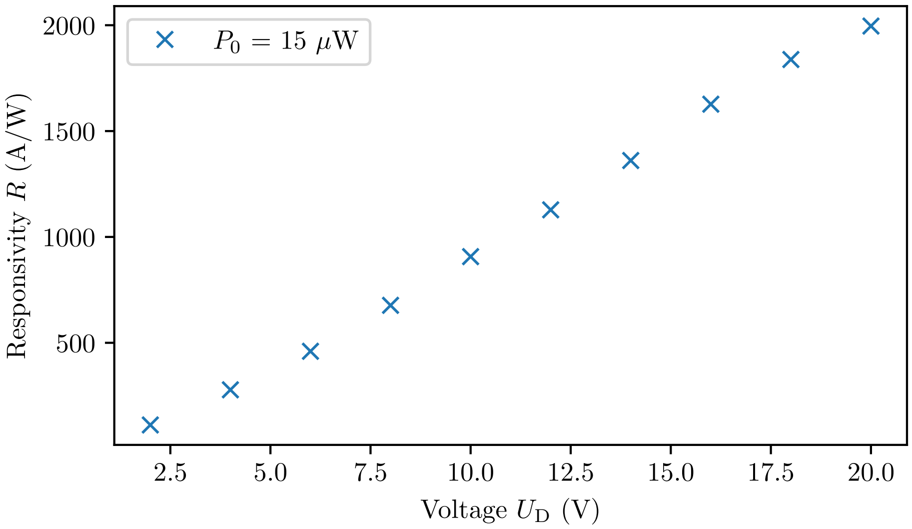

(b) Responsivity measured at a UV laser power P_0 at $\lambda = 226\,\text{nm}$ with a beam radius of $r = 0.9\,\text{mm}$

Figure 38: Responsivity R as a function of the applied diode voltage U_D for 385 nm (a) and 226 nm light (b).

Table 9: Comparison of archieved responsivities from different groups. The results for 385 nm from this work are taken from measurements of $P_0 = 5\,\mu$W.

Responsivity R	Diode voltage U_D	Wavelengthbehavior λ	Ref.
123.1 A/W	28 V	385 nm	This work
22.2 A/W	4 V	385 nm	This work
1996.0 A/W	20 V	226 nm	This work
$<$ 0.05 A/W	5 V	370 nm	[23]
3.32 A/W	2 V	365 nm	[28]
0.08 A/W	-	320 nm	[24]
$\sim$ 1.0 A/W	14 V	325 nm	[1]
$\sim$ 0.1 A/W	14 V	225 nm	[1]
0.016 A/W	3 V	370 nm	[41]

In order to investigate the behavior as a function of power, the responsivity was measured for both wavelengths under a fixed diode voltage. Figure 39 shows the responsivity at 385 nm for $U_\mathrm{D} = 5$ V (a) and for 226 nm and $U_\mathrm{D} = 15$ V. The $R \sim P^{-1}$ dependence is clearly visible for both curves. This should ideally peak at a power P_limit, at which the diode still gives a recognizable signal and thus the responsivity is highest. However, this could not be shown in this measurement, since such low powers could not be achieved. If the values of R are compared with the right choice of parameters, shown in Figure 38, they agree very well. Single outliers as in (a) for $P > 125\,\mu$W can be explained by the fact that possibly the excited IGZO states are not yet fully relaxed and therefore delivered a slightly higher current, as it was already discussed in the section of the response time. Since the same diode was used for these measurements, it cannot be excluded that permanent changes in the IGZO structure occur after some time of irradiation.

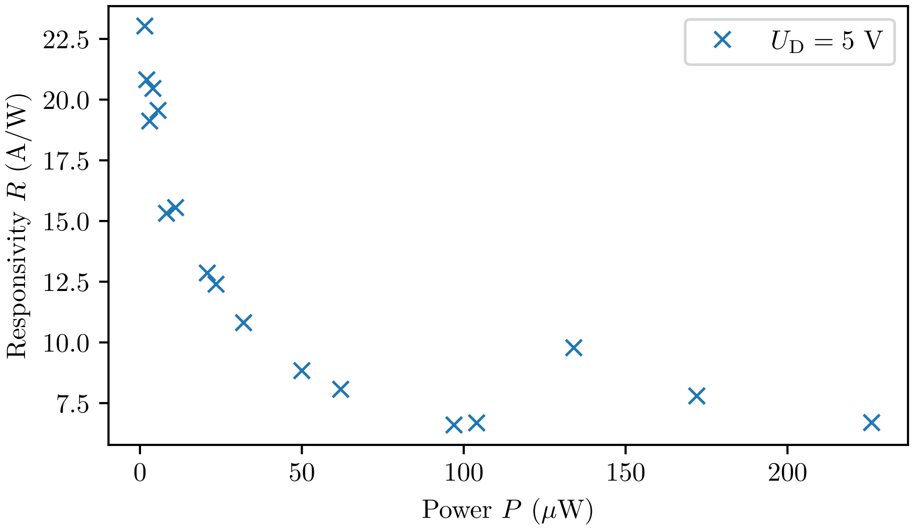

(a) Responsivity measured at $\lambda = 385\,\mathrm{nm}$ and $r = 2\,\mathrm{mm}$

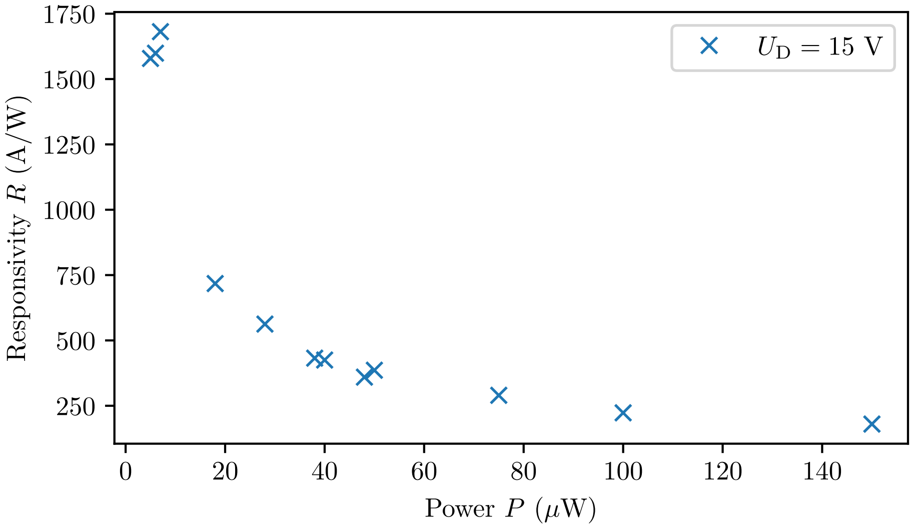

(b) Responsivity measured at $\lambda = 226\,\mathrm{nm}$ and $r = 0.9\,\mathrm{mm}$

Figure 39: Responsivity R as a function of the UV power P for 385 nm (a) and 226 nm light (b).

All previous measurements were made at room temperature $T \approx 22^\circ$ C, so it is interesting to see if higher temperatures result in a difference. For this purpose, the glas substrate with the diodes was fixed on a metallic surface with thermocouple and heated up to almost 70° C. The responsivity was evaluated at different temperatures, which can be seen in Figure 40. The diode voltage is fixed at 5V and the measurement was taken for two different powers of the 385 nm LED. A temperature measurement at 226 nm was not possible, because such a metal plate including thermocouple is difficult to integrate into the laser setup. Looking at the two curves, a drop in responsivity with increasing temperature can be observed. This can be explained by the fact that the mobility μ, which is proportional to the collision times of the charge carriers τ, dominates the scattering at ionized impurities with $\mu \sim T^{3/2}$ for lower temperatures, but is dominated by phonon scattering with $\mu \sim T^{-3/2}$ at higher temperatures [22]. Since apparently the scattering by phonons is less pronounced at higher power, the responsivity also drops significantly lower there. Overall, however, the effect of phonon scattering seems to dominate, since no increase can be seen.

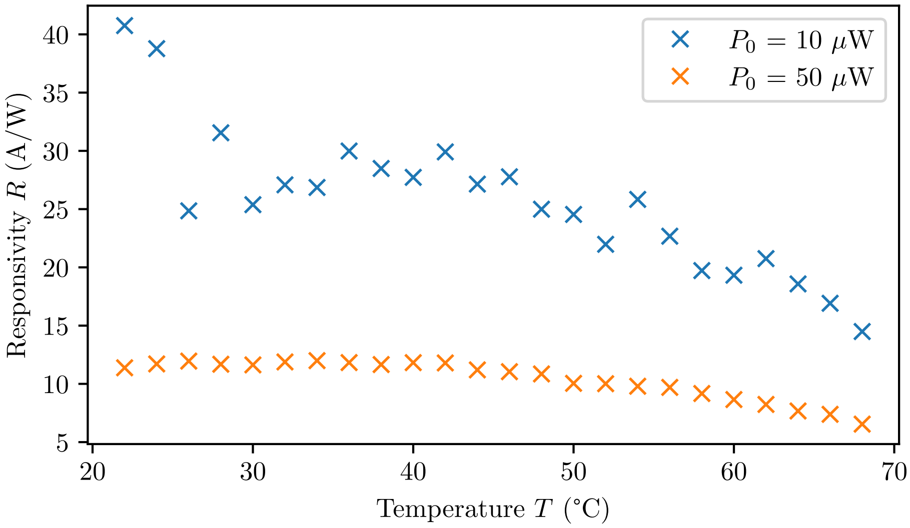

Figure 40: Responsivity R as a function of substrate temperature T under fixed diode voltage $U_D = 5\,$V at different powers P_0 of the 385 nm LED.

Signal-to-noise ratio & Noise-equivalent power

In this section, the noise characteristics are examined in more detail and compared with a conventional avalanche photodiode [3]. First the signal-to-noise ratio was calculated as follows

$$SNR = \frac{I_{\mathrm{D(Light)}} - I_{\mathrm{D(no\ Light)}}}{I_{\mathrm{D(Noise)}}} \tag{5.4}$$

from which the noise equivalent power can be drawn. For this purpose the measurements must not be performed with a low pass filter with a 25 Hz cutoff frequency as before, but limited to 1 Hz. Therefore the resistor R_2 was increased to 2.65 MΩ. Also the applied diode volatge was fixed to $U_{\mathrm{D}} = 5\,\mathrm{V}$. Figure 41 shows the SNR as a function of power on a single sensor for the IGZO sensor under the influence of 385 nm light (a), for a commercial avalanche photodiode (Thorlabs APD130A2) (b) and for the IGZO sensor under 226 nm laser light (c). The black dashed line indicates the noise-equivalent power level. This is the power at which the SNR is exactly one. For the IGZO diode, the SNR looks very steeply increasing for small powers, which then ends in a sort of plateau or minimal increase. The commercial photodiode shows a very linear behavior. Two measurements were made, one with the photodiode connected to the oscilloscope directly after the 1 Hz lowpass and one with a 50 Ω termination. The SNR slightly worsened with the last one. Table 10 shows a comparison of the obtained values for the NEP, which are obtained from extrapolation of the data at $SNR = 1$. The values at 385 nm for the SNR are three orders of magnitude better for the IGZO sensor than for the commercial photodiode both with and without a 50 Ω termination. Even at a lower wavelength of 226 nm, it performs better than the APD at 385 nm. Although the datasheet by Thorlabs [3] gives a value of $\sim 0.2\,\mathrm{pW}/\sqrt{\mathrm{Hz}}$, this cannot be compared with the value presented here, since a lock-in detection technique is used and the NEP is related to the value of the highest responsivity $R_{\max} = 25\,\mathrm{A/W}$ of the APD for $\lambda_{\mathrm{R_{max}}} = 600\,\mathrm{nm}$ [3]. As the responsivity decreases with decreasing wavelength [3], it can be assumed that the APD also has a larger NEP for smaller wavelenghts. These commercial photodiodes may be better for the use of a wide range of wavelenghts, but the presented IGZO diode beats it in the UV range.

Table 10: Noise-equivalent powers for at different wavelenghts for the IGZO sensor and a commercial APD.

Wavelenght λ	Sensor type	NEP
385 nm	IGZO	$0.26\,\mathrm{nW}/\sqrt{\mathrm{Hz}}$
385 nm	APD	$0.36\,\mu\mathrm{W}/\sqrt{\mathrm{Hz}}$
385 nm	APD with 50 Ω	$0.50\,\mu\mathrm{W}/\sqrt{\mathrm{Hz}}$
226 nm	IGZO	$0.14\,\mu\mathrm{W}/\sqrt{\mathrm{Hz}}$

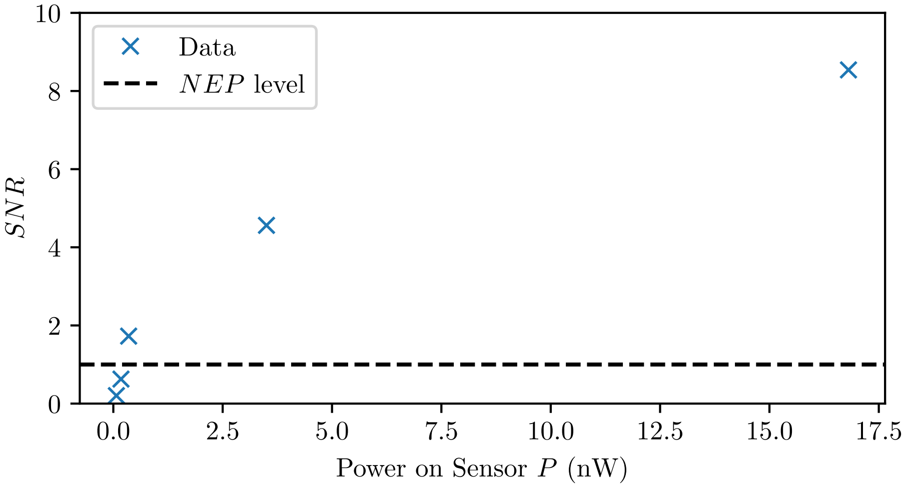

(a) IGZO sensor at $\lambda = 385\,\text{nm}$

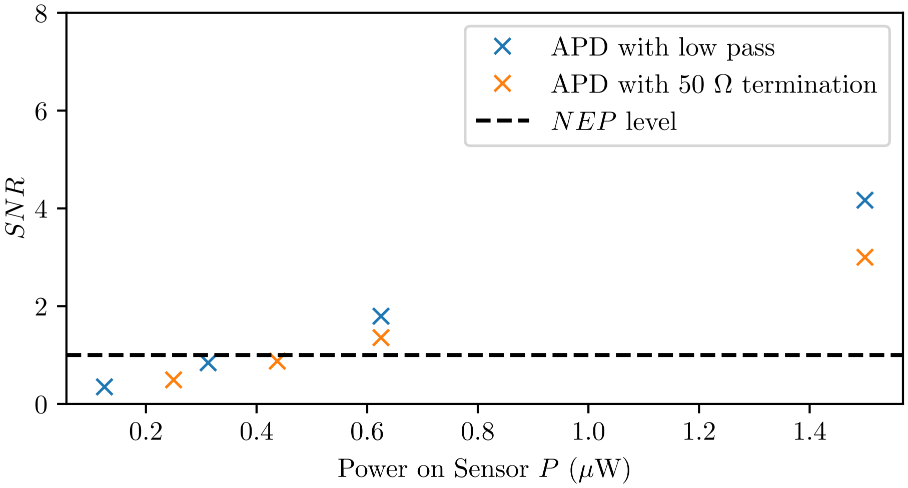

(b) APD sensor at $\lambda = 385\,\text{nm}$

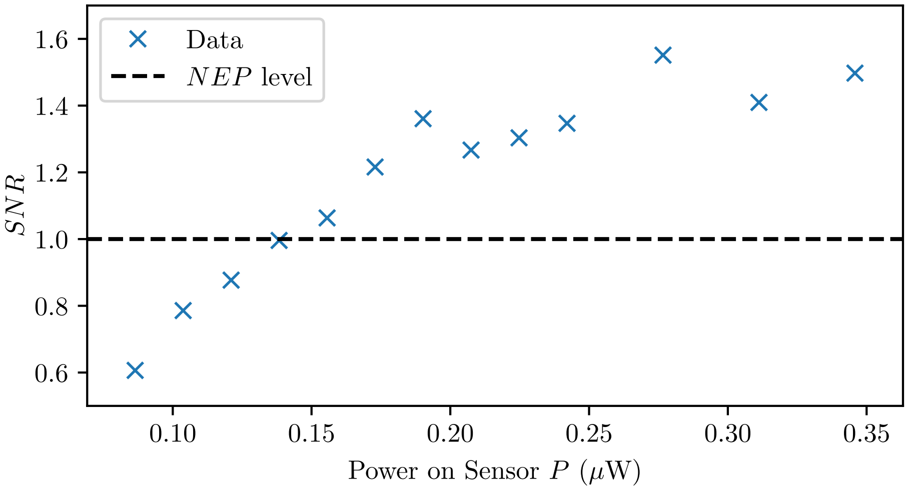

(c) IGZO sensor at $\lambda = 226\,\text{nm}$

Figure 41: Signal-to-noise ratio as a function of power to a single sensor P for different wavelengths λ and sensor types. The black dashed line indicates the level at which the NEP is reached.

At last the peak-to-peak behavior of the signal without light incidence is examined at 226 nm. For this purpose, the maximum and minimum values of the current are searched for in a small range and then averaged over many ranges. The difference between these two values gives the peak-to-peak value, which is shown in Figure 42. In (a) the power P was varied from $10 - 150\,\mu$W. It can be seen that the noise initially increases, but then forms a plateau at around $40\,\mu$W. Thus, the noise is independent of the power. The situation is different when the voltage U_D is varied in (b). Here the current was measured from $1 - 20$ V and it seems that the noise increases more or less linearly and does not become consistent. This also makes sense, since the increased voltage also transports more charge carriers, which are already present without excitation by light. Overall, however, it can be said that the noise only increases by a maximum of about 20% over a wide range, both with an increase in power or voltage.

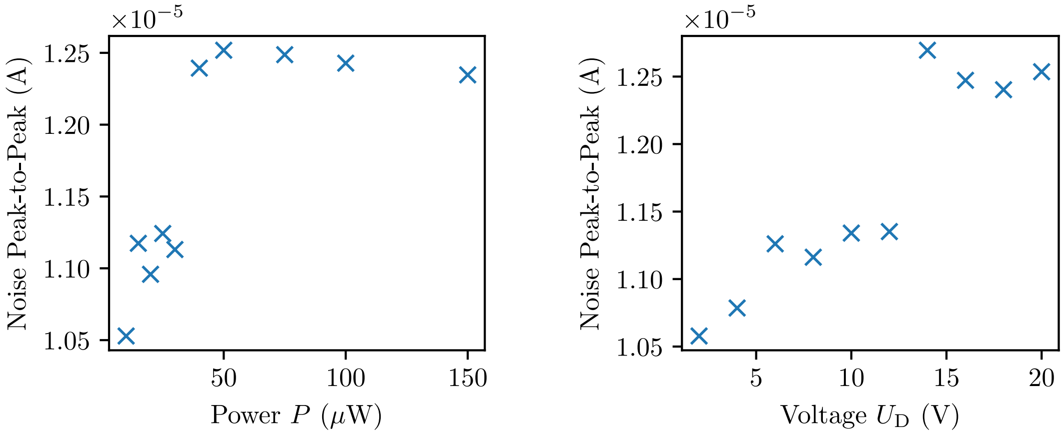

(a) $U_\mathrm{D} = 15$ V (b) $P = 80\,\mu$W

Figure 42: Peak-to-peak value of the noise generated without light irradiation at 226 nm as a function of the power P and the diode voltage U_D.

5.3 Fluorescence measurements

After the characterization of the diode, measurements integrated into the actual measurement setup can now be performed. For this purpose, a project is used which has also provided the 226 nm laser by a frequency-quadrupled Ti:Sa laser. Detailed work about the project and their measurements can be found in [13, 12, 42]. The goal of this measurement is to collect the fluorescence light from excited nitric oxide. The theory can be found in the theory chapter "Nitric oxide". For this purpose a glass cell is built, which has the glas substrate with the photosensors glued vacuum-tight on the bottom or top side. Figure 43 shows the installed glass cell in the experiment. The invisible UV ligth path is indicated by the purple beam.

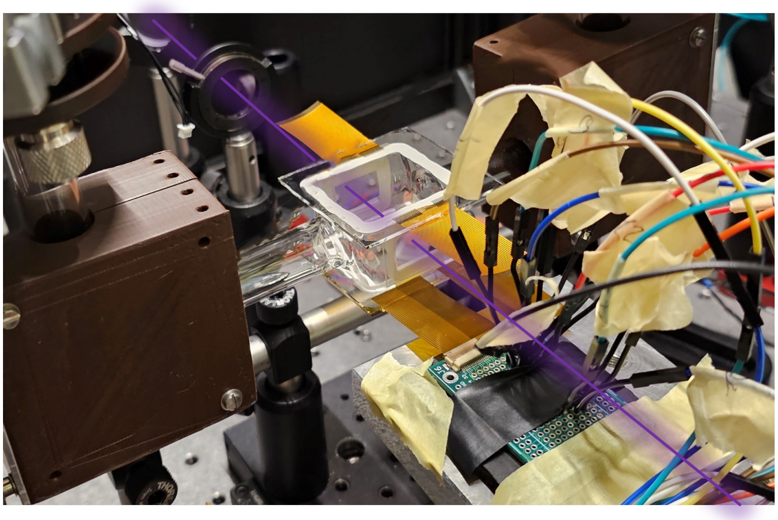

Figure 43: Glas cell with IGZO sensors on the top and bottom side installed in the experiment. The otherwise invisible UV laser beam is drawn in purple on top to indicate the laser path.

In the setup itself, pressure in the cell ($\widehat{=}$ flow rate of the nitrogen monoxide), laser power as well as the wavelength can be tuned. In order to record a fluorescence transition, the power of the laser, the pressure in the cell and the diode voltage are kept constant and the wavelength of the 904 nm titanium sapphire laser is tuned, resulting in a tuned UV wavelength. Such a measurement takes about 600-1200 seconds to avoid that the readout electronics distort the result by tuning too fast. In addition, an avalanche photodiode (Thorlabs APD130A2) is installed after the cell, which also records the absorption signal as a reference. Figure 44 shows such a recorded measurement signal, above the fluorescence signal of the IGZO diode, below the absorption signal of the APD. Since the signal is recorded in time on an oscilloscope, but a frequency axis is desired, a reference cavity is needed to calibrate the frequency axis. Using the cavity peaks of the 904 nm laser, the time axis can be converted as follows. First the cavity peaks are converted into a frequency:
The free spectral range (FSR) of the 904 nm cavity is known and is 897.4 MHz for 226 nm since the FSR is wavelenght dependent. Since the measurement was made with the quadrupled 226 nm, the factor 4 must be added. The frequency peaks are

then fitted with a third order polynomial and the fit function is taken as the new frequency axis.

In order to be able to theoretically describe the behavior of the two measurements, the phenomena described in the chapter "broadening mechanisms" must first be estimated.
The Doppler broadening at room temperature $T = 293\,\mathrm{K}$ and a wavelength of 226 nm is given by equation 3.29 to $\Delta f_{\mathrm{Doppler}} = 2.96\,\mathrm{GHz}$.
An estimate of the pressure broadening according to equation 3.33 gives [12] at nitric oxide and 2 mbar pressure and room temperature with $\Delta f_{\mathrm{Press}} = 5.22\,\mathrm{MHz}$.
The transit time broadening is given by 3.32 at room temperature for nitric oxide and a measured diameter of $d = 1.8\,\mathrm{mm}$ as follows $\Delta f_{\mathrm{Transit}} = 189.3\,\mathrm{kHz}$.
Power broadening is estimated as the final broadening mechanism. According to equation 3.35, the saturation intensity $I_{\mathrm{sat}} = 18.1\,\mathrm{mW/mm^2}$ is obtained with the value for $\Gamma \approx 160\,\mathrm{MHz}$ taken from [12] at a wavelength of 226 nm. With a diameter of $d = 1.8\,\mathrm{mm}$ this would require a saturation intensity of $P_{\mathrm{sat}} = 46\,\mathrm{mW}$, which cannot be achieved in this experiment. Thus the power broadening from equation 3.34 if the intensity is assumed to be equal to the saturation intensity can be calculated to $\Delta f_{\mathrm{Power}} = 160\,\mathrm{kHz}$. However, a paper [43] published as part of the project shows that the transition is being saturated and that the assumed values provide only very rough estimates.

As can be seen, the Doppler broadening dominates by far. Therefore, all other effects are neglected in the evaluation. Since the Doppler broadening has a Gaussian shape, an asymptotic Gaussian is assumed for the fluorescence, since the slope and decay are different due to the readout electronics and the slow fall time. This asymetric Gaussian is also called "Crystal ball function" and is defined according to [44] as follows:

$$g(x, \alpha, n, x_0, \sigma) = N \cdot \begin{cases} e^{-\frac{(x-x_0)^2}{2\sigma^2}}, & \text{for } \frac{x-x_0}{\sigma} > -\alpha \\ A \cdot (B - \frac{x-x_0}{\sigma})^{-n}, & \text{for } \frac{x-x_0}{\sigma} \leq -\alpha \end{cases} \tag{5.5}$$

where

$$\begin{aligned} A &= \left(\frac{n}{|\alpha|}\right)^2 \cdot \left(e^{-\frac{|\alpha|^2}{2}}\right), \\ B &= \frac{n}{|\alpha|} - |\alpha|, \\ N &= \frac{1}{\sigma(C + D)}, \\ C &= \frac{n}{|\alpha|} \cdot \frac{1}{n-1} \cdot e^{-\frac{|\alpha|^2}{2}}, \\ D &= \sqrt{\frac{\pi}{2}} \left(1 + \mathrm{erf}\left(\frac{|\alpha|}{\sqrt{2}}\right)\right). \end{aligned}$$

The function is a mixture of Gauss and a polynomial part, the function “erf” is the error function, α some sort of polynomial weight, n the polynomial degree, x_0 the center of the function and σ the width of the Gaussian part. To fit the baseline of the measurement, a third order polynomial is assumed. Thus, the total fit function of the fluorescence measurement is given by

$$F(x, u, \alpha, n, x_0, \sigma, a_1, a_2, a_3, a_4) = u \cdot g(x, \alpha, n, x_0, \sigma) + \text{Polynomial}(x, a_1, a_2, a_3, a_4). \tag{5.6}$$

The factor u is used to circumvent the normalization.

For the absorption the Lambert Beer law from equation 3.2 must be included. The function thus results in

$$b(x, c, d, \alpha, n, x_0, \sigma) = c \cdot e^{-d \cdot g(x,\alpha,n,x_0,\sigma)} \tag{5.7}$$

and with a additional third order polynomial baseline part to the full fit function

$$\begin{aligned} B(x, c, d, \alpha, n, x_0, \sigma, a_1, a_2, a_3, a_4) &= b(x, c, d, \alpha, n, x_0, \sigma) \\ &+ \text{Polynomial}(x, a_1, a_2, a_3, a_4) \end{aligned} \tag{5.8}$$

Due to the difficulties with the fit, the value for $n = 11$ was fixed by manual trial and error.

Figure 44 shows the measurement and fit for the parameters $P = 170\,\mu\text{W}$, $p = 0.1\,\text{mbar}$, $U_\text{D} = 2\,\text{V}$, a tuning range of the 904 nm laser of 10 GHz at a duration of 1000 s. The baseline fit through the polynomial was subtracted from each of the measurement results and the fit.

The Full-Width-Half-Maximum (FWHM) values result from $2\sqrt{2\ln(2)} \cdot \sigma$ to

$$\begin{aligned} \text{FWHM(IGZO)} &= 3.65\,\text{GHz} \\ \text{FWHM(APD)} &= 2.80\,\text{GHz}. \end{aligned}$$

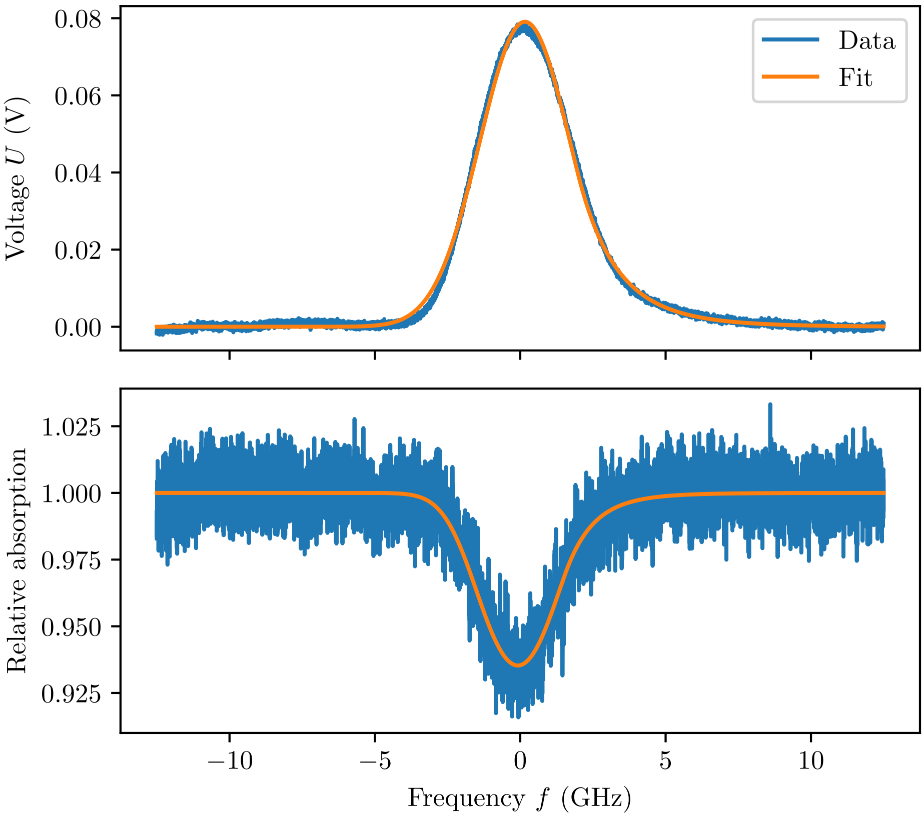

Figure 44: Fluorescence measurement with the IGZO diode (top), absorption measurement with the commercial Thorlabs APD130A2 (bottom) on a relative frequency axis. The fit functions are according to 5.6 and 5.8, where the baseline was subtracted at the measurement and fit. The parameters for this measurement were $P = 170\,\mu\text{W}$, $p = 0.1\,\text{mbar}$, $U_\text{D} = 2\,\text{V}$ and a tuning range of the 904 nm laser of 10 GHz at a duration of 1000 s.

The values for the FWHM are in line with the theoretically expected value for the Doppler broadening, although this is somewhat higher than expected for the IGZO sensor. With the APD it is even slightly lower, but as can be seen in Figure 44, the signal is somewhat noisy and therefore inaccuracies in the fit could arise. To compare the FWHM and the amplitudes of the Gaussian function, measurements were made as a function of pressure and laser power.

Figure 45 shows the fit parameters obtained for the measurement as a function of pressure. The increase in the amplitude of the IGZO diode (a) and the relative absorption (b) of the APD can be reasonably explained by the fact that, due to the increased pressure, more NO molecules are available for excitation and re-emission of light. In the range of $0 - 1.5\,\text{mbar}$, the gas does not yet appear to be optically dense, so that the relative absorption would saturate. The FWHMs for the APD in (d) vary between $2.8 - 3\,\text{GHz}$, only for small pressures they are significantly smaller at 2.6 GHz. However, this is due to the measurement signal and the resulting fit, since this is very noisy at such small pressures. In contrast, the increase in the

IGZO diode in (b) cannot be explained by the broadening mechanisms. Pressure broadening is out of question, as has already been shown above. One explanation lies in the slow fall time of the sensor and the resulting broadening of the signal. The increase is probably due to the fact that over the measurement time in the IGZO more and more long-lived states such as oxygen vacancies and peroxides are generated, which then broaden the signal even more due to the worsened fall time.

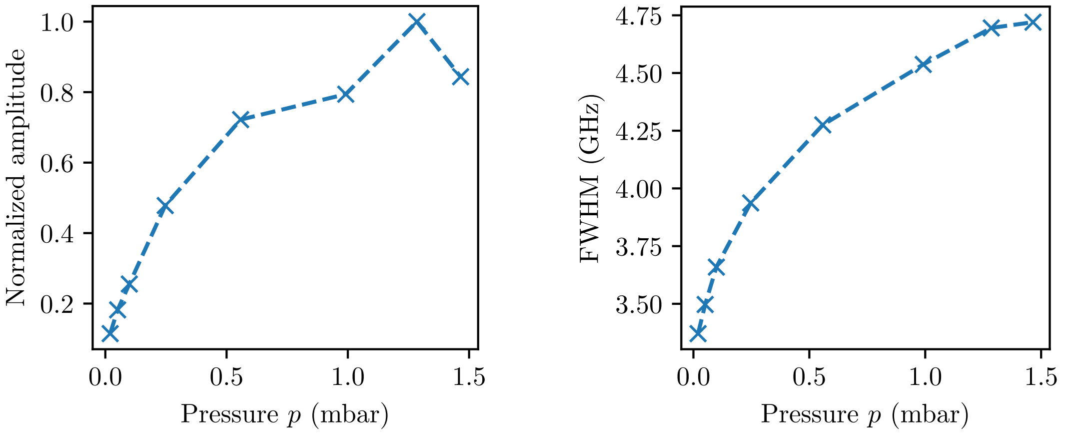

(a) IGZO sensor (b) IGZO sensor

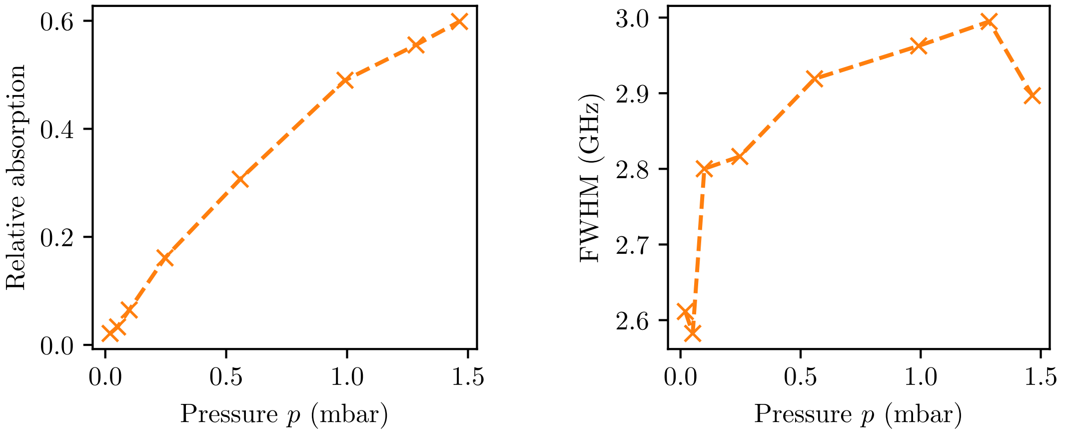

(c) APD (d) APD

Figure 45: Fit parameters for the amplitude and the FWHM of the Gaussian functions according to equation 5.6 for the IGZO sensor and equation 5.8 for the APD as a function of pressure at a wavelength of 226 nm at a laser power of 170 μW.

Figure 46 shows the parameters obtained for the measurements as a function of laser power. Both the amplitude at the IGZO diode in (a) and the relative absoprtion in (c) increase with laser power. This value should remain constant. In the case of the IGZO diode, this can again be explained by the long-lived states, which maintain an increased photocurrent over time. The small fluctuations in the photodiode are more likely due to fluctuations in laser power or pressure, since as shown the power broadening is much too small. The FWHM of the APD (d) is relatively stable around 2.8 GHz except for an outlier at high power. The FWHM of the IGZO diode in (b) rises again, which is due to the same argument by the long-lived conditions by oxygen vacancies and peroxide formation.

Overall, however, it can be said that the IGZO sensors can reliably detect fluorescence light, even if the widths can only provide an indication rather than an exact value.

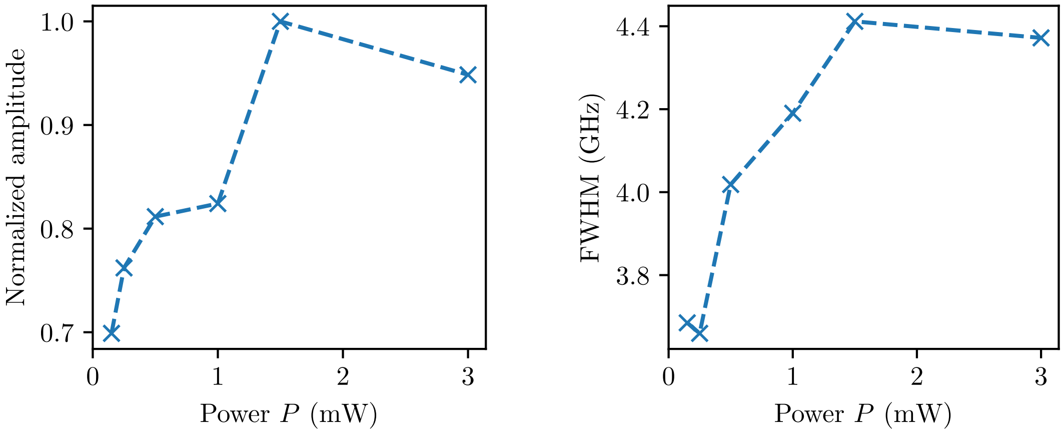

(a) IGZO sensor

(b) IGZO sensor

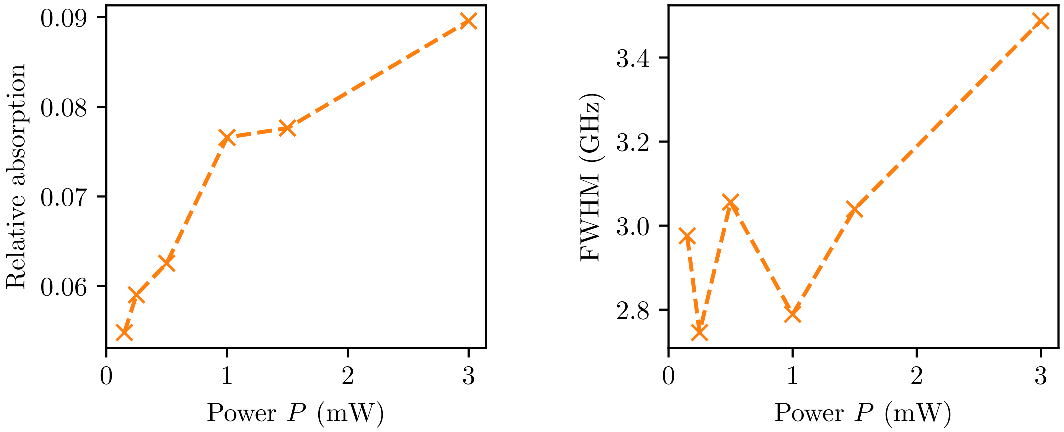

(c) APD

(d) APD

Figure 46: Fit parameters for the amplitude and the FWHM of the Gaussian functions according to equation 5.6 for the IGZO sensor and equation 5.8 for the APD as a function of laser power at a wavelength of 226 nm at a pressure of 0.1 mbar.

As a final measurement with a single sensor, the 226 nm UV light was passed through a $\lambda/2$ waveplate. This allows the polarization of the light to be changed. The aim of this measurement is to show that the direction of the NO dipole radiation can be adjusted by changing the polarization. When a dipole is excited with the laser, it emits light perpendicular to the direction of excitation. Since the sensor is on a specific side of the cell (in this case on the bottom side), if linearly polarized light is assumed, a rotation of 45° of the waveplate from the maximum of the signal should result in a value of zero, since all emitted light from the NO would have to travel perpendicular to the sensor area. For a $\lambda/2$ plate, the following applies to the E-field vector when assuming a plane wave in z direction [45]

$$\boldsymbol{E}(z,t) = E_0 \cdot \begin{pmatrix} \cos\phi \\ -\sin\phi \end{pmatrix} \cdot e^{i(\omega t - kz)} \tag{5.9}$$

with ϕ the angle of the waveplate which referring to the rotated polarization angle $\varphi = 2\phi$.

As a first measurement, an additional polarizing beamsplitter cube was placed after the cell and before the APD. This measurement should serve as a comparison to the measurement of the sensor. The beamsplitter cube only allows p-polarized light to pass through in the beam direction, and s-polarized light at 90° to it. If the $\lambda/2$ plate is now rotated, only certain portions of linear polarized light should pass through the beamcube as a result of the rotation. Figure 47 above shows such a measurement. The waveplate is automatically rotated by a stepper motor. The measurement shows the measurement signal of the APD for a complete rotation of the waveplate. The sinusoidal waveform, which reaches a minimum at each 45° rotation, can be seen very clearly. Therefore a fit function of the following form is assumed

$$f(x) = a \cdot \sin(\omega x - \varphi) + c \tag{5.10}$$

where a is the amplitude of the sinusoidal wave, ω the angular velocity, φ the phase offset and c some general offset. The fit results (shown in orange color in the plot) in an angular velocity of $\omega = 0.0691/°$, which translates to a period of $T = 2\pi/\omega = 90.9°$. This confirms that the $\lambda/2$ waveplate meets the assumptions exactly. The fact that the signal does not drop to 0 probably has to do with the laser light not being fully linear polarized and imperfections in the beam cube and waveplate.

Now the measurement was repeated with the sensor. Due to offsets and fluctuations of the sensor, the baseline as well as the amplitude of the sinusoidal curve was fitted with a third order polynomial for a better fit. Figure 47 (b) shows the measurement after subtracted baseline and fit. The signal is very noisy, but nevertheless it was possible to obtain a fit which gives an angular velocity of $\omega = 0.0681/°$, and thus a period of 92.25°. This result is also very close to the expected value and confirms the dipole theory. The reason for such a weak signal is probably that the laser light does not only consist of linearly polarized light as shown in the measurement before and therefore also radiation components can contribute not only perpendicularly to the irradiation. In addition, it is possible that previously emitted dipole radiation can be reabsorbed by other NO molecules and thus also be emitted again in an undesired direction.

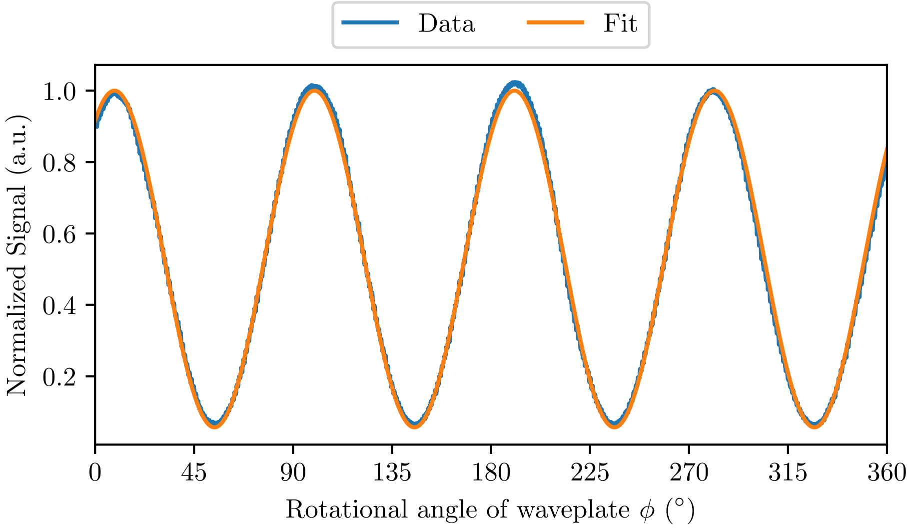

(a) Measurement signal of the APD as a function of the angle of the waveplate. In addition, a polarizing beamcube is placed in front of the APD.

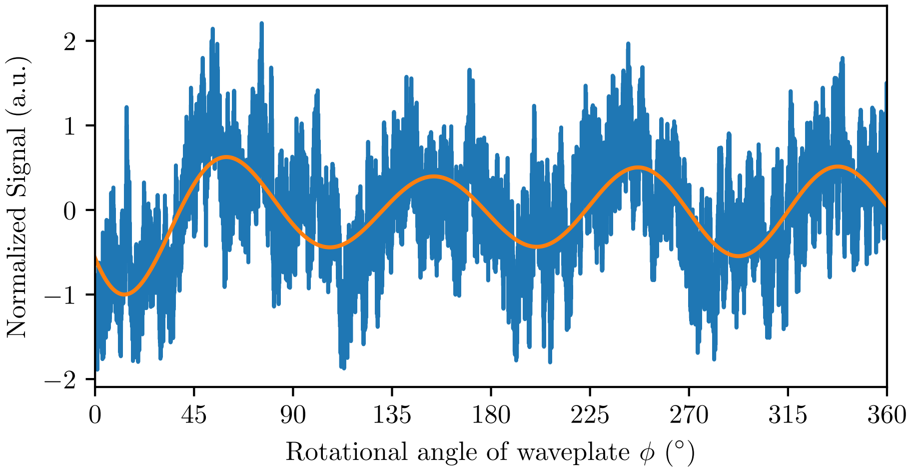

(b) Measurement signal of the IGZO sensor as a function of the angle of the waveplate. The baseline is subtracted from fit and measurement signal.

Figure 47: Measurements of the signal strength of the APD and the IGZO sensor when rotated on an $\lambda/2$ waveplate. The waveplate was automatically rotated 360° by a stepper motor. The measurement was performed in the 226 nm laser experiment.

5.4 Spatial measurement

As a final measurement, the array of sensors was tested. The aim was to perform spatially resolved measurements. For this purpose, not only a single sensor was read out, but all 64 sensors were controlled via the Arduino. Due to the poor fall time, the readout delay between the measurement of a pixel must be selected in such a way that there is no or at least as little influence as possible. The delay per pixel was 50 milliseconds during the measurements. This means that all pixels are updated every 3.2 seconds.
A measurement with an glas substrate outside the cell was first performed. It was positioned directly behind the glas cell so the laser beam reached the substrate perpendicular. Figure 48 shows the measurement. It can be clearly seen that the laser beam impinges approximately on the center of the array. The Gaussian profile of the beam is also indicated, as the beam intensity drops rapidly towards the edge. The beam profile measured with a commercial photodiode has a beam radius of about 0.9 mm, which could also be shown in this measurement when the pixels to the right and left of the center (red C) are taken. The peak two pixels above is due to the fact that the sensor is not calibrated and therefore the individual sensors respond differently. Since the resolution is limited to 8x8 pixels, the statement is rather quantitative. Nevertheless, this shows that even a realization with low resolution can already provide a good estimate of the beam profile.

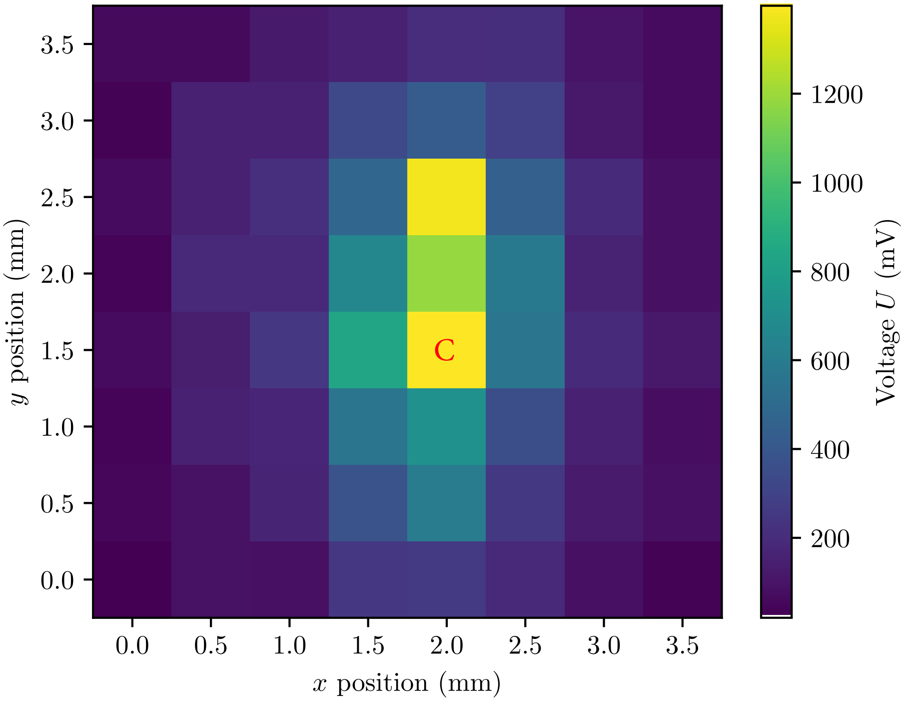

Figure 48: Measurement of the sensor array outside positioned directly behind the cell with the 226 nm laser, displayed as PixelGrid. The laser beam reaches the glas substrate perpendicular.

The first measurement inside the cell should show that the array responds to the position of the laser beam in parallel. At a power of 1.3 mW and a pressure of about 0.1 mbar all pixels were read out at four different laser positions. The laser beam was shifted slightly by adjusting a mirror. Figure 49 shows the array displayed as individual pixels under four different positions. It can be clearly seen that the sensors respond the most at position 3. It can therefore be assumed that the laser beam is closest to the sensor array here. At position 1, the laser beam seems to be farthest away, so that almost no photocurrent is generated. Position 2 lies between 1 and 3 and thus has a deflection that lies in between. Position 4 moves away from the array again, which is also visible in the measurement data. The difference of the individual pixels is related to the fact that the sensor could not be calibrated. For this, the complete sensor would have to be illuminated in the same way, which was not possible due to the small beam size of 0.9 mm. Since the individual pixels are also only about 0.5 mm apart, it should be possible to see the beam even in the PixelGrid. However, this could not be shown yet. The reason for this is probably scattering of the light by multiple absorption and emission, as well as distortions due to the slow fall time. Nevertheless, it could be shown that almost all sensors react to the light and a readout is feasible.

A second measurement will show the behavior of the sensor response at different pressures. Figure 50 shows the measurement results of the PixelGrid for a wide pressure range from 0.06 mbar to 16.55 mbar with a laserpower of 0.5 mW. There it can be seen that for an increasing pressure up to about 0.6 mbar only the photocurrent increases. This agrees with the measurements in Figure 45. Due to the increased number of NO molecules, there is more absorption and thus also more fluorescent light. However, if the pressure continues to increase, the signal drops rapidly again. This is due to the fact that for high pressures the number of molecules becomes so large that the fluorescent light does not reach the sensors at all, but is re-absorbed and emitted all the time beforehand. This makes the gas in the cell optically dense for measurements at the sensor. For very high pressures above 3 mbar, it is very clearly visible that the measured voltage is only in the range of the dark current. Therefore, a measurement only makes sense if the medium is not optically dense. In this range, it should then only be possible to perform truly spatially resolved measurements. In order to improve the spatial resolution, for example, an attempt can be made to reduce the scattered light by installing a sort of “channel” for the individual sensors so that only light can reach and be detected in parallel.

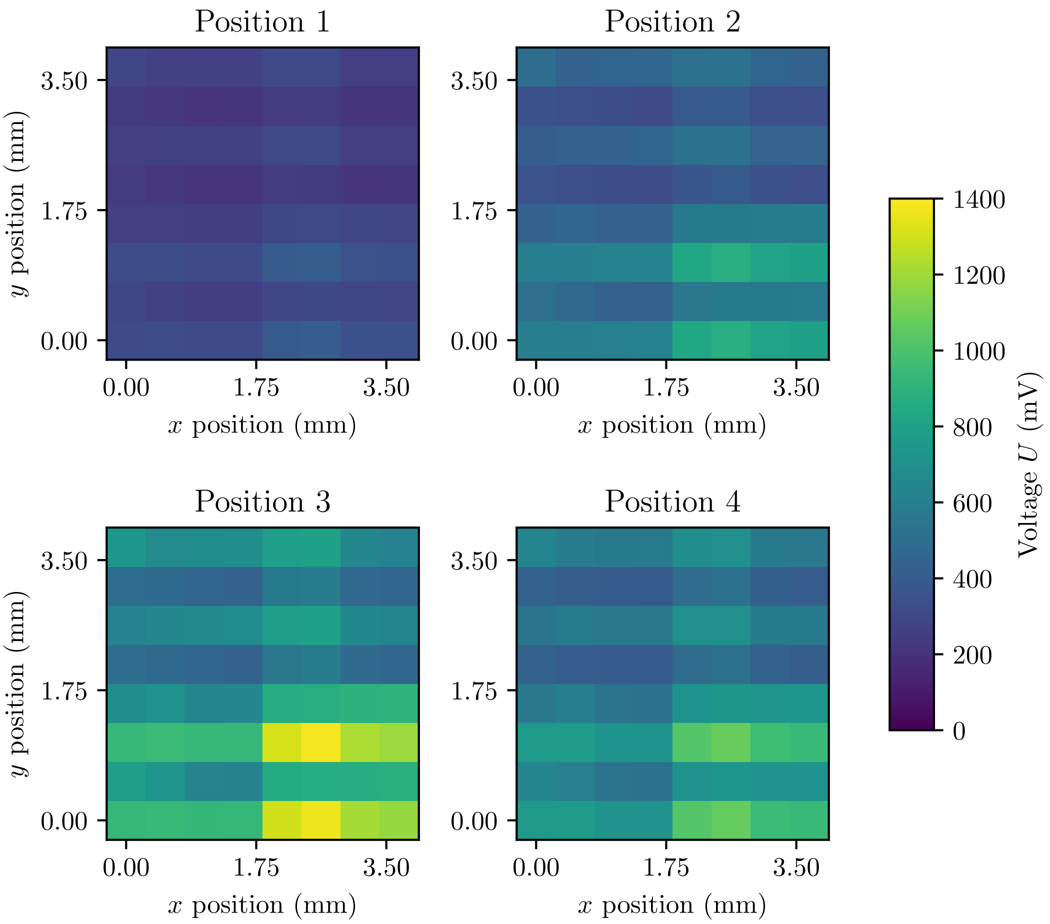

Figure 49: Measurement of the sensor array for different positions of the 226 nm laser displayed as PixelGrid. The measurement was performed at a power of $P = 1.3\,\text{mW}$, a pressure of $p = 0.1\,\text{mbar}$ and a readout delay of the individual sensors of 50 ms.

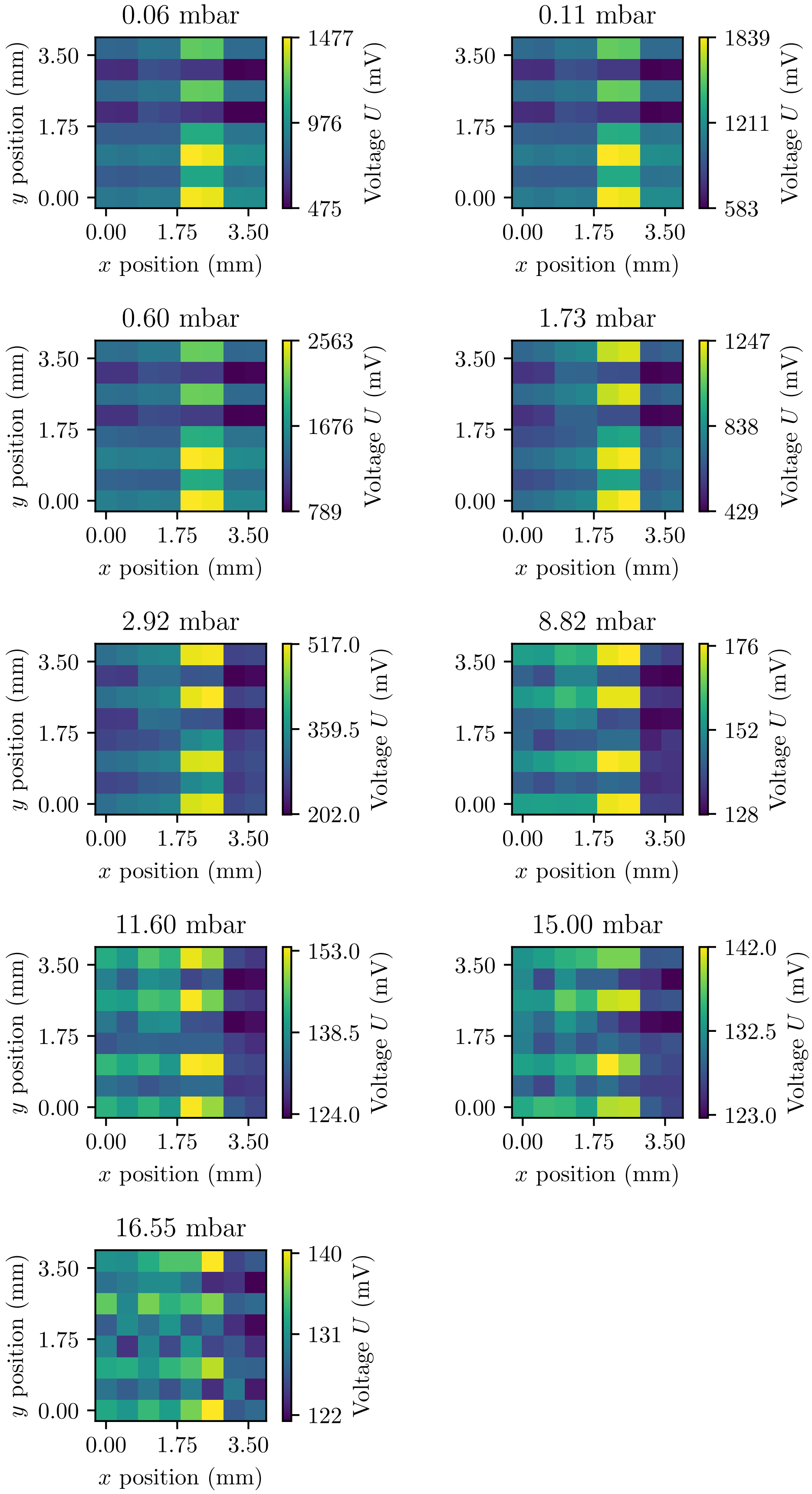

Figure 50: Measurement of the sensor array for different pressures with the 226 nm laser, displayed as PixelGrid. The measurement was performed at a power of $P = 0.5\,\mathrm{mW}$ and a readout delay of the individual sensors of 50 ms.

6 Conclusion

6.1 Summary

In this work, photosensors were fabricated and characterized using indium gallium zinc oxide (IGZO) thin film technology. Since IGZO has a large band gap of over 3 eV, it is suitable as a semiconductor material for photosensors in the UV range.
First, different sensor designs were fabricated and tested. It was found that the generated photocurrent depends on the active area of the sensor as well as the geometry. As a result, with gold electrodes, smaller dimensions of $10 - 100\,\mu$m width provided almost the same results as larger ones. The decisive value for making this conclusion was the ratio of the current with irradiation and the dark current, which was above 10. The obtained U/I curve showed Ohmic behavior for the most part, although a Schottky contact was predicted by the metal-semiconductor contact. In addition, it was found that the response time depends on the thickness of the IGZO layer. The best values, which ranged in the millisecond regime for rise and fall time, were achieved by 120 nm film thickness.
It was also tested whether the variation of the active layer has an influence on the characteristics. For this purpose, one side of the gold electrode was replaced by indium tin oxide (ITO) or aluminum. However, this did not lead to any response time improvements.
A vertical diode design was also tested, which used two gold electrodes or a variation with ITO in the production process. Here, the response times were significantly worse, so that this attempt also led to no improvement. Nevertheless, this type of sensor can be used in other applications as a load source for currents, since it shows a constant plateau of the photocurrent in the U/I characteristic.
From these findings, it was concluded that a photodiode with two gold electrodes and an active sensor area dimension of $10\,\mu$m x $100\,\mu$m was the best result. The best values for the photocurrent ratio were 2134 and response times in the low millisecond range, both for UV light at 385 nm and at 226 nm. Responsivities of up to 2000 A/W at 226 nm light were achieved, which is several times better than in other studies [25, 28, 24, 1, 28]. The responsivity depends on the applied diode voltage, the power of the UV light and the temperature. High diode voltages of 20 V, lower light powers of a few microwatts and room temperature achieved the best values. The noise equivalent power (NEP) is significantly better than conventional silicon based avalanche photodiodes [3] with a value of up to $0.26\,\mathrm{nW}/\sqrt{\mathrm{Hz}}$ for 385 nm light.
The diodes were then also tested in a real experiment in which nitric oxide flows through a glas cell and is excited by lasers. The fluorescence light could be detected with the help of these sensors, with the determined widths roughly corresponding to the theoretical Doppler broadening. In addition, it was possible to show how the radiation properties of a dipole change with a change in polarization. As a last step in this work, the sensors were produced in an 8x8 sensor array, with which it was possible to read out all sensors spatially and even get comparable results to an commercial photodiode in terms of beam profile characteristics.

6.2 Outlook

The results shown here provide a good basis for further research in the field of IGZO photosensors.
It is possible that other design approaches such as different electrode materials, or the arrangement of these, may lead to improvements. The most important point is probably the improvement of the response time. The thickness of the IGZO layer can be increased and further improvements in the response time can be expected. Mixtures of IGZO layers with other materials, as described in [25], are also approaches that can be pursued. Degradation of the exposed IGZO layer can be achieved by a passivation layer, which increases durability.
Perhaps the second important point is the improvement of the sensor array. In this work, first spatial measurements could be performed, but for more accurate results, the design of the array has to be adapted. Channels that allow light to pass only parallel to them prevent scattered light and improve accuracy. The readout circuit can be further optimized to improve noise and speed. Currently, the array is limited to 8x8 passive matrix sensors, so the circuit would have to be changed for larger designs and an active matrix approach could reduce cross talk between individual sensors. The scalability does not depend on the array itself, but on the readout electronics and the response of the photosensors. Since other components such as operational amplifiers, resistors, capacitors and much more can also be manufactured in thin-film technology, manufacturing process steps can be combined in order to realize as much electronic components as possible on glas substrates.
In summary, further research on IGZO sensors is of present relevance and offers promising results.

7 Literature

References

[1] H. T. Zhou, L. Li, H. Y. Chen, Z. Guo, S. J. Jiao, and W. J. Sun. Realization of a fast-response flexible ultraviolet photodetector employing a metal–semiconductor–metal structure InGaZnO photodiode. *RSC Advances*, 5(107):87993–87997, 2015.

[2] Ying Zhu, Yongli He, Shanshan Jiang, Li Zhu, Chunsheng Chen, and Qing Wan. Indium gallium zinc oxide thin-film transistors: Materials, devices, and applications. *Journal of Semiconductors*, 42(3):031101, March 2021.

[3] Si Avalanche Photodetectors Thorlabs. `https://www.thorlabs.com/newgrouppage9.cfm?objectgroup_id=6686`. Accessed 22.05.23.

[4] Yannick Schellander, Marius Winter, Maurice Schamber, Fabian Munkes, Patrick Schalberger, Harald Kuebler, Tilman Pfau, and Norbert Fruehauf. Ultraviolet photodetectors and readout based on a-IGZO semiconductor technology. *Journal of the Society for Information Display*, 31(5):363–372, May 2023.

[5] C.J. Foot. *Atomic Physics -*. OUP Oxford, New York, London, 2005.

[6] Rubidium 85 D Line Data - Daniel Adam Steck Oregon Center for Optics and Department of Physics, University of Oregon. `https://steck.us/alkalidata/rubidium85numbers.pdf`, 2021. Accessed 11.04.23.

[7] Wolfgang Demtroeder. *Experimentalphysik 1 - Mechanik und Wärme*. Springer-Verlag, Berlin Heidelberg New York, 2015.

[8] Hermann Haken and Hans C. Wolf. *Molekülphysik und Quantenchemie - Einführung in die experimentellen und theoretischen Grundlagen*. Springer-Verlag, Berlin Heidelberg New York, 2013.

[9] Gerhard Herzberg. *Spectra of Diatomic Molecules -*. Van Nostrand, Princeton, New Jersey, 1950.

[10] PubChem. Nitric Oxide. `https://pubchem.ncbi.nlm.nih.gov/compound/145068`. Accessed 04.04.23.

[11] Nitric oxide | Uses, Facts, & Definition | Britannica. `https://www.britannica.com/science/nitric-oxide`, March 2023. Accessed 04.04.23.

[12] Fabian Munkes. *Continuous-wave absorption spectroscopy on the* $X^2\Pi_{1/2}$ *to* $A^2\Sigma^+$. Master's thesis, 5th Institute of Physics, University of Stuttgart, 2019.

[13] Yannick Schellander. *Ionization current measurements of Rydberg states in nitric oxide created by continuous-wave three-photon excitation.* Master's thesis, 5th Institute of Physics, University of Stuttgart, 2020.

[14] Spontaneous and stimulated emission - FiberLabs Inc. `https://www.fiberlabs.com/glossary/spontaneous-and-stimulated-emission/`, May 2021. Accessed 06.04.23.

[15] George Louis Zarur and Ying-Nan Chiu. Cooperative optical phenomena. ii. spin-forbidden lifetime of the $a^4\Pi$ state of nitric oxide. *The Journal of Chemical Physics*, 59(1):82–88, 1973.

[16] H. Lefebvre-Brion and F. Guerin. Calculation of the radiative lifetime of the $a^4\Pi$ state of no. *The Journal of Chemical Physics*, 49(3):1446–1447, 1968.

[17] Colin M. Western. PGOPHER: A program for simulating rotational, vibrational and electronic spectra. *Journal of Quantitative Spectroscopy and Radiative Transfer*, 186:221–242, January 2017.

[18] Prof. Dr.-Ing. Norbert Fruehauf. *Lecture Thin Film Technology.* Vorlesungsskript, Institut für Großflächige Mikroelektronik, Universität Stuttgart, 2020/2021.

[19] Marius Winter. *Entwicklung von Operationsverstärkern mit Indium-Gallium-Zink-Oxid Dünnschichttransistoren.* Master's thesis, Institut für Großflächige Mikroelektronik, University of Stuttgart, 2022.

[20] Marco Dettling. *Development, Characterization and Readout of Large-Area Photosensor Arrays.* Master's thesis, Institut für Großflächige Mikroelektronik, University of Stuttgart, 2022.

[21] Rudolf Gross and Achim Marx. *Festkörperphysik* -. De Gruyter, Berlin, 2018.

[22] Henri Menke. *Fortgeschrittene Molekül- und Festkörperphysik.* Vorlesungsskript, Universität Stuttgart, 2014/2015.

[23] Kin-Tak Lam, Sheng-Joue Young, Yen-Lin Chu, Chi-Nan Tsai, Tung-Te Chu, Ting-Sung Lu, and Liang-Wen Ji. Characteristics of Metal Semiconductor Metal Ultraviolet Photodetectors Based on Pure ZnO/Amorphous IGZO Thin-Film Structures. *Journal of Nanomaterials*, 2021:1–6, April 2021.

[24] Jingjing Yu, Kashif Javaid, Lingyan Liang, Weihua Wu, Yu Liang, Anran Song, Hongliang Zhang, Wen Shi, Ting-Chang Chang, and Hongtao Cao. High-Performance Visible-Blind Ultraviolet Photodetector Based on IGZO TFT Coupled with p–n Heterojunction. *ACS Applied Materials & Interfaces*, 10(9):8102–8109, March 2018.

[25] Ying-Tsung Li, Chang-Fu Han, and Jen-Fin Lin. Characterization of the electrical and optical properties for a-IGZO/Ag/a-IGZO triple-layer thin films with different thickness depositions on a curved glass substrate. *Optical Materials Express*, 9(8):3414, August 2019.

[26] Toshio Kamiya, Kenji Nomura, and Hideo Hosono. Origins of High Mobility and Low Operation Voltage of Amorphous Oxide TFTs: Electronic Structure, Electron Transport, Defects and Doping*. *Journal of Display Technology*, 5(12):468–483, December 2009.

[27] Stefan Knobelspies, Benedikt Bierer, Alwin Daus, Alain Takabayashi, Giovanni Salvatore, Giuseppe Cantarella, Alvaro Ortiz Perez, Jürgen Wöllenstein, Stefan Palzer, and Gerhard Tröster. Photo-Induced Room-Temperature Gas Sensing with a-IGZO Based Thin-Film Transistors Fabricated on Flexible Plastic Foil. *Sensors*, 18(2):358, January 2018.

[28] Chun-Ying Huang, Tzu-Yu Peng, and Wan-Ting Hsieh. Realization of a Self-Powered InGaZnO MSM UV Photodetector Using Localized Surface Fluorine Plasma Treatment. *ACS Applied Electronic Materials*, 2(9):2976–2983, September 2020.

[29] Xinge Yu, Tobin J. Marks, and Antonio Facchetti. Metal oxides for optoelectronic applications. *Nature Materials*, 15(4):383–396, April 2016.

[30] David C. Hays, B. P. Gila, S. J. Pearton, and F. Ren. Energy band offsets of dielectrics on InGaZnO $_4$. *Applied Physics Reviews*, 4(2):021301, June 2017.

[31] Hyukjoon Yoo, I. Sak Lee, Sujin Jung, Sung Min Rho, Byung Ha Kang, and Hyun Jae Kim. A Review of Phototransistors Using Metal Oxide Semiconductors: Research Progress and Future Directions. *Advanced Materials*, 33(47):2006091, November 2021.

[32] Invertierender Verstärker (Operationsverstärker). `https://www.elektronik-kompendium.de/sites/slt/0210141.htm`. Accessed 02.05.23.

[33] Spannungsteiler. `https://www.biancahoegel.de/technik/schaltung/spannungsteiler.html`. Accessed 02.05.23.

[34] Passiven Tiefpass 1. und 2. Ordnung berechnen </br>Funktionsweise, Formel, Tiefpass Rechner. `https://electronicbase.net/de/tiefpass-berechnen/`. Accessed 02.05.23.

[35] Arduino Uno (R3). `https://www.kriwanek.de/index.php/de/arduino/boards/403-arduino-uno-r3`. Accessed 25.05.23.

[36] Joon Seok Park Hyun Jae Kim. *Oxide TFTs for Displays and Beyond.* Display Week, Los Angeles, 2023.

[37] Austrittsarbeit, FH Uni Münster. `https://www.fh-muenster.de/ciw/downloads/personal/juestel/juestel/chemie/Austrittsarbeit.pdf`. Accessed 17.05.23.

[38] Shraddha D. Nehate, Adithya Prakash, Prabhu Doss Mani, and Kalpathy B. Sundaram. Work Function Extraction of Indium Tin Oxide Films from MOSFET Devices. *ECS Journal of Solid State Science and Technology*, 7(3):P87, February 2018.

[39] Spezifischer Widerstand. `https://www.chemie.de/lexikon/Spezifischer_Widerstand.html`. Accessed 17.05.23.

[40] Indium tin oxide. `https://en.wikipedia.org/w/index.php?title=Indium_tin_oxide&oldid=1140111569`, February 2023. Accessed 17.05.23.

[41] H. K. Li, T. P. Chen, S. G. Hu, X. D. Li, Y. Liu, P. S. Lee, X. P. Wang, H. Y. Li, and G. Q. Lo. Highly spectrum-selective ultraviolet photodetector based on p-NiO/n-IGZO thin film heterojunction structure. *Optics Express*, 23(21):27683, October 2015.

[42] Phillip Neufeld. *Collisional ionization of Rydberg states in nitric oxide.* Master's thesis, 5th Institute of Physics, University of Stuttgart, 2022.

[43] Patrick Kaspar, Fabian Munkes, Philipp Neufeld, Lea Ebel, Yannick Schellander, Robert Löw, Tilman Pfau, and Harald Kübler. Doppler-free high-resolution continuous-wave optical UV spectroscopy on the A $^2\Sigma^+ \leftarrow$ X $^2\Pi_{3/2}$ transition in nitric oxide. *Physical Review A*, 106(6):062816, December 2022.

[44] Crystal Ball Function. Wikipedia. `https://en.wikipedia.org/wiki/Crystal_Ball_function`. Accessed 23.05.23.

[45] Wolfgang Demtroeder. *Elektrizität und Optik* -. Springer, Berlin, Heidelberg, 2006.